

December 1992

1N-71
135310
P-77

Unsteady Pressure Loads in a Generic High-Speed Engine Model

Tony L. Parrott,
Michael G. Jones,
and Ernie M. Thurlow

(NASA-TP-3189) UNSTEADY PRESSURE
LOADS IN A GENERIC HIGH SPEED
ENGINE MODEL (NASA) 77 p

N93-15391

Unclas

H1/71 0135310

[The page contains extremely faint and illegible text, likely a scan of a document with very low contrast or significant noise. No specific words or structures are discernible.]

**NASA
Technical
Paper
3189**

1992

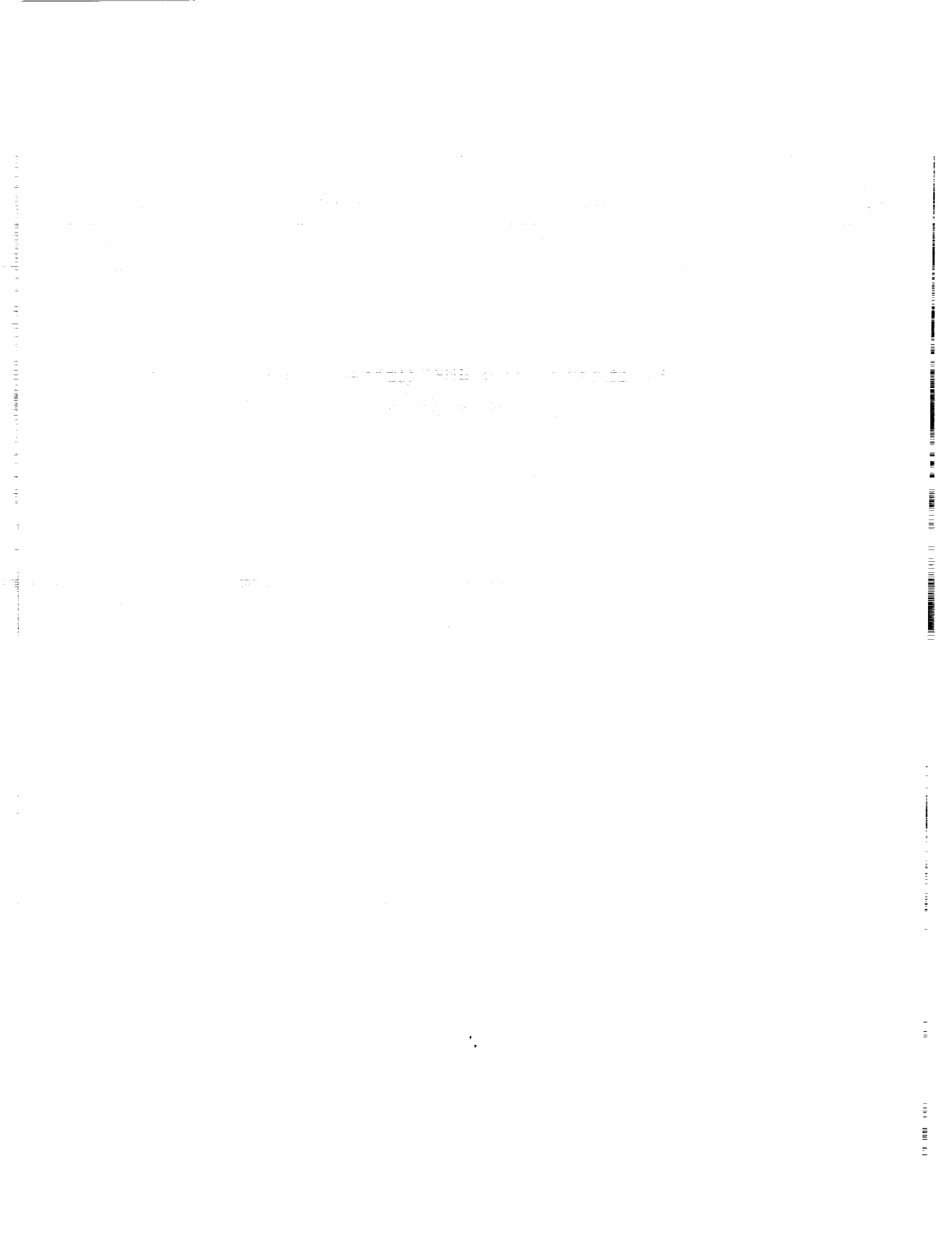
Unsteady Pressure Loads in a Generic High-Speed Engine Model

Tony L. Parrott
*Langley Research Center
Hampton, Virginia*

Michael G. Jones
and Ernie M. Thurlow
*Lockheed Engineering & Sciences Company
Hampton, Virginia*



National Aeronautics and
Space Administration
Office of Management
Scientific and Technical
Information Program



Summary

Fluctuating pressure loads were measured along the top interior wall of a generic scramjet engine model during a series of performance tests conducted in the Combustion-Heated Scramjet Test Facility at the Langley Research Center (formerly the Langley Mach 4 Scramjet Test Facility). This facility can simulate Mach number 4 flight conditions at dynamic pressures that correspond to altitudes from 57 000 to 86 000 ft. The 75-in-long model was installed in the test cabin of the facility with the inlet positioned at the tunnel nozzle exit plane. The nominal inlet Mach number was 3.5 at a total temperature and pressure of 1640°R and 92 psia, respectively.

To minimize gage exposure to damaging heat flux from the high-enthalpy flow, 0.159-in-diameter piezoresistive strain gages were recess mounted in existing calorimeter ports at nine locations along the interior of the model's top upper wall. Recess distance ranged from 4 to 12 gage diameters. This technique provided a means to obtain meaningful data in the hostile flow environment.

Fluctuating wall pressures were successfully measured to 5 kHz at five locations upstream of the combustor region and at one location in the combustor section. However, not all gages were used for every run. The root mean square (rms) pressures ranged from 0.06 to 7.8 percent of the local dynamic pressure q_e at the boundary layer edge. The rms pressures, mainly in the isolator section, greatly exceeded those reported in the literature for attached, turbulent boundary layers on flat plates, which generally tend to a limit of 1 percent q_e .

The overall fluctuating pressure levels in decibels (re 20 μ Pa), over a frequency range 0 to 5 kHz, varied from 131 dB in the inlet region to 180 dB in the isolator-combustor region. These generally high levels were measured both before and after an inlet unstart. The main effect of the unstart was to extend the high-pressure levels further upstream from the combustor into the isolator section.

A key finding was that combustion noise propagates upstream into the isolator section through the subsonic portion of the boundary layer. Combustion noise contributes to the total noise measured in the isolator section upstream of the combustor, where noise levels increased by 15 dB when the equivalence ratio (fuel-air ratio normalized by the stoichiometric ratio) was increased from 0.37 to 0.57.

Transient pressure disturbances associated with thermally induced inlet unstarts were also measured. The unstart shock was found to propagate upstream

at approximately 7 ft/sec, which suggests that transient loading effects on the engine structure have little effect on structural damage compared with boundary layer combustion noise.

Symbols

A, B	temperature-dependent parameters in gage transfer function, also empirical constants describing functional dependence of Strouhal number
A_T, B_T	derivatives of A and B with respect to temperature
C	empirical constant related to effective port area, 0.9
c	sound speed
c_e	sound speed at boundary layer edge
d	cylindrical recess diameter
E	gage output voltage, instantaneous value
E_m	mean value of gage output voltage
f	frequency
G	power spectral density
K_v	empirical constant (0.57) used in appendix C
k	polytropic constant, also statistical degrees of freedom
l	cylindrical recess length from port to gage diaphragm
$l_{i,i+1}$	length of element ($i, i + 1$)
M	local Mach number
M_e	local Mach number at boundary layer edge
N	number of sample points used in PSD analysis
N_B	number of data analysis blocks
N_{Re}	unit Reynolds number at boundary layer edge
n	cavity cross mode number, also n th sampling point
p	pressure
\bar{p}, \bar{p}_m	mean value of fluctuating pressure, also labelled μ_1
\tilde{p}	fluctuating pressure

$p(n)$	pressure at n th sampling point	Z_c	tube characteristic impedance
$p(t)$	pressure time history	α	empirical constant used in appendix C, 0.24
p_e	mean static pressure at boundary layer edge	α_3	skewness
\tilde{p}_g	fluctuating pressure at gage face	α_4	kurtosis
\tilde{p}_i	fluctuating pressure at station i of transmission line	γ	specific heat ratio
p_{rms}	rms pressure	δ^*	boundary layer displacement thickness
p_s	mean static pressure at port entrance	Δ	increment
\tilde{p}_s	fluctuating static pressure at port entrance	μ_1	mean value
p_t	mean total pressure	μ_3	third moment of pressure probability density about the mean
q_e	dynamic pressure at boundary layer edge	μ_4	fourth moment of pressure probability density about the mean
R	gas constant, 1716 ft ² /sec ² -°R	ρ_{cav}	gas density in recess cavity
R_f	recovery factor	ρ_e	gas density at boundary layer edge
$\bar{S}_p(\omega)$	averaged power spectral estimates	ρ_s	gas density at wall
$\hat{S}_p(\omega)$	power spectral estimate of $S_p(\omega)$	σ	standard deviation, also gage diaphragm deflection factor
$\hat{S}_p^j(\omega)$	power spectral estimate for j th data block	σ^2	variance
s	cross-sectional area of port	ϕ	equivalence ratio, also propagation constant
\tilde{T}	fluctuating temperature	ω	angular frequency
T_{aw}	adiabatic wall temperature	∞	free stream
T_e	static temperature at boundary layer edge	Abbreviations:	
T_t	total temperature of gas	ESP	electronic scanning pressure system
T_w	wall temperature	GHSE	generic high-speed engine
t	time	OASPL	overall sound pressure level computed from variance
t_B	time length of data block	(OASPL) _{PSD}	overall sound pressure level computed from PSD
t_{total}	time length of N_B contiguous data blocks	PD	probability density
U_e	gas velocity at boundary layer edge	PDF	probability density function
\tilde{U}_g	fluctuating volume velocity at gage face	PSD	power spectral density
\tilde{U}_i	fluctuating volume velocity at station i of transmission line	PSIA	absolute pressure in pounds per square inch
V	cavity volume over gage diaphragm	rms	root mean square
W_s	combined data window correction and calibration constant	R6B7	run 6, batch 7
		R15B6	run 15, batch 6
		R50B10	run 50, batch 10

TDR	transient data recorder
TN	tunnel nozzle

Introduction

The use of air-breathing propulsion systems for aerospace-plane vehicles requires a flight path optimized for maximum tolerable dynamic pressure to achieve high propulsive efficiency. Unfortunately, high dynamic pressures imply severe unsteady pressure loads on surface areas exposed to turbulent boundary layers. In localized areas of shock impingement or flow separation associated with high surface curvature, unsteady pressure loads may be exacerbated such that overall levels may reach at least 170 dB (re 20 μ Pa), a level that may severely damage structures. As yet, no analytical models provide the structural design engineer with needed predictive accuracies for these unsteady loads. In particular, how are the characteristics of unsteady boundary layer loads on the interior of scramjet engines affected by interacting shock wave and boundary layers, separated flow over surfaces of high curvature, and the combustion process?

Scramjet propulsion engineers seek to relate engine performance to unsteady loads measured at various locations on the interior walls. A particular interest is the highly undesirable phenomenon known as "engine unstart," which is preceded by a destabilization of the inlet shock system. In the unstarted state, a bow shock forms in front of the engine inlet; the resulting flow pattern allows a large amount of spillage flow around the engine, with a consequent drag increase and combustor flame out. When the engine is operating at the highest possible level of heat release rate (i.e., near thermal choke), transient pressure disturbances from the combustion unsteadiness may initiate an unstart. High engine efficiency depends, in part, on the highest possible heat release rate consistent with stable operation. Thus, it is important to quantify the unsteady loads in the engine interior before an engine unstart.

Thus, two critical problems exist for designers of supersonic combustion ramjets (scramjets): control of the engine operating transients to prevent aerodynamic instabilities from initiating an engine unstart, and design of structures to withstand intense fluctuating pressure loads generated on the engine interior by aerodynamic and combustion processes. In his review of aerothermal problems associated with hypersonic flight, Holden (ref. 1) states that even the prediction of laminar-to-turbulent transition remains an important unresolved problem in hypersonic flow. Further, the complex flow fields around interacting

shock waves and turbulent boundary layers make detailed analytical predictions of such regions almost impossible within the framework of the boundary layer equations. Therefore, an ability to predict fluctuating loads associated with these complicated flows must likely rely on a systematic measurement program to supply the necessary data base both for engine aerodynamics and component design.

This work has a twofold purpose. The primary purpose is to enhance and extend the existing technology for fluctuating loads measurements over a broad frequency range underneath the boundary layers of high-speed and high-enthalpy flows. When exposed to such flows, the piezoresistive transducer element typically used in conventional flush-mounted pressure gages sustains excessive thermal loads that cause gage sensitivity changes and even failure. Therefore, other measurement configurations must be found. Although active cooling has been a solution in some cases, this technique is too mechanically intrusive and inconvenient for most applications. This paper documents an attempt to measure unsteady loads during performance tests of a generic scramjet engine model with high-frequency pressure gages recessed into the interior wall to reduce thermal flux to the gage diaphragm. The gages were installed in existing calorimeter ports. The model was designed by the Johns Hopkins Applied Physics Laboratories and tested in the Combustion-Heated Scramjet Test Facility at the Langley Research Center.

The second purpose of the work is to present results of unsteady loads measurements in a scramjet model. These data are relevant to aerodynamic performance and structural design. The results include pressure time histories obtained during a thermally induced engine unstart, pressure spectra during steady-state operation, and the effects of increased heat release rate on fluctuating pressures in the boundary layer upstream of the combustor (isolator section).

Experiment Configuration

Test Facility

The tests were conducted in the Combustion-Heated Scramjet Test Facility at the Langley Research Center (formerly the Langley Mach 4 Scramjet Test Facility). A schematic diagram of the facility is shown in figure 1. The facility is equipped with an air ejector to enable simulation of dynamic pressures from 500 to 1900 psfa (altitude from 86 000 to 57 000 ft) at a Mach number of 4. Flight enthalpy is duplicated by the combustion of hydrogen in air

with oxygen replenishment to yield vitiated air that contains an oxygen volumetric content of 21 percent. The test gas from the burner is expanded through a converging-diverging nozzle to a Mach number of 3.5. This supersonic flow exhausts as a free jet from the 13-in. square nozzle exit into a cabin that houses the model. The gas passes through and around the model into an exhaust duct system connected to an annular air ejector that exhausts to the atmosphere. As shown in figure 1, the facility is within a cell that has an ambient air intake tower at the upstream end and an exhaust tower at the downstream end. A more complete description of this facility, along with calibration results, is given in reference 2.

Test Model

A scramjet engine model, designed by the Johns Hopkins Applied Physics Laboratories, was installed in the facility cabin. Figure 2 shows the uninstalled model. The copper heat sink model (1200 lbm) was equipped with various spill doors and boundary layer bleed plates to condition the flow and to aid inlet starting. The copper mass provided a heat sink for the intense thermal flux generated by the aerodynamic and combustion processes. In figure 3 the model is shown installed in the facility with the spill window open. The flow is from right to left. Test results relating to the performance of this model as a propulsive device are described in reference 3 and are not discussed here.

Important features of the model relevant to the present discussion are shown in the conceptual view of figure 4. The model plan view and side view (not to scale) are shown schematically in figure 5. The overall length of the model is 73.6 in. and the inlet height and width at the cowl tip are 8 and 6 in. Initial flow compression is obtained with 7° compression ramps on the top and bottom walls over the first 15.6 in. of the inlet section. This setup is followed by 3.5° sidewall compression ramps, starting 21.6 in. from the inlet mouth. The sidewall compression extends 10.8 in. to the isolator section of length, 17.2 in.

Model Configuration and Test Conditions

The facility was configured to simulate the inlet flow conditions for a hydrogen-burning scramjet behind the bow shock of a 12° half-angle conical body immersed in a Mach 4 free-stream flow. Nominal values were 1640°R for the total temperature, 92 psia for the total pressure, 11 psia for the dynamic pressure, and a Mach number of 3.5 for the gas at the model inlet.

The model was mounted such that the inside top wall surface was continuous with the inside top wall surface of the square tunnel nozzle. This approach permitted simulation of the boundary layer growth along the upper inlet wall of an integrated engine module. At the isolator entrance the flow is compressed such that the core Mach number is reduced from 3.5 at the inlet to about 1.8. The flow from the isolator section enters the combustor section where fuel struts are located at the area step. As indicated by the perspective diagram in figure 4, these struts can provide a combination of tangential and transverse injection of gaseous hydrogen; however, only transverse injection was used in this test. Also not used in this test were an internal splitter and a fuel strut upstream of the area step in the isolator section shown in figure 4. During combustion, the heated flow expands through the 10° nozzle into the exhaust duct. To measure performance, the model was equipped with 16 calorimeter ports, 204 static pressure taps, and flowmeters to measure internal flow and fuel consumption. A standard wind tunnel balance was used to measure thrust.

Pressure Gage Installation

High-frequency fluctuating pressure measurements beneath high-enthalpy boundary layer flows present a challenging problem. Commercially available high-frequency gages were employed that used piezoresistive transducing elements. The gages were temperature compensated from 80° to 450°F, with an upper temperature limit of about 600°F. To reduce sensitivity changes and probable destruction from thermal stress, it was necessary to either actively cool the gages or recess them into the wall. For mechanical convenience, recess mounting was chosen in this test, with due consideration for the possibility of spurious noise and distorted frequency response.

During a selected number of model performance tests, nine calorimeter port locations were made available for piezoresistive pressure gages distributed along the entire length of the model plus one gage in the lip of the tunnel nozzle. Six of these gage installations are shown in the distorted-scale side view of figure 6. The 0.159-in. gages were recessed from the interior wall surface by amounts varying from 0.78 to 1.97 in. to minimize damage from incident thermal flux to the diaphragms. The recess hole diameters were 0.170 in. Although gages were installed in the combustor and exhaust regions, limited gage life prevented the acquisition of meaningful data. However, the gage at location 6, in the forward region of the combustor, did survive. Gage destruction apparently was caused by hot gas spillage

flow around the outside of the model during unstarts, as opposed to excessive heat flux incident from the boundary layer. The surviving gages were located relative to the model inlet entrance at distances of -2.2, 8.5, 24.2, 35.0, 47.7, and 53.4 in. at recess depths of 0.78, 1.13, 1.97, 1.97, 1.85, and 1.75 in., respectively. All gages were designed for a pressure range of 0 to 100 psia. One other piezoresistive gage, with a range of 0 to 1000 psia, was installed downstream from a quick-acting valve in a parallel branch of the fuel supply line. This gage provided a fuel pressure time history for correlating changes in combustion noise to incremental changes in the fuel flow rate.

Additional tests were performed in a Mach 4 blowdown tunnel (cold flow) to explore sensitivity changes during thermal transients and recession effects on gage response. Thermal transient effects are addressed in appendix A. Gage recession effects on the measurement accuracy are discussed in appendix B, which also contains a correction procedure that accounts for effects of flow interaction with the open ports of the gage-cavity system. Finally, possible flow noise from the interacting boundary layer and port-cavity system (self-noise) is discussed in appendix C.

Data Acquisition, Reduction, and Analysis

An important objective of this test was to correlate transient events in the pressure time history at various gage locations with changes in the overall engine operating parameters. The use of 0- to 100-psia pressure gages allowed fluctuating pressure data, superimposed on the mean static pressure, to be acquired at each gage location. In this manner the transient events could be visually analyzed and correlated in context with the local mean static pressure at each gage location.

The data were reduced in three stages. First, time domain analysis focused on pressure transients associated with engine operation transients such as onset of fuel flow, ignition, inlet unstart, and sudden heat release. Second, pressure spectra were obtained on pressure time history segments of special interest. Third, probability density functions were calculated on these same data segments. In this section, the acquisition, reduction, and analysis procedures will be discussed.

Data Acquisition System

Figure 7 is a diagram of the instrumentation used to obtain the fluctuating pressure measurements.

Gage excitation and signal conditioning were supplied by a precision, low-noise, signal conditioning system below the tunnel test cell. The low-level signals from the pressure gages were transmitted through about 50 ft of shielded cable to the signal conditioner. Signals from the signal conditioner system were transmitted through about 75 ft of shielded cable to the digital signal acquisition system in the control room above the test cell. Fixed gains for each channel could be preset at the signal conditioner by changing the resistors in a feedback loop.

The digital data acquisition system consisted of programmable bandpass filters, transient data recorders (TDR's), and a computer system. The bandpass filter, with a roll off of 70 dB per octave, was employed as an antialiasing filter; the filter also had programmable gain that optimized the discrete signal level. The TDR's discretized the output signal levels from the filters (-10 to 10 V) into 65 536 steps. The discrete samples were then temporarily stored in 0.5-megasample/channel buffers associated with the TDR's. Depending on total gain selections, the pressure resolution ranged from 6.1×10^{-5} to 94.3×10^{-5} psia per step, for a nominal intrinsic gage sensitivity of 0.71 mV/psia. The acquisition procedure was controlled by the computer. Data sampling rate, filter cutoff frequencies, and signal amplification were inserted into the program as control parameters. A more complete description of the data acquisition system and analysis software is given in reference 4.

During a typical test run of approximately 28 sec, the pressure time history would generally include a number of transients separated by segments of statistically stationary pressure fluctuations. To capture all the data during a test run, the sampling rate was set to 15 kHz (data acquisition duration of 33 sec) and the bandpass filter was set in a low-pass mode with the cutoff frequency chosen to permit an analysis bandwidth of 5 kHz. This configuration permitted events such as inlet start, fuel ignition, and inlet unstart to be captured. After each test run, the TDR buffers were downloaded into permanent storage and a quick-look analysis of the data was performed.

System Calibration

The frequency response of the gage cavity system was expected to differ significantly from that of a flush-mounted gage. As a first step in evaluating these effects, the frequency response of the gage cavity system was measured with a small-diameter (0.2-in. by 0.4-in.) waveguide that incorporated a reference gage and a high-frequency sound source described in reference 5. This frequency response

measurement, however, did not account for flow effects. Flow effects on the recessed gage frequency response were examined analytically. This issue is addressed further in appendix B.

The pressure gages were calibrated in situ with a precision constant pressure source at various times during the tests. A two-point calibration was used that included the endpoints of the expected pressure range at a specific gage location. This direct current (dc) calibration was used to adjust the fixed gains at the signal conditioner to accommodate the expected range of pressure during a given test run. The midpoint of these pressure ranges (i.e., the mean static pressures) was estimated from expected design performance of the engine model. Consequently, there were occasional out-of-range conditions at various gage locations that could not be accommodated by the a priori chosen dynamic range. This condition generally occurred more frequently for gages farther from the inlet, particularly in the combustor region.

Data Reduction

Of the 64 test runs during which fluctuating pressure data were acquired, the tunnel operating conditions were nominally the same; only the engine operating conditions were varied. Many of these runs were discarded after a visual inspection for sufficiently long segments of nominally statistically stationary data from which pressure spectra could be calculated. From the surviving test runs, three were chosen as representative and will be discussed in some detail.

Pressure spectra were calculated using standard time-series analysis procedures described by Hardin (ref. 6) and implemented with the same software as was used in reference 4 (see that reference for a discussion of the specific software routines).

Data Analysis

An immediate goal of the data analysis was to correlate events in the pressure time histories at different gage locations with inlet unstarts. This correlation was done by visual inspection of the pressure time histories and by measurement of shock wave propagation speeds between gage locations. Also, measurements of peak-to-peak fluctuating pressures yielded rough estimates of the rms fluctuating pressure differences between gage locations.

Pressure spectral estimates were obtained during those portions of the pressure time histories that, on a visual inspection basis, approached statistical stationarity. Because the gages were mounted in recessed cylindrical cavities, directly measured power

spectra were subject to distortion from cavity resonances, flow interaction with the port, and self-noise contamination generated by the grazing flow over the cavity port. Thus, some attention was given to these effects.

Tijdeman and Bergh (ref. 7) describe a correction procedure whereby the distortion effects alluded to above were correctly modeled for subsonic flow and low frequencies. A modified version of that model was investigated for the high-speed flow, high-frequency case; this modification was based on a suggestion by Heller and Widnall (ref. 8). Application of Heller and Widnall's modification to the Tijdeman and Bergh model for the range of aerothermal flow parameters and excitation frequencies of interest in this investigation resulted in corrections of not more than ± 1.5 dB. Because this correction was well within the random measurement error range, it was not applied to these results. Essentially, the model calculates the transfer function between the fluctuating pressure incident on the cavity port and that at the face of the recessed gage. It takes into account the damping effect of viscous losses on the wall of the cavity and the pressure drop caused by the interaction of the steady flow and the fluctuating flow into the cavity port. (See appendix B for a more thorough discussion of the model.)

The effects of spatial averaging on the finite sensing area of a transducer (in this case the port area) will reduce its effective sensitivity with increasing frequency. Blake's review of sensor spatial averaging effects (ref. 9) suggests that for port diameters used in this investigation, loss of signal from spatial averaging was less than 1 dB for the highest frequency of interest (5 kHz) in this investigation.

Power spectral densities (PSD's) were calculated for selected portions of time histories with acceptable statistical stationarity. Acceptable stationarity is largely an engineering judgment based on a comparison of the means and variances of data blocks composed of a segment of pressure time history subject to PSD analysis. In fact, no pressure time histories were ideally stationary. However, every effort was made to limit the analysis region such that the trade off between statistical accuracy and nonstationarity effects was a balanced one. To improve statistical precision, the statistically stationary portions of the time histories were subdivided into contiguous data blocks of 4096 samples. Thus, for a sampling rate of 15.6 kHz, the data blocks are 0.262 sec long.

These blocks were very nearly statistically independent as determined by the first zero crossing of the autocorrelation function. Subdivision of a data

record into N_B statistically independent data blocks, each of length t_B , allows power spectral density estimates taken from each block to be treated as a chi-square random variable with two degrees of freedom. Thus, the larger N_B can be made, the smaller the statistical uncertainty. In other words, the accuracy of the power spectral estimate $\widehat{S}_p(\omega)$ depends upon finding a sufficiently long stationary segment of data to provide a value of N_B that is as high as possible. Generally, N_B ranged from 7 to 31 blocks. Thus, the statistical accuracy of $\widehat{S}_p(\omega)$ was somewhat variable. With 7 blocks, the probability is 80 percent that $\widehat{S}_p(\omega)$ lies between 0.66 and 1.72 of the true value; for 31 blocks the probability is 80 percent that the estimate lies between 0.81 and 1.30. The power spectral estimates were averaged over these N_B blocks as follows:

$$\widehat{S}_p(\omega) = \frac{1}{N_B} \sum_{j=1}^{N_B} \widehat{S}_p^j(\omega) \quad (1)$$

The trade off for reducing statistical uncertainty by increasing N_B is reduced frequency resolution bandwidth of the spectral estimate for a given total time length t_{total} . This trade off is quantified by the equation

$$k = 2\Delta f t_{\text{total}} \quad (2)$$

where k represents the statistical degrees of freedom and Δf is the resolution bandwidth associated with the data block length t_B ($\Delta f = 1/t_B$).

The discrete Fourier transform estimate for each data block was computed from

$$\widehat{S}_p^j(\omega) \approx \frac{\Delta t}{2\pi} \sum_{n=0}^{N-1} p(n) \exp(-i\omega n \Delta t) \quad (3)$$

where $N = 4096$. In this equation a ‘‘boxcar type’’ data window has been assumed that is unity over t_B and zero elsewhere. Thus, the final spectral estimate obtained by averaging the individual spectral estimates from N_B data blocks is given by

$$\overline{S}_p(\omega) = W_s |\widehat{S}_p(\omega)|^2 \quad (4)$$

where W_s is a correction factor that accounts for the data window and experimental calibration factors. The rms pressures were computed by an integration of the area under $\widehat{S}_p(\omega)$ from 1.9 Hz to 5 kHz. (The contribution of the frequency band centered at 0 Hz was excluded to avoid nonstationarities arising from slow variations of the mean static pressure.)

Statistical Analysis

In some instances, it is useful to compare measured probability density functions with normal den-

sity functions based on the computed mean and variance of the time history data as follows:

$$\mu_1 = \frac{1}{NN_B} \sum_{n=1}^{NN_B} p(n) \quad (5)$$

$$\sigma^2 = \frac{1}{NN_B - 1} \sum_{n=1}^{NN_B} [p(n) - \mu_1]^2 \quad (6)$$

Note that these statistical parameters are computed across all NN_B values of the N_B contiguous data blocks of N data points each. Another measure of the rms pressure is the square root of the variance. However, this measure implicitly involves the mean as indicated in equation (6). Thermal transients have been shown to alter the mean values recorded with gages of the type used in this study; therefore, it was decided that an alternate form of this value should be calculated from the power spectral density with the contribution from the mean excluded. In all probability density functions shown in the section ‘‘Discussion of Results,’’ the tabulated overall sound pressure level (OASPL) was taken from the variance. In most cases, this value is close to the OASPL computed from the PSD (denoted (OASPL)_{PSD}); however, there are cases where the value is substantially different. This difference is an indication of a changing underlying mean value (either ‘‘true’’ or thermally induced) or a lack of stationarity. When they arise, these situations will be noted.

Skewness, which measures asymmetry in the density function, is calculated from

$$\alpha_3 = \mu_3/\sigma^3 \quad (7)$$

where μ_3 is the third moment of the pressure probability density about the mean normalized by the third power of the standard deviation σ . Kurtosis, which measures peakedness or flatness of the density function, is calculated from the fourth moment normalized by the fourth power of the standard deviation; thus,

$$\alpha_4 = \mu_4/\sigma^4 \quad (8)$$

where μ_4 is the fourth moment of the probability density about the mean.

The calculated mean and variance were used to construct a Gaussian probability density function (PDF) against which the measured density function was compared. The measured density function is displayed as a normalized 25-bin histogram centered on the mean static pressure normalized by the rms pressure, as determined from the variance.

The section "Discussion of Results" contains an explanation of deviations in the PDF's from Gaussian that is based upon several simulated time histories generated when a base or dominant pseudo-Gaussian process was perturbed by another whose mean is within the base distribution range but whose variance is much smaller. Such perturbations can be studied by observing changes in skewness and kurtosis when the mean and variance of the perturbing process are altered. A high kurtosis value, relative to 3 for a perfect Gaussian, indicates that the instantaneous pressure remains for a relatively long period near the mean value; a nonzero skewness value, relative to zero for a perfect Gaussian, indicates that asymmetric excursions from the mean occur. For the experienced observer, these statistical parameters offer useful ways to monitor changes in the fluctuating boundary layer pressures that are not readily discernible in the power spectra.

Estimates of Aerothermodynamic Parameters

Aerothermodynamic parameters such as Mach number, unit Reynolds number, static pressure, and temperature were estimated at the various gage locations from measurements of the tunnel operating parameters at the model inlet and from static pressure measurements along the model wall. Estimates of aerothermodynamic parameters for the core flow at each measurement location were calculated on the basis of isentropic flow relationships. These estimates can err on the high side because of total pressure losses through the developing oblique shock wave system. However, for these experiments, this error was not considered serious. For completeness, the isentropic flow relations for a thermally and calorically perfect gas, taken from reference 10 and appropriately manipulated for this work, are given below.

The Mach number M_e at the boundary layer edge over a given gage location is given by

$$M_e = \sqrt{\left(\frac{2}{\gamma - 1}\right) \left[\left(\frac{p_e}{p_t}\right)^{\frac{1-\gamma}{\gamma}} - 1\right]} \quad (9)$$

where p_e is equal to the measured static pressure p_s at a wall port underneath the boundary layer and p_t is the tunnel total pressure at the model inlet plane or tunnel nozzle exit (see fig. 6). The dynamic pressure q_e is computed from

$$q_e = \frac{1}{2} \gamma p_e M_e^2 \quad (10)$$

The static temperature at the boundary layer edge is given by

$$T_e = T_t \left[1 + \left(\frac{\gamma - 1}{2}\right) M_e^2\right] \quad (11)$$

Unlike the static pressure, the static temperature increases through the boundary layer and will approach the adiabatic wall temperature for a nonconducting wall. In the present case the model mass was large and highly conducting, so thermal equilibrium was never reached and the wall temperature remained below the adiabatic value. The ratio of the adiabatic wall temperature to the static temperature in the core flow is given by

$$T_{aw} = T_e \left[1 + R_f \left(\frac{\gamma - 1}{2}\right) M_e^2\right] \quad (12)$$

For a nominal Mach number of 3.5 and a recovery factor R_f of about 0.9, an estimate of the adiabatic wall temperature for the flow through the present model is approximately 1460°R.

Measurements of wall temperature indicated a mean of about 600°R. Thus, the ratio T_w/T_{aw} is about 0.4, which suggests a modestly cold wall condition. The gas density in the gage recess cavities is calculated from the gas law as follows:

$$\rho_{cav} = \frac{p_e}{RT_w} \quad (13)$$

where the gas temperature in the cavity is taken to be T_w but may be considerably higher because of gas exchange with the relatively hot boundary layer.

Discussion of Results

Results from three tests are presented here. These results are representative of the unsteady or fluctuating pressure loads in the GHSE for various operating conditions. During the first test, run 6, batch 7 (R6B7), a thermally induced unstart was captured. This test was interesting because it offered the opportunities to observe an unstart-induced traveling shock wave over a sufficient distance and to determine the shock speed. However, only one gage remained within the measurement range after the unstart. Thus, a second test is presented that also involves an unstart; run 15, batch 6 (R15B6) has data records of sufficient length to provide high-quality PSD's before and after unstart. This run was not as convenient for the determination of the shock speed because the surviving gages were too closely spaced. The third test, run 50, batch 10 (R50B10), was included to study the effects of step increases in the heat release rate without the complicating effects of

an unstart. This test is particularly interesting because it provides evidence of combustion noise apparently propagating upstream in the subsonic portion of the boundary layer underneath the supersonic core flow in the isolator section.

Table I lists information relevant to the test conditions and data analysis results. For each test run, the column entries were divided into four groups; the first vertical column of each group is the gage location number. The second vertical column of the first group is the model calorimeter port designation and nearest electronic scanning pressure (ESP) static pressure port. This information is useful to readers who want to correlate results from this report with those in the generic high-speed engine (GHSE) performance report of reference 3. The third vertical column presents gage location relative to the inlet leading edge, and the fourth vertical column gives the gage recess depth. The fifth, sixth, and seventh vertical columns relate to the specific segment of the measured pressure time history that was analyzed.

The second horizontal group of entries contains the tabulated values of the thermodynamic parameters and is generally self-explanatory with the aid of the symbols list. Vertical columns p_t and T_t are stagnation values of pressure and temperature at the model inlet plane as estimated from tunnel operating parameters. The next vertical column is the static pressure p_e at the boundary layer edge, as determined from static pressure measurements p_s at the wall static pressure ports. These values were acquired from averaging measurements acquired during the indicated time region as listed in the first table grouping. The next two vertical columns, labeled T_e and ρ_e , are computed from the previous columns as discussed in the section "Data Acquisition, Reduction, and Analysis." The last vertical column, ρ_{cav} , is computed from the gas law, with the temperature in the cavity taken to be 600°R as measured by a thermocouple installed in a calorimeter port.

The third and fourth horizontal groups of entries relate to the correlation of unsteady pressure loads data with data for other fluctuating boundary layer loads in the literature. These entries will be referenced as further discussion develops. All dimensional quantities are expressed in British gravitational units.

Run 6, Batch 7 (R6B7)

Figure 8 shows curves for five axial static pressure distributions along the interior top wall of the model for test R6B7 just before and during an inlet unstart that is induced by thermal choking. The table in that

figure lists the time coordinate for each pressure distribution, the corresponding ESP cycle, and equivalence ratio ϕ (i.e., the fuel-to-air ratio divided by the stoichiometric ratio). The column labeled cycle has the same information as the sixth vertical column of the first horizontal group in table I. This information allows the data in the present report to be correlated with the engine performance data of reference 3.

The first three static pressure distributions, indicated by series 1, 2, and 3, correspond to a normally operating engine (i.e., a net thrust production at an approximate equivalence ratio of 0.41). The static pressure rise is roughly linear with distance downstream from the model inlet to about 40 in. At that point, the pressure rise becomes somewhat steeper. This steeper region begins about midway in the isolator section. Maximum pressure occurs in the combustor region and decreases through the nozzle section. Note that mean pressure changes of 2 to 3 psia (about 1.3 percent) occur in the combustor region over about 2-sec intervals; these changes are consistent with variations of about 2 percent in ϕ .

For curves 4 and 5, which correspond to equivalence ratios of 0.492 and 0.581, respectively, the pressure distribution is dramatically different. These curves reflect the unstarted state of the model. The onset of inlet unstart is associated with increased heat release rates as indicated by the higher equivalence ratios (see series 4 and 5 in the figure). The value of ϕ for curve 4 is quite soft because the facility data acquisition system response time is not sufficient to update values of ϕ in real time for this transient condition. For this particular test run, the equivalence ratio threshold for unstart is approximately 0.58. In figures 9 to 14, the analysis is presented of the unsteady pressure loads data along the top wall of the model before and just after unstart.

Figure 9 shows pressure time histories in pounds/square inch at gage locations 1 and 4 for test R6B7. Note that the use of absolute, as opposed to differential, gages allows the high-frequency unsteady pressures to be viewed in context with the relatively slow mean pressure variations. The differences between the mean static pressures of figures 8 and 9 (about 3 psia) at gage location 4 are likely due to temperature effects on the zero shift of the piezoresistive gages as discussed in appendix A. These effects notwithstanding, on the basis of arguments presented in appendix A, the static pressure variations in general were faithfully reproduced.

The pressure fluctuations in figure 9 change throughout the test run, and significant events are indicated in the figure. Pressure fluctuations during

the initial 2 sec are indicative of tunnel and model inlet start transients and are not considered further. At 7 sec, the fuel is initiated, followed by ignition and thrust. The key feature, an inlet unstart, occurs at 13 sec, as shown by the sudden mean pressure increase at gage location 4 and is followed by a similar increase at gage location 1 exactly 0.436 sec later. As the disturbance emerges from the inlet, the signal conditioner for gage location 1 is driven out of range. These pressure increases indicate an upstream propagating shock that passes out the model inlet. The average upstream propagation speed of the shock between the two gages, relative to the model reference frame, is about 7.1 ft/sec. As is evident at gage location 4, the fluctuating pressures increase dramatically after the inlet unstart. The fuel is turned off at 17 sec and the facility is shut down at about 20 sec.

A few points should be made concerning the measured unstart phenomenon. First, the relatively slow speed at which the shock moves through the inlet indicates a potential for using control mechanisms to reverse the direction of the moving shock wave before the unstart process is complete. Also, the consequence of an unstart is not just the increase in static pressure, but is also the exposure of an increased area of the engine to high fluctuating loads.

If a researcher wishes to estimate power spectra and other statistical parameters of interest, it will not be possible to satisfy the statistical stationarity requirement for arbitrarily selected portions of the pressure time histories as shown in figure 9. Therefore, regions of the pressure time histories were chosen on the bases of interest and relatively good stationarity for a sufficient length to provide meaningful averages of the PSD estimates over several contiguous data blocks. Two or three regions were chosen for all three runs and are indicated by shaded regions in the pressure time history plots. Specifically, relatively good statistical stationarity is observed over intervals I and II from 3.7 to 5.5 sec and from 10 to 12.3 sec, respectively. These time interval regions are further analyzed. All aerothermodynamic entries in table I are averages taken over these regions.

Figure 10 shows a magnified segment of the time history, 32 msec long, in region I at gage location 4. If the pressure fluctuations are described approximately by a Gaussian process, then pressure excursions remain within 3 standard deviations of the mean more than 99 percent of the time. Therefore, estimates of the rms pressures can be obtained by taking one-sixth of the peak-to-peak pressure fluctuations. Thus, a conservative estimate that is based on the indicated 8-msec time slice indicates a peak-to-peak value of at least 0.4 psia or

147 dB (re 20 μ Pa). A more accurate value obtained from the PSD over the 1.8-sec region I yields an $(OASPL)_{PSD}$ of 153.1 dB. Thus, the particular peak-to-peak estimate illustrated in the figure is conservative by about 6 dB. Similarly, after unstart and before fuel shut off, peak-to-peak pressures approximate 7.0 psia (172 dB). The $(OASPL)_{PSD}$ for the 2.5-sec region III is 178.6 dB.

Part (a) of figures 11 and 12 presents pressure spectra in two different formats at gage locations 1 and 4 and for regions I and II of the pressure time histories. Pressure spectra for time region III (inlet unstarted) are not included because the gage at location 1 was out of range. The same data are then shown in part (b) of the figures nondimensionalized for the flow velocity at the boundary layer edge U_e , the rms value of the fluctuating pressure p_{rms} , and the boundary layer displacement thickness $\delta^* = 0.23$ in., as estimated at the tunnel nozzle exit. The rms pressure is obtained by a summation of the contributions from each frequency bin Δf , except for the one centered at 0 Hz. In this way the contribution from the mean value is excluded. The result of this calculation is listed as $(OASPL)_{PSD}$ in the appropriate figures. All the power spectra are presented in this format to allow convenient comparisons with typical presentations of flat-plate boundary layer data.

Figure 11(a) shows PSD's expressed in decibels at gage locations 1 and 4 (see fig. 9) for region I. The PSD analysis extends to nearly 8 kHz to verify antialiasing filter roll off beyond 5 kHz. Beyond about 6 kHz, signal conditioning (discretization) noise floors, which are different for each instrumentation channel, mask any further filtering action. These data above the filter cutoff are included to aid in judging the quality of the data below 5 kHz. For this case, the data below 5 kHz are well above the respective channel noise floors and are apparently uncontaminated by aliasing effects. Because of the varied ways these spectra may be affected by other contaminating influences associated with recessing the gages, the reader is urged to consult the appendixes of this report.

In region I, the inlet is started, but no combustion occurs. Except for the maxima near zero frequency, the general characteristic of the spectrum is that expected for a turbulent boundary layer. The maxima near zero frequency may indicate upstream disturbances in the tunnel or low-frequency model vibration. Low-frequency vibration, however, may be the less likely contributor. Also, a relatively sharp, localized peak at 0.9 kHz is noted at reference gage location 1 on the tunnel nozzle lip. A broad peak is barely

perceptible near 2.1 kHz at gage location 4. The possibility that either of these peaks is caused by gage mount vibration or organ pipe resonances of the gage recess cavity is discounted by arguments presented in the appendixes. For example, the first organ pipe resonance would be expected at 4.6 kHz if the gas temperature in the recess cavity were 600°R. Also, the pressure transfer correction model, discussed in appendix B, predicts a nearly complete damping of such resonances. Also, at 5 kHz, the level at gage location 4 has fallen only about 7 dB relative to the broad peak at 2 kHz. Clearly, much of the high-frequency energy above 5 kHz has not been captured.

Comparisons of the two spectra show that the level at reference location 4 ranges higher than that at reference location 1 by 15 to 30 dB, whereas the overall level at gage location 4 is 18.7 dB higher than at gage location 1. From table I, the static pressure increases 5.24 times between the two locations, and p_{rms}/p_e increases from 1.13 to 1.86 percent. These two factors account for the 18.7-dB increase in the rms pressure at gage location 4 relative to that at location 1. The static pressure increase is associated with the flow compression. The increase in p_{rms}/p_e may be associated with the interacting shock and boundary layers. Combustion is not involved in these spectra because there is none in this time frame.

Figure 11(b) shows the same spectra in nondimensional form. Because each spectrum is normalized by its own rms pressure, the large differences alluded to above are largely suppressed. In this plotting format, the differences between the two spectra are more clearly delineated. Also, the log-log scale emphasizes spectral detail at the lower frequency range at the expense of detail at the higher frequencies. For example, the peak at gage location 1 near 0.9 kHz in figure 11(a) shows up near a reduced frequency of 3×10^{-2} in figure 11(b). The spectrum at gage location 4, 35 in. downstream from the inlet plane, is somewhat more uniform with frequency than is the case for the spectrum at reference gage location 1, which is near the tunnel nozzle exit. In fact, the two spectra cross each other near a reduced frequency of 7×10^{-3} and diverge above that frequency, with the spectrum at gage location 4 nearly 10 times greater at a reduced frequency of 7×10^{-2} , near the filter cutoff frequency. This change in the boundary layer fluctuating pressure spectrum may be associated with the flow compression through the oblique shock in the inlet region.

In the literature dealing with surface pressure fluctuations underneath turbulent flows, the free-stream dynamic pressure (e.g., refs. 11 and 12) is sometimes used to normalize the dimensional power

spectra instead of the rms pressure as was done here. Other investigators use the dynamic pressure at the boundary layer edge as the normalizing factor (e.g., see ref. 11). The rms pressure was used here because it achieved the best possible collapse of the spectra from different gage locations and permitted similarities and differences to be more easily compared.

Refer to table I to change the normalization parameters. For example, if p_{rms} is replaced by q_e in figure 11(b), the PSD scale is multiplied by 2×10^{-6} and 23×10^{-6} , respectively, for gage locations 1 and 4. Also, the spectrum at gage location 1, region I will follow the trend of the normalized spectrum measured on a flat-plate equilibrium boundary layer underneath supersonic flow. References 11 to 13 show that flat-plate spectra contain significant energy to reduced frequencies near 1 for a wide range of flow and boundary layer parameters. Therefore, the present measurements miss at least 1 decade of the high-frequency spectrum. The fact that the spectrum at gage location 4, region I is 14.7 times higher (and might even be higher with the missed portion of the spectrum included) suggests that the boundary layer turbulence grows more than would be the case for an equilibrium boundary layer on a flat plate for similar flow conditions. This assumption is further supported when rms pressure is compared as a percentage of either the mean static pressure or dynamic pressure at the boundary layer edge. Table I shows a significant jump to 1.86 and 2.87 percent of the static pressure at gage location 4 (0.48 and 0.78 percent q_e).

Figure 12(a) shows the pressure spectra at gage locations 1 and 4 in region II where combustion has reached steady state. The spectrum shape at reference gage location 1 is practically identical to that for no combustion (region I) in figure 11(a). The $(OASPL)_{PSD}$ difference of only 0.7 dB between these regions suggests that very little combustion noise was measured at this gage location. At gage location 4, however, the spectrum, although quite similar in general shape and trend to that in figure 11(a), is up to 5 dB higher, starting well below 1.0 kHz and gradually coalescing at the high-frequency end near 5 kHz. Further, the $(OASPL)_{PSD}$ at gage location 4 in region II is 157.4 dB compared with 153.1 dB in region I (no combustion) at the same gage location and reflects a difference of 4.3 dB. This result suggests that broadband, low-frequency combustion noise may contribute to the fluctuating pressure at gage location 4.

As was the case for region I, the gage location 4 spectrum is about 30 dB greater than that at gage location 1 for the higher frequency range starting at

about 1 kHz. The spectral peak, near 0.9 kHz at gage location 1, is diminished somewhat; however, a peak at about 3.2 kHz becomes more prominent. These minor changes provide further evidence that the gages are measuring real pressure fluctuations rather than spurious output from gage mount vibration. As with gage location 4 in figure 11(a), the pressure spectrum for gage location 4 in region II is devoid of the minor spectral peaks evident at gage location 1.

Figure 12(b) shows the same data presented in figure 12(a), but in nondimensional form. The two spectra of this figure are also seen to collapse to a reduced frequency of about 7×10^{-3} , where a divergence begins and continues to the filter cutoff as was the case in figure 11(b). In this case, however, the divergence is more uniform and the broad peak at the reduced frequency of 8×10^{-2} is less noticeable. The pronounced effect of the filter roll off again suggests significant energy in these spectra beyond 5 kHz. It is interesting to compare the spectrum at gage location 4 in this figure with the corresponding spectrum of figure 11(b) for the no-combustion case. There appears to be some increase in the level of the low-frequency spectrum at gage location 4, consistent with the increase in the decibel spectrum in region II (i.e., combustion). Also, the slightly less prominent peak near 10^{-1} is probably a result of the increase in the gage location 4 spectrum between 10^{-2} and 10^{-1} . This finding is consistent with the comparisons on the decibel spectrum and suggests that broadband, low-frequency combustion noise affects the spectrum at the reference gage.

Figures 13 and 14 show the probability density distributions for the pressure time histories at gage locations 1 and 4 and for time regions I and II. The continuous curves are Gaussian probability distributions based on the means and variances as tabulated in the figures. The mean, variance, skewness, and kurtosis of the relevant regions have been calculated from the equations given in sections "Data Reduction" and "Data Analysis." These values were calculated over all the data blocks used in the PSD analysis. The OASPL is calculated directly from the variance as listed. These values are also listed, along with those calculated from the PSD's, in the last grouping of entries in table I. For the present test run, the quantity $(\text{OASPL} - (\text{OASPL})_{\text{PSD}})$ reaches a maximum of 3.9 dB, which occurs for time region II at gage location 1. For the most part, the differences between the two methods of calculating overall sound pressure levels are within 1 dB. The differences between the two methods are likely caused by nonsta-

tionarity in the pressure time histories from slowly varying mean static pressures.

The measured probability distribution in figures 13 and 14 is based on a 25-bin histogram covering the pressure range. Each distribution has been normalized by its respective rms value (obtained from the variance), and the mean has been suppressed.

In figure 13(a), the tabulated values for skewness and kurtosis of 0.15 and 2.96, respectively, suggest that the Gaussian density function describes the statistical properties of the pressure time history to a good approximation in region I. Visual inspection of the data distribution for the Gaussian curve would suggest an inconsistency between the calculated skewness and the apparent visual skewness. However, contributions to skewness are weighted by the cube of deviations from the mean. Thus, a careful pairing of symmetrically occurring data points away from the mean indicates relatively larger numbers of bin counts greater than 1 standard deviation from the mean \bar{p} ; thus, $p(t) - \bar{p}/p_{\text{rms}} = 1$.

However, bin counts beyond 3 standard deviations are of little significance because there are so few of them. Another item of interest in figure 13(a) is the tabulated OASPL of 135.2 dB. This value in no way depends on the Gaussian distribution assumption. It is computed directly from the variance of the measured time history values. The $(\text{OASPL})_{\text{PSD}}$ obtained from the PSD was 134.4 dB.

In figure 13(b), the PDF is shown for the same gage location but for region II of the time history where steady-state combustion occurs. Here the skewness is negligible, but the kurtosis has dropped to 2.70 (still 90 percent of that for a Gaussian curve). The visible data scatter about the Gaussian curve suggests a poorer fit than indicated by the skewness and kurtosis values. However, the apparent scatter is fairly sensitive to histogram bin width selection. For instance, if the bin width were greater, the apparent scatter distribution would change for adjacent values that are greatly different. The relation of visual scatter to calculated values of kurtosis and skewness becomes increasingly difficult when the apparent data scatter becomes significant as in figure 12(b); however, if the data pairs away from the mean are compared, the symmetry appears to be controlled mainly by contributions between 1 and 3 standard deviations from the mean. The OASPL for time region II is 139.0 dB as calculated from the variance (135.1 from PSD). This difference very likely reflects a lack of statistical stationarity. The PSD-based value is probably more accurate.

At gage location 4 (figs. 14(a) and 14(b)), the PDF's are much more peaked (i.e., kurtosis greater than 3) and more skewed than at gage location 1. Therefore, the pressure excursions are more clustered near the mean value, as is evident in the figures. In regions I and II, the tails of the PDF's show pressure excursions ranging from 3 standard deviations below to 10 standard deviations above the mean in region I. Even a few significant excursions from the mean pressure, particularly when an engine is operating at nearly optimal conditions, may initiate the unstart condition. Thus, although the data for gage location 4 appeared mostly Gaussian, the excursions of approximately 10 standard deviations above the mean may provide insight into the stability of the airflow through the engine (i.e., resistance to unstart).

In region II, the skewness is about 3.7 times greater than in region I and the kurtosis is about 2.7 times greater. These comparisons indicate that the pressure time histories become less Gaussian away from the inlet plane and the deviation from Gaussian becomes even more apparent when combustion occurs, in spite of the fact that the measurements are well upstream of the combustor and the core flow is supersonic. (Note also the listed overall levels of 153.2 and 157.8 dB calculated from the respective variances compared with 153.1 and 167.4 dB obtained from the corresponding pressure spectra previously described. The difference of nearly 10 dB in region II again suggests significant nonstationarity for the pressure time history in this region.) This situation is also consistent with the corresponding spectra of figures 11(a) and 12(a). This result suggests that combustion noise contributes significantly even in the inlet section of the model.

Run 15, Batch 6 (R15B6)

Run 15, batch 6 also involved an engine unstart. In this case, data were obtained at gage locations 4, 5, and 6. The gage at location 6, in the combustor region (see fig. 6 and table I), survived long enough to acquire meaningful data during the combustion process. Figure 15 shows four static pressure distributions along the model top wall before and after unstart in a similar format to figure 8. Also, the ESP system obtained a sequence of pressure distributions less than 1 sec apart that shows the progressive static pressure distribution changes during the unstart process. Series 1 and 2 are representative of static pressure distributions during normal model operation at equivalence ratios of 0.414 and 0.422, respectively. As the equivalence ratio approaches 0.5, the pressure changes as it did in figure 8, but with substantially different details.

Figure 16 shows the pressure time histories at gage locations 4, 5, and 6 and significant events in the test run. In this test, a third time history region is examined. This region occurs after the unstart event. Also, gage location 6 was out of range for pressure fluctuations corresponding to region I.

Figures 17(a) and 17(b) show pressure spectra comparisons, expressed in decibels and nondimensional form, respectively, at gage locations 4 and 5 in region I before combustion was initiated. These spectra show similar trends, with the levels at gage location 5 slightly higher (fig. 17(a)) except near 2 kHz, where the gage location 4 spectrum peaks above that at gage location 5. Gage locations 4 and 5 were recessed to the same depth and the mean flow conditions were nearly the same over both gages. Therefore, any masking effects due to self-noise should be manifested to about the same degree in both spectra. Thus, the observed differences in spectral detail strongly indicate that self-noise did not significantly contribute to these spectra. Consistent with the trend established between gage locations 1 and 4, the $(\text{OASPL})_{\text{PSD}}$ increases from 153.4 to 156.8 dB. The nondimensional spectra again show similar trends, with gage location 4 levels exceeding those at gage location 5 to a reduced frequency of about 10^{-2} .

Figure 18 shows a comparison of spectra at gage locations 4, 5, and 6 for region II during combustion. Combustion apparently causes the spectra at gage locations 4 and 5 to increase ($(\text{OASPL})_{\text{PSD}}$'s of 155.1 and 165.2 dB, respectively); the greater increase occurs at gage location 5, with a consequent distinct separation between the spectra at gage locations 4 and 5 across the entire frequency range. Also, except for the region below 2 kHz, the spectrum at gage location 5 is similar in trend to that at gage location 5 before combustion. The core flow is supersonic in isolator section gage locations 4 and 5; therefore, combustion noise apparently propagates upstream through the subsonic part of the boundary layer to reach gage locations 4 and 5. More data are presented below to further support this contention. At gage location 6, in the combustor, the spectrum is characterized by five tone-like peaks to about 1.5 kHz and by a broad peak at about 2.4 kHz. Above 2.4 kHz the levels are generally 10 to 20 dB higher than at gage location 5 across the entire spectrum, with an $(\text{OASPL})_{\text{PSD}}$ of nearly 180 dB.

Figure 18(b) shows the same data in nondimensional format. The spectra for gage locations 4 and 5 collapse about the same as in test R6B7. However, the spectrum for gage location 6 deviates significantly

from the trends for gage locations 4 and 5; this response suggests that combustion noise in fact significantly contributes to this deviation as well as to that between gage locations 4 and 5.

Figure 19 shows spectra at gage locations 4, 5, and 6 taken in region III of the pressure time history after the inlet unstarted but before combustion ceased. After an unstart, the flow was subsonic throughout the model interior. The interesting feature here is the high spectrum levels at gage location 4 ((OASPL)_{PSD} of 177.5 dB and most distant from the combustor) relative to those at gage location 5 ((OASPL)_{PSD} of 167.5 dB). This phenomenon may be generated by acoustic coupling of the combustion process with longitudinal acoustic modes in the engine model. The standing waves resulting from such resonances may cause localized increases in the fluctuating pressure levels. Also, the spectrum for gage location 4 does not start to roll off until about 5.8 kHz, which suggests a large spectral peak in this region that the low-pass filter did not attenuate sufficiently to avoid some aliasing back into the region to about 4.2 kHz. Thus, although the accuracy of the spectra for gage location 4 in this figure is certainly compromised, the test results do suggest significant energy beyond 5 kHz; therefore, the overall levels stated in this report are conservative. The same data are presented in nondimensional form in figure 19(b). Again, differences in these spectra are likely associated with combustion noise as previously discussed.

Figures 20 through 22 show PDF's for gage locations 4, 5, and 6 for regions I, II, and III in the same format as for the previous test run. These PDF's exhibited the same general responses as did those for test R6B7 and will not be discussed in individual detail. It should be noted, however, that the highest rms sound pressure level of 180.3 dB was recorded at gage location 6 with low heat release (see fig. 22(a)). Also, a level of 178 dB was achieved at gage locations 4 and 6 in the unstart condition (region III). As previously stated, these levels are almost certainly conservative in that significant contributions from frequencies above 5 kHz were filtered out at the data acquisition stage. Further, even though an acoustician would view the fluid dynamic processes as quite nonlinear, the PDF's at gage location 6 in the combustor, both during normal engine operation with combustion and in the unstart condition, are well approximated by a Gaussian process (see fig. 22(b)). It should also be noted that the magnitude of the excursions from the mean was similar for all three gages and time regions.

Run 50, Batch 10 (R50B10)

The objective of run 50, batch 10 was to measure changes in fluctuating pressure levels from a sudden step change in the fuel flow and, thus, the heat release rate. In this test an inlet unstart was avoided. Figure 23 shows the top wall static pressure distributions before, during, and after the step increase in heat release rate. Figure 24 shows a comparison of pressure time histories at gage locations 2 through 6, along with the pressure time history for a transducer installed in the fuel flow line. The time scale of the ESP was not completely synchronized to the pressure recording system that logged fluctuating pressures. Also, the gage at location 2 was mounted in an "infinite-line" configuration, similar to that presented in reference 14. This configuration was chosen to provide additional thermal protection.

Figures 25 through 27 show comparisons of the pressure spectra at gage locations 2 through 5 for regions I (no heat release), II (low heat release), and III (high heat release). These figures give evidence of combustion noise propagating upstream through the boundary layer. In particular, the pressure spectra shown in figure 27 show peaks at gage locations 4, 5, and 6 that gradually increase in frequency in the gages nearest the combustor region. Again, note that the change in gage recess depth is small compared with an acoustic wavelength and thus does not sufficiently explain these shifts.

Figures 28 through 32 show the PDF's at gage locations 2 through 6 for regions I, II, and III. Again, the same format was used as in previous PDF's. The overall level for the high heat release region reaches 181 dB (see fig. 31(c)) at gage location 5 as opposed to gage location 6 in the combustor. This somewhat surprising result is consistent with the (OASPL)_{PSD} computed from the PSD (171.5 dB and 167.7 dB at gage locations 5 and 6). It is interesting to note that the magnitudes of the excursions from the mean varied significantly versus location and heat release. This situation was especially true at gage location 2, where the scales of the plots had to be increased to include all excursions from the mean. Although some excursions were quite large, the engine never unstarted. This finding indicates that the engine was operating in a stable mode that was not easily disturbed.

Table I summarizes all the key aerodynamic parameters and rms fluctuating pressure data at the various gage locations. The entries in the table are useful for a comparison of the results of this investigation with those from other investigations (e.g., refs. 11 through 13). The (OASPL)_{PSD} and the

OASPL computed from the PDF variance generally agree well, as shown by the last three column entries for the last entry groupings. The agreement is particularly good for tests R6B7 and R15B7. For test R50B10, however, the differences are generally greater (to 12 dB), especially in high heat release region III. These differences are likely attributable to the relatively high degree of statistical nonstationarity in the pressure time history data in these regions, and that nonstationarity also affects the accuracy of the OASPL as computed from the PDF. Thus, the $(\text{OASPL})_{\text{PSD}}$ computed from the PSD is likely more accurate.

Table I also shows that the unit Reynolds number increases from the inlet toward the combustor as the Mach number decreases. The ranges for the Mach and Reynolds numbers compare approximately with a portion of data in reference 12; in that reference the Mach and unit Reynolds numbers ranged from 1.4 to 2.5 and from 7.2×10^6 to 9.4×10^6 , respectively, to give rms pressures on a smooth tunnel wall from 0.2 to 0.4 percent q_e compared with the present data for which rms pressure ranged from 0.13 percent q_e at the model inlet to 7.5 percent q_e in the isolator section. However, the rms pressure normalized by the mean static pressure ranged from 0.32 to nearly 17 percent, which is comparable to rms pressures of 5 to 24 percent of the mean static pressure reported in reference 13 for a flat plate in a hypersonic boundary layer flow ranging from Mach number 5.2 to 10.4. Laganelli, Martellucci, and Shaw (ref. 11) show a comparison between a semiempirical prediction of rms pressures and measured data for attached turbulent boundary-layer flows for Mach numbers up to 10. Although much scatter is evident, both theory and experiment show a trend of decreasing p_{rms}/q_e with increasing Mach number. In no case does measured or predicted p_{rms}/q_e exceed 1 percent. Therefore, the increasingly complex flow dynamics affects the rms pressure normalized by dynamic pressure which departs significantly from similar flat-plate data described in references 11 and 12.

Figure 33 graphically summarizes all values of $(\text{OASPL})_{\text{PSD}}$ for the three tests and time regions in relation to gage location. At each gage location, the values of $(\text{OASPL})_{\text{PSD}}$ for the three time regions (I, II, III) are plotted from left to right. However, although a given time region designation is only a chronological ordering and does not consistently reference an engine operation state, these regions do include engine unstart conditions. The value of $(\text{OASPL})_{\text{PSD}}$ generally increases with gage location from the engine inlet. The data can be viewed as occupying a band of less than 30 dB at each gage

location, ranging from 131 dB just upstream of the engine inlet to nearly 180 dB near the combustor.

The last two figures (figs. 34 and 35) depict the skewness and kurtosis values versus axial distance (and gage location), again for all three tests and time regions. To keep the scaling acceptable, two kurtosis values were excluded (89.14 and 21.65 for test R50B10, gage location 2, regions II and III, respectively). Perhaps the most intriguing feature of these figures is that the data points were significantly non-Gaussian at gage locations 2 and 4, which were positioned at the start of both the inlet and the isolator. Thus, the non-Gaussian plot is possibly a reflection of changes in the shock wave structure where the wall angles change. Results of recent research (as yet unpublished) with a wedge on a flat plate indicate that this premise may indeed have some foundation. However, more data must be analyzed to determine the validity of this theory.

Recommendations for Future Investigations

The fluctuating wall pressure data in this report result from an exploratory investigation. Key issues were compromises in frequency response and dynamic range associated with the recessed transducers to achieve thermal protection. For frequencies to about 5 kHz, recession depths to about 2 in., and flow stagnation temperatures to about 1600°R, this approach appears possible. The gages were recessed in a massive heat-sink model with a ratio of about 0.4 for the wall to adiabatic wall temperature.

The high-speed flow over the gage recess ports may inhibit or dampen the organ pipe resonance of the recess cavities without generating excessive self-noise that could mask the desired fluctuating pressure measurements. However, measurements with both recessed and flush-mounted transducers should be performed to quantify any distorting effects of the open recess port on the spectrum, especially at the higher frequencies, or of small turbulence scales.

Experiments also should be conducted to validate Tijdeman and Bergh's transfer function (both amplitude and phase) with Heller and Widnall's correction for supersonic flows. That validation may make it possible to measure space-time correlations in high-temperature flows with recessed transducers.

Conclusions

This report has documented the results of an exploratory experiment to measure fluctuating wall pressures on an interior wall of a generic scramjet engine model. The tests described here were part

of a comprehensive series of performance tests conducted in the Langley Combustion-Heated Scramjet Test Facility, which can simulate Mach number 4 flight conditions at altitudes ranging from 57 000 to 86 000 ft. A key feature of the fluctuating pressure measurement approach was to recess the piezoresistive pressure gages relative to the interior wall surface to protect them from the high-enthalpy flow. Although this procedure forced a careful interpretation of the data, the systematic error introduced by the recess apparently is not greater than about 1 dB. The measurements revealed several significant findings:

1. The quality of the measurements suggests that recessed pressure transducers can be successfully employed to obtain meaningful fluctuating wall pressure data to at least 5 kHz in a hostile flow environment with a tolerable transducer mortality.
2. On the model wall near the inlet plane, root mean square (rms) pressures normalized by the local dynamic pressure at the boundary layer edge are comparable to those measured for attached, equilibrium boundary layers on flat plates for similar Mach and unit Reynolds number ranges.
3. Pressure spectra generally are like those reported for flat plates near the model inlet, but are increasingly characterized by sharper peaks with increasing distance from the inlet plane. This profile is especially true near the combustor. These spectral peaks are apparently associated with the combustion process.
4. With increasing distance from the inlet plane, including the isolator section, the rms pressures range to 7.8 percent of the dynamic pressure at the boundary layer edge for both normal engine model operation and the unstart condition. These fluctuating pressures are significantly greater than the upper limit of about 1 percent as reported in the literature on measurements for attached,

turbulent boundary layers on flat plates for Mach numbers 0.4 to 10. Also, semiempirical theoretical predictions for compressible, turbulent boundary layers over flat plates indicate decreasing p_{rms}/q_e with increasing Mach number, with an upper limit approaching 1 percent at subsonic Mach numbers. These comparisons suggest that the fluid dynamics processes (such as interacting shock and turbulence and combustion noise) are more complex in producing scramjet fluctuating wall pressures than for flat-plate boundary layers.

5. Comparison of pressure spectra at gages in the isolator section before and after increased heat release provides compelling evidence of combustion noise propagating upstream against the supersonic core flow.
6. During the engine unstart process, the upstream shock wave propagates at about 7 ft/sec. Therefore, direct structural loading from pressure jumps associated with the unstart shock is likely benign relative to structural damage.
7. On a decibel scale (re 20 μ Pa), overall sound pressure levels range from 131 dB near the inlet plane to 180 dB just upstream of the combustor before an unstart condition. After an unstart, limited data suggest that a maximum level of 180 dB was not exceeded, although the spatial distribution of maximum levels may be different with higher levels extending into the isolator section, presumably because supersonic core flow was absent.

All data presented in this report are subject to the systematic and random measurement errors discussed at length in the report and the appendixes.

NASA Langley Research Center
Hampton, VA 23681-0001
September 25, 1992

Appendix A

Transducer Characteristics

The transducer element for the high-frequency gages used to measure fluctuating pressure loads in this test was a piezoresistive transducer bonded to a metal diaphragm. The gage was packaged in a miniature, ruggedized case, capable of operating at up to 500°F. The gages were installed in the generic, high-speed engine (GHSE) with specially designed inserts to take advantage of existing calorimeter ports. A typical insert is illustrated in figure A1. The gage was mounted in a 0.159-in-diameter channel of the calorimeter insert as indicated in the figure. That insert was then flush mounted into the top wall of the GHSE model. This arrangement formed the recess gage mount used at all measurement locations in the GHSE model. The gages were recessed from 0.78 in. to 1.97 in. deep. Other relevant specifications for the gages are given below.

Pressure range, psia	100
Nominal sensitivity, mV/psia	0.75
Combined nonlinearity, hysteresis, and repeatability at full-scale output, percent	±1
Acceleration sensitivity:	
Perpendicular, percent full scale/g	0.0007
Transverse, percent full scale/g	0.00014
Compensated temperature range, °F	80 to 450
Thermal zero shift, over compensated range, percent	±10
Thermal sensitivity shift, over compensated range, percent	±7
Diaphragm resonance, kHz	80
Diaphragm diameter, in.	0.147

Because both the steady and fluctuating loads were to be measured, absolute gages were chosen instead of the differential type. Generally, the fluctuating pressures were expected to be at least an order of magnitude lower than the steady pressures. A two-point static pressure calibration, spanning the expected range of pressure excursions about the mean pressure at a given gage location, was applied to each gage.

Also, thermal- and acceleration-induced sensitivity shifts were concerns. No vibration data were obtained during the tests. However, because of the massive GHSE model (37.3 slugs), any vibration-induced contamination of the measured pressure fluctuations generally occurs at low frequencies. Based on the stated acceleration sensitivities, a worst case vibration of 100 Hz with an amplitude of 0.1 in. perpendicular to the gage diaphragm would generate a contaminating response equivalent to a 108-dB acoustic pressure. Generally, the low-frequency pressure spectrum levels recorded in the tests were at least 115 dB. Therefore, the contaminating influence of low-frequency vibration was not greater than about 1 dB.

Comparison of mean static pressures measured by the piezoresistive pressure gages and by the facility ESP system during preliminary test runs indicated that the piezoresistive gages underwent substantial zero shifts, apparently due to transient thermal effects. Although the fluctuating pressure was measured for the general local mean static pressure, accuracy of the mean static pressure measurements was not considered crucial. There was concern, however, that measurement accuracy for the fluctuating pressure component would be adversely affected by thermal transients.

To alleviate this concern as well as to compare recessed with flush-mounted gages, an aluminum, cold-flow scramjet model, 12 in. long, was modified to accept pairs of pressure gage inserts at three locations streamwise along a side wall as shown in figures A2 and A3. At each of the three locations a pair of gages could be aligned in streamwise or transverse direction to the flow. The inserts allowed the gages to be recess mounted to varying depths or be flush mounted. Exploratory tests were conducted on this model in the Mach 4 Blowdown Facility to compare flush-mounted with recessed gage dynamic responses in a supersonic flow environment without thermal effects on a flush-mounted gage. Thermocouples were also installed in flush and recessed configurations similar to arrangements in the GHSE to provide information on gage exposure to thermal transients.

The Mach 4 Facility draws air from an outdoor tank farm that is some distance away. The tank farm air may vary daily by at least 20°F, depending upon meteorological conditions. Unfortunately, when the scramjet inlet was started in this facility, the boundary layer loads were not strong enough to generate coherent unsteady pressures that could be acquired by the present gages and analyzed. Therefore, the inlet was purposely unstarted to generate sufficiently high unsteady pressures for analysis (comparison of flush with recessed gages). This procedure provided some insight into the comparison of flush with recessed gage responses; however, the data were inconclusive because the aerodynamic environment was uncontrolled. Nonetheless, the gage responses to the mean static pressure were well matched to the static pressures recorded by the ESP system.

Figure A4 shows the temperature changes at the flush and recessed thermocouples in degrees Rankine versus time in minutes. Tunnel startup is at 1.1 min and tunnel shutdown occurs off scale in this plot. Apparently, thermal equilibrium is achieved at about 3 min into the run. The initial temperature rise of about 10°R may be caused by higher temperature air being purged from the piping system before air from the tank farm is accessed. The initial temperature rise is followed by a steady decline for about 1.5 min, at which time the flush-mounted thermocouple reading rapidly drops, then recovers to about 10°R below the value for the recessed thermocouple. The recessed thermocouple apparently approaches its equilibrium value of about 497°R asymptotically. Generally, these thermal responses were expected except for the sudden transient disturbances at tunnel startup and for the flush-mounted thermocouple near the onset of the equilibrium temperature. After an initial precooling run, however, the model regulates to equilibrium temperature much more smoothly.

Figure A5 shows a comparison of the pressure responses at a flush-mounted gage for a precooled with a nonprecooled model run. Note that the responses during tunnel startup transients are quite different, but in the equilibrium part of the run, the responses are about the same. This difference suggests that the gage temperature-compensating mechanism does perform after the thermal transients subside. To further validate the thermal transient effects on static pressure response, the tip of a gage was suddenly submerged in an ice-water bath under ambient pressure conditions. The results of two consecutive tests, starting with the gage at ambient temperature, are shown in figure A6. The two identical tests produced response transients that were quite different, but again, the equilibrium values approached the ambient pressure. These tests also suggest that the temperature-compensating mechanism for the piezoresistive gages does not provide for accurate pressure responses during a thermal transient. After the thermal transient has diminished and a new temperature equilibrium has been achieved, however, the pressure gages will again give accurate pressure responses.

These tests suggest that both the zero shift A and the dynamic sensitivity B of the gage transfer characteristic may be affected during thermal transients as suggested in figure A7. Note that the parameters A and B are functions of temperature; for example,

$$E = A(T) + B(T)p \quad (A1)$$

The linearized relationships between the fluctuating component of the gage voltage output \tilde{E} , the fluctuating temperature \tilde{T} , and the fluctuating pressure \tilde{p} were of interest here. Equation (A1) is thus linearized and solved for \tilde{E} to give

$$\tilde{E} = (A_T + B_T p)\tilde{T} + B\tilde{p} \quad (A2)$$

where the parameters A and B are implicit functions of time because of their possible temperature dependence. Clearly, the fluctuating pressure is contaminated by the thermal transient if the temperature derivatives A_T and B_T are not zero. The temperature-compensating mechanism will ensure that the parameter B is held constant over the compensated temperature range after thermal transients have subsided. However, these qualitative tests suggest that the compensation does not hold A_T and B_T constant during thermal transients.

It should be noted, however, that the current tests were conducted with the sensors mounted in a massive copper wall. Thus, thermal changes to the flow environment should slowly transfer to the gages. Therefore, although some measurements in this study may contain gradual shifts in their mean value, the fluctuating results should be unaffected.

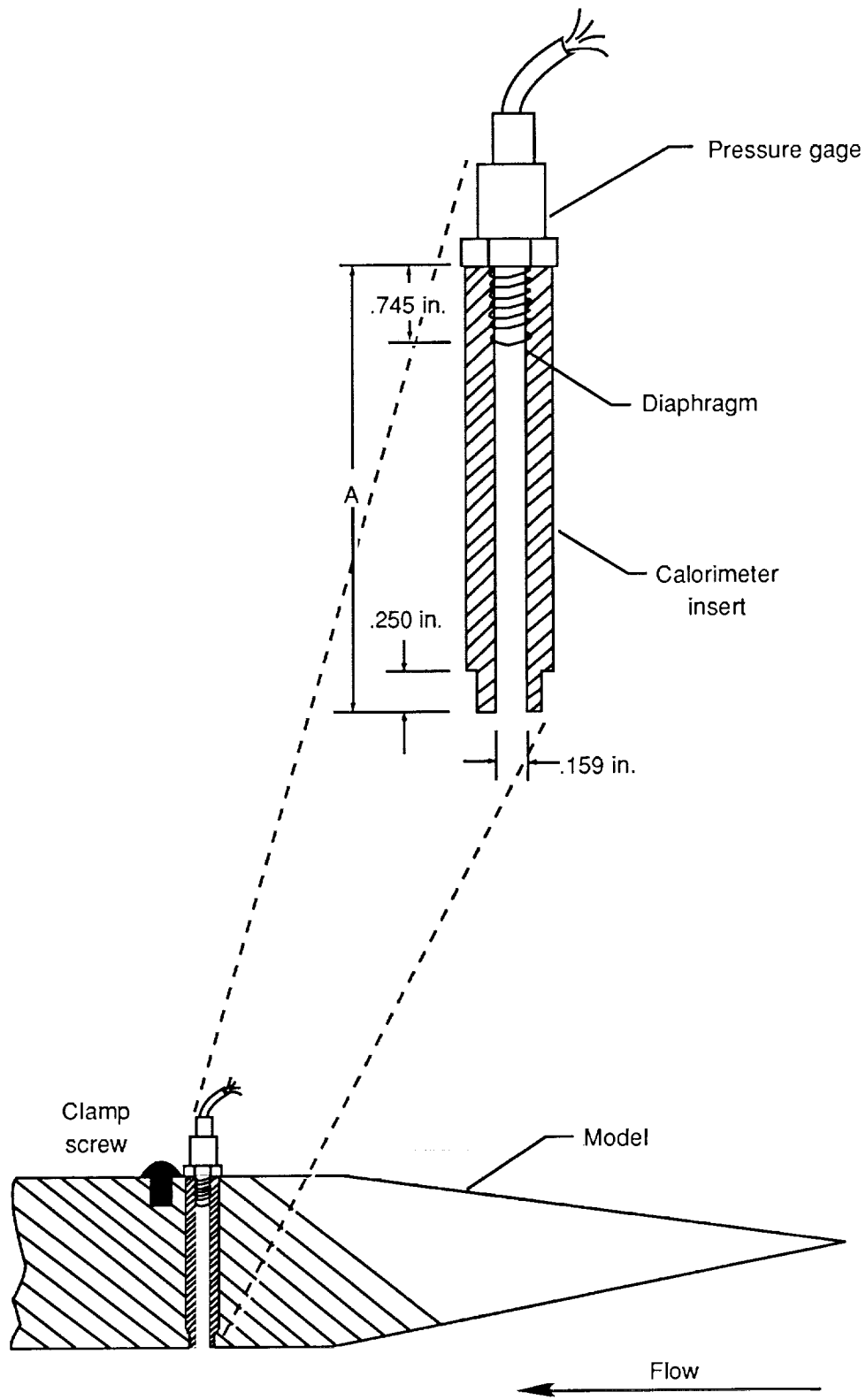
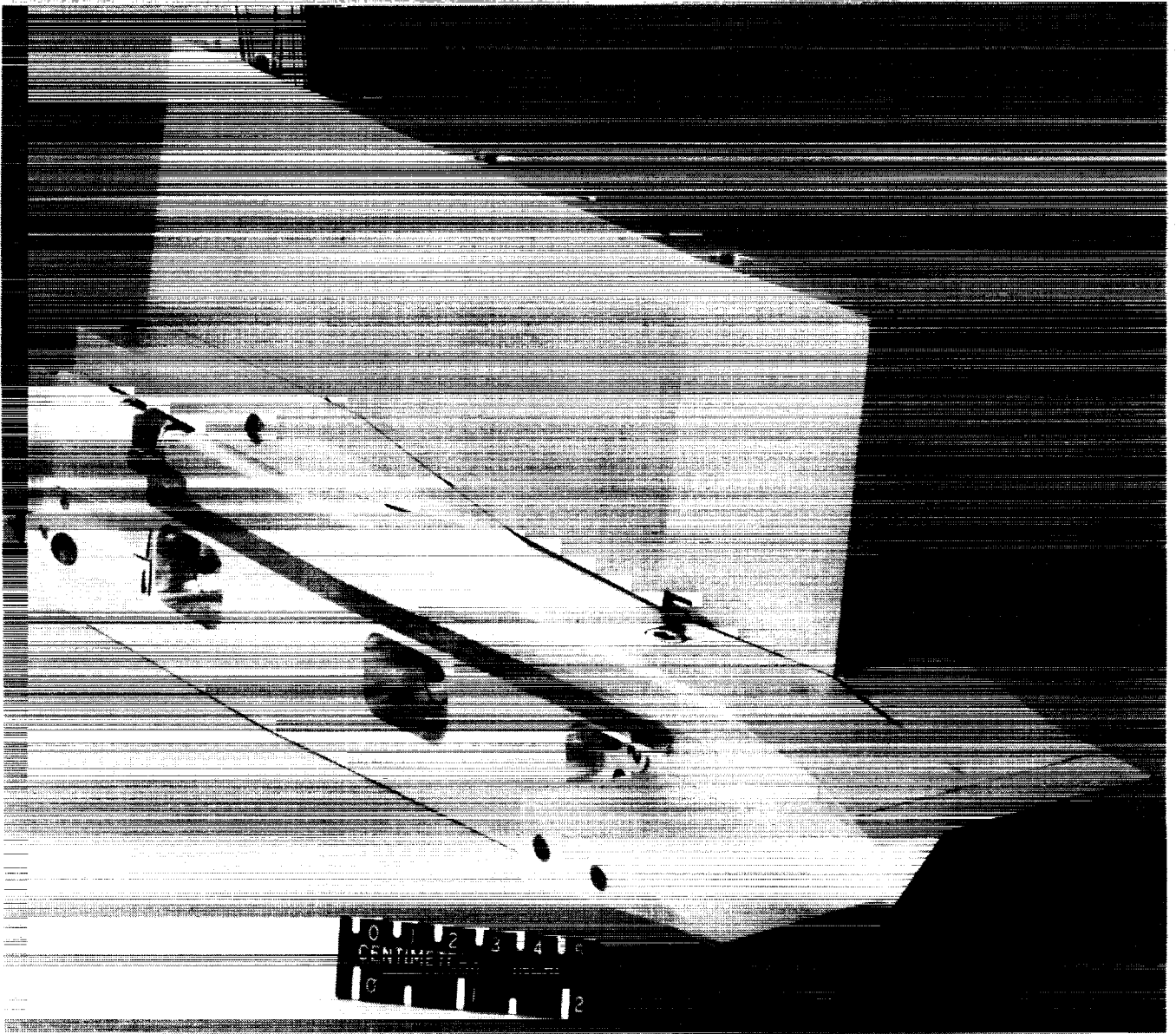


Figure A1. Pressure gage installation.

ORIGINAL PAGE
BLACK AND WHITE PHOTOGRAPH



L-89-6949

Figure A2. Cold-flow scramjet model.

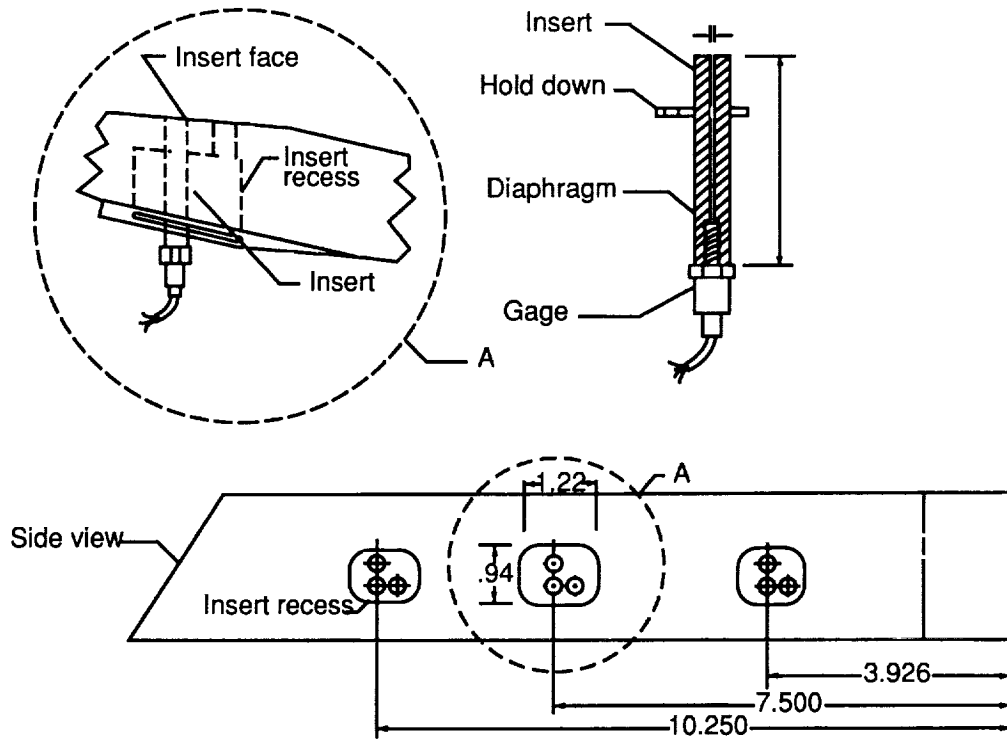


Figure A3. Pressure gage installation in cold-flow scramjet model. Linear dimensions are in inches.

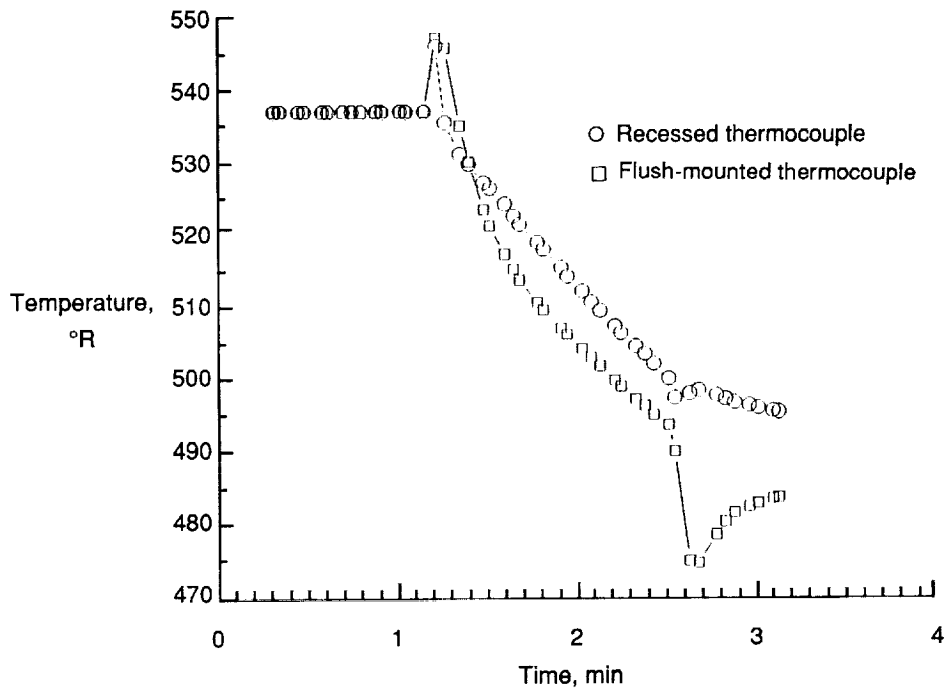


Figure A4. Thermal response of model with no tunnel precooling.

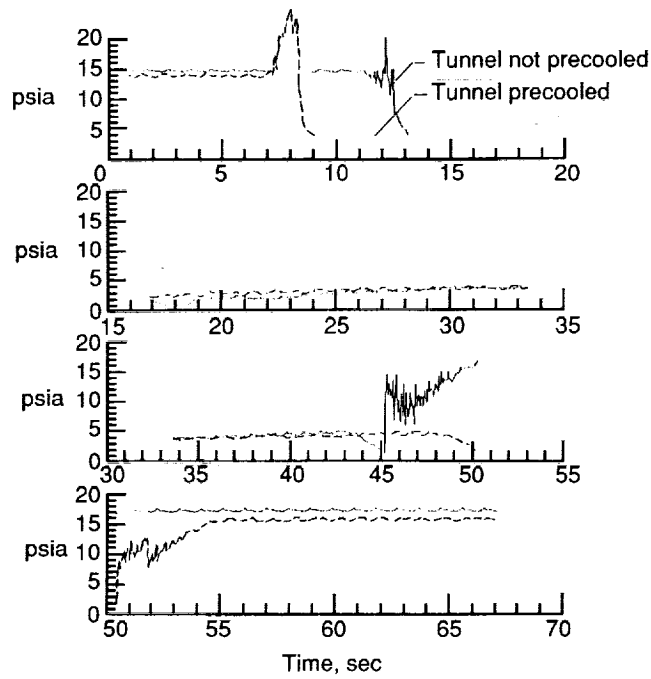


Figure A5. Pressure responses of a flush-mounted pressure gage.

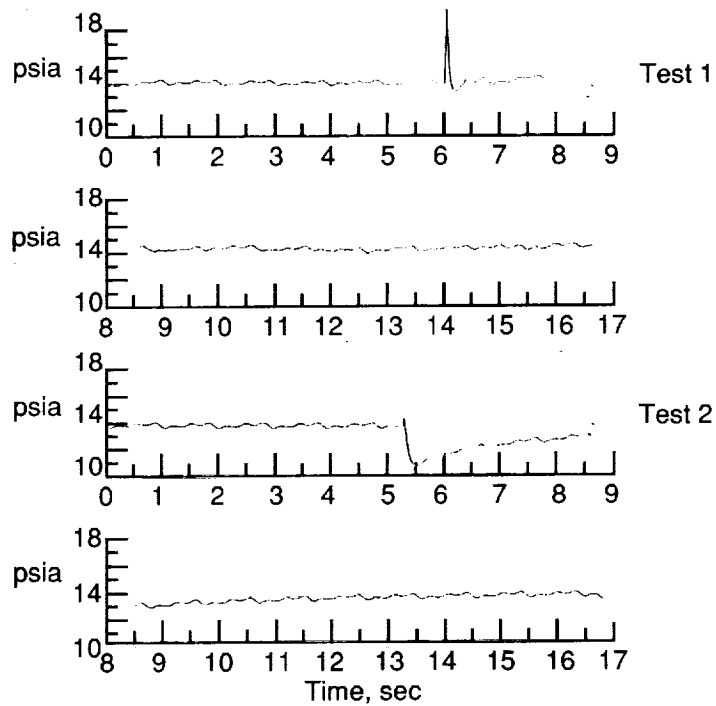


Figure A6. Responses of a pressure gage after consecutive 50° thermal shocks.

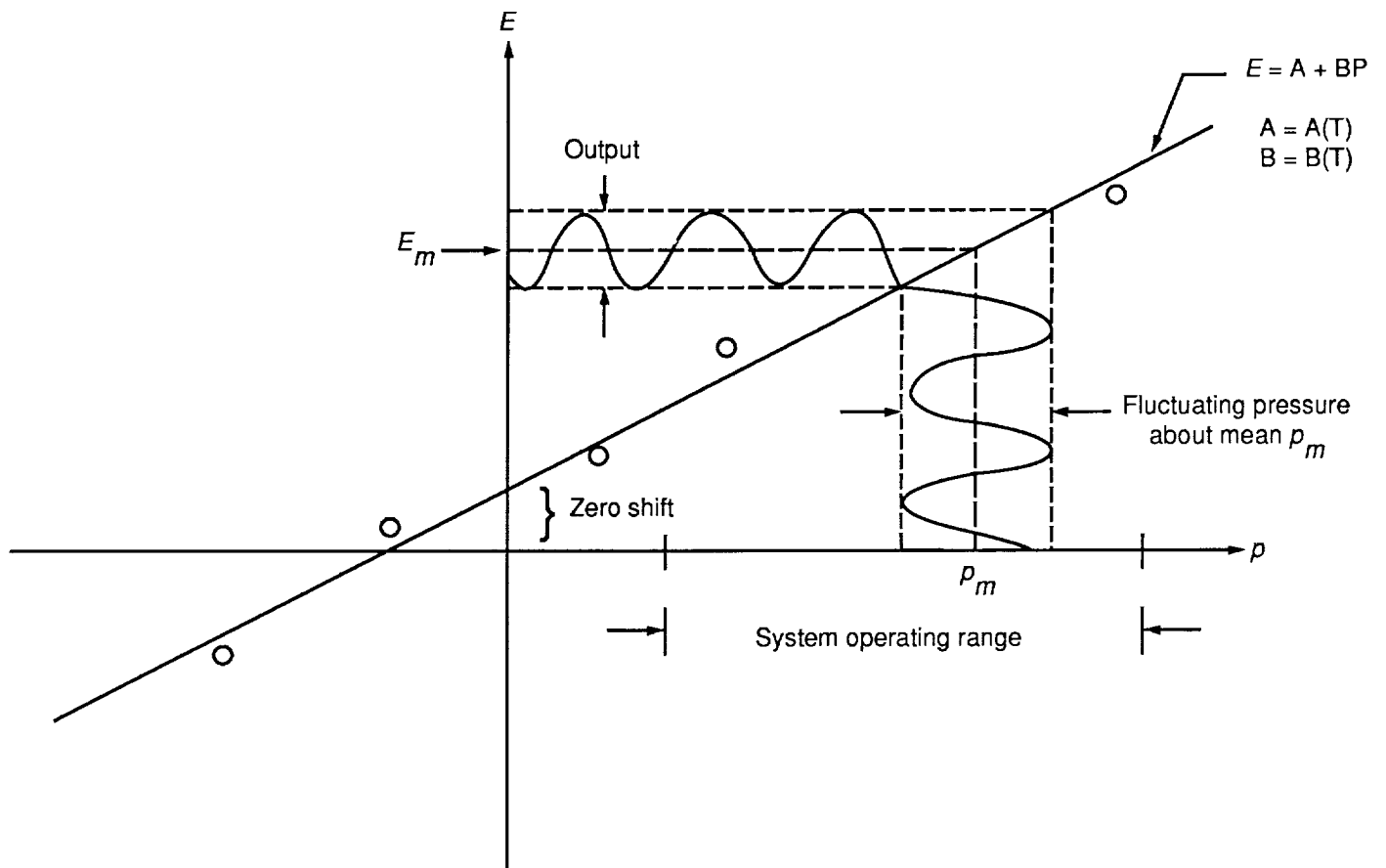


Figure A7. Transfer characteristics of piezoresistive pressure gage.

Appendix B

Gage Recession Effects

The transfer function between the fluctuating pressure at the inlet port of a recessed gage and that at the gage diaphragm is needed to correct the measured pressure spectra obtained with a recessed gage beneath a boundary layer flow. Tijdeman and Bergh (ref. 7) have developed a model for such a measurement configuration for the case when the core flow is subsonic and at low frequencies. The model is essentially a transmission line theory that accounts for the viscous dissipation in small tubes and the flow-port cavity interaction by an additional acoustic impedance. This modeling of the flow-port interaction is a greatly oversimplified description of an inherently nonlinear problem. However, Tijdeman and Bergh showed that the model was reasonably accurate for flow velocities to a Mach number of 0.8 and frequencies to 120 Hz. Richards (ref. 15) converted this theory to a more elegant matrix formulation. The intent in this appendix is to apply this transmission-line matrix formulation to recessed gage configurations and to extend the model to account for supersonic mean flow and/or high frequencies.

Generalized Configuration

Figure B1 depicts a typical recessed gage configuration for gage protection in harsh flow environments. For this configuration, the transfer function of interest is the ratio \tilde{p}_g/\tilde{p}_s . It is assumed that the fluctuating pressure and volume velocity at the port entrance are known. According to reference 7, the boundary condition at the port inlet surface is given by

$$\begin{bmatrix} \tilde{p}_s \\ \tilde{U}_s \end{bmatrix} = \begin{bmatrix} 1 & C\rho_s U_e/s \\ 0 & 1 \end{bmatrix} \begin{bmatrix} \tilde{p}_1 \\ \tilde{U}_1 \end{bmatrix} \quad (\text{B1})$$

where C is an empirical constant related to the effective port area, \tilde{p}_s and \tilde{U}_s are the fluctuating pressure and volume velocity just inside the port, and ρ_s and U_e are the static density at the port and mean flow velocity at the edge of the boundary layer over the port, respectively. The values of \tilde{p}_1 and \tilde{U}_1 are the fluctuating pressure and volume velocity just inside the port (location 1), and s is the cross-sectional area of the port. When the mean flow velocity is supersonic, Heller and Widnall (ref. 8) suggest that U_e in equation (B1) should be replaced with c , the adiabatic-phase velocity of sound.

A matrix formulation can be used to describe the relation between fluctuating pressures and volume velocities at one end of a constant-area tube element and those at the other end as follows:

$$\begin{pmatrix} \tilde{p}_{i+1} \\ \tilde{U}_{i+1} \end{pmatrix} = \begin{bmatrix} \cosh(\phi_{i,i+1} l_{i,i+1}) & Z_{c,(i,i+1)} \sinh(\phi_{i,i+1} l_{i,i+1}) \\ \frac{1}{Z_{c,(i,i+1)}} \sinh(\phi_{i,i+1} l_{i,i+1}) & \cosh(\phi_{i,i+1} l_{i,i+1}) \end{bmatrix} \begin{pmatrix} \tilde{p}_i \\ \tilde{U}_i \end{pmatrix} \quad (\text{B2})$$

for $i = 1, 3, \text{ and } 5$. In this formulation, $\phi_{i,i+1}$ and $l_{i,i+1}$ are the complex propagation constant and length of element $(i, i+1)$. $Z_{c,(i,i+1)}$ is the tube characteristic acoustic impedance that depends on the element geometry.

Thus, if the boundary conditions are known at the junction between the three constant-area elements and at the face of the gage, the desired transfer function (\tilde{p}_g/\tilde{p}_s) can be determined. These boundary conditions are as follows: at the junction between the three elements, the pressure is constant and the volume velocity is continuous; for example,

$$\tilde{p}_2 = \tilde{p}_3 = \tilde{p}_5 \quad (\text{B3})$$

$$\tilde{U}_2 - \tilde{U}_3 - \tilde{U}_5 = 0 \quad (\text{B4})$$

The relation

$$\frac{\tilde{U}_6}{\tilde{p}_6} = \left[j \left(\frac{\omega}{c} \right) \left(\frac{\gamma V}{\rho_6 c} \right) \left(\sigma + \frac{1}{k} \right) \right] \quad (\text{B5})$$

given in reference 15 is used to describe the conditions at gage location 6. In this equation, $j = \sqrt{-1}$, ω is the angular frequency, γ is the ratio of specific heats, V is the volume of the cavity at the face of the gage, σ is a

diaphragm deflection factor, and k is the polytropic constant ($k = 1$ for isothermal process, $k = \gamma$ for adiabatic process). Finally, because the cavity dimensions at the face of the gage are assumed to be very small relative to the shortest wavelength of interest, \bar{p}_g is assumed equivalent to \bar{p}_6 .

Recessed Gage Configuration

Utilization of this transmission-line matrix formulation technique is convenient for modeling various high-frequency recessed pressure gage configurations in supersonic flow. The particular gage recess geometry in this study is depicted in figure B2. For this configuration, the derivation above can be simplified to a combination of equations (B1) and (B2) and a boundary condition similar to that in equation (B5).

Figure B3 depicts a comparison of measured data and model prediction (taken from ref. 8) for $M = 0$, $M = 0.8$, and low frequencies (to 120 Hz). As seen in the figure, the model performs quite well for those conditions. For the present test, however, it is important to understand the effects of sound and/or grazing flow over a recessed cavity at supersonic flow rates (to $M = 3.5$) and higher frequencies (to 5 kHz).

A preliminary test was conducted to determine the effects of sound over a recessed cavity (no flow) for frequencies to 30 kHz. A recessed gage, with a recession length of 1.25 in. and a diameter of 0.16 in., was placed opposite a flush-mounted reference microphone in a small, rectangular waveguide (0.2-in. by 0.4-in.), in which only plane waves propagate over the frequency range of interest. The results from this test are shown in figure B4, where the solid curve represents the actual measured transfer function (ratio of acoustic pressure at the recessed gage to that measured by the flush-mounted high-quality condenser microphone) and the dashed curve represents the predicted transfer function. As can be seen in the figure, the model matches the measured levels at the three resonances. The frequencies where resonances occur are not quite as well matched but are remarkably close, given the sensitivity of the calculations. The model predicts the resonant frequencies much better than does the standard organ pipe calculation, which predicts that the resonances should occur at about 5, 15, and 25 kHz. Clearly, this transmission-line matrix formulation represents a useful model to account for various physical phenomena within the recessed gage cavity for higher frequencies (at least to 30 kHz).

Present Configuration

Transfer function results are provided in figure B5 for a typical recessed gage configuration in the present test. The aeroacoustic parameters in the transfer function calculations are included in the inset table. The maximum frequency for the present test was 5 kHz, so the transfer functions are displayed only for that frequency range. In this figure, the solid curve represents a transfer function expected with no mean flow. The dashed curve depicts the transfer function computed for the supersonic flow condition.

Note that the no-flow curve contains a resonance of 27 dB at approximately 2 kHz, whereas the supersonic flow curve indicates a peak resonance of less than 1 dB near 1.8 kHz. Because the transfer function for the supersonic flow case is so flat, this correction (recall that this transfer function typically should be used to correct the measured response to attain the true response) was not implemented in view of other greater experimental uncertainties. This situation held true for all port lengths in the experiment.

Some measured spectra indicate peaks that fall near these predicted resonances. These measured peaks are often more than 1 dB above the surrounding levels, as predicted by the transmission line model (with all of the aeroacoustic parameters included), but are much less than 27 dB above the surrounding levels. However, no consistent trend appears for the resonant peaks in the measured spectra. Thus, this model may properly describe the effects of the recessed cavity, even for these harsh conditions. Theoretical and experimental studies are being conducted to improve the model for supersonic flow rates.

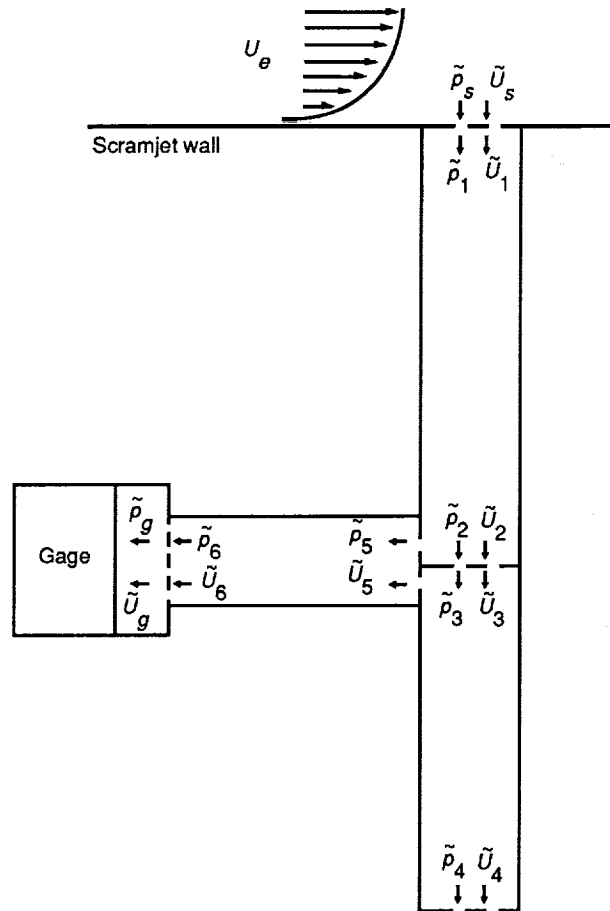


Figure B1. Generalized configuration.

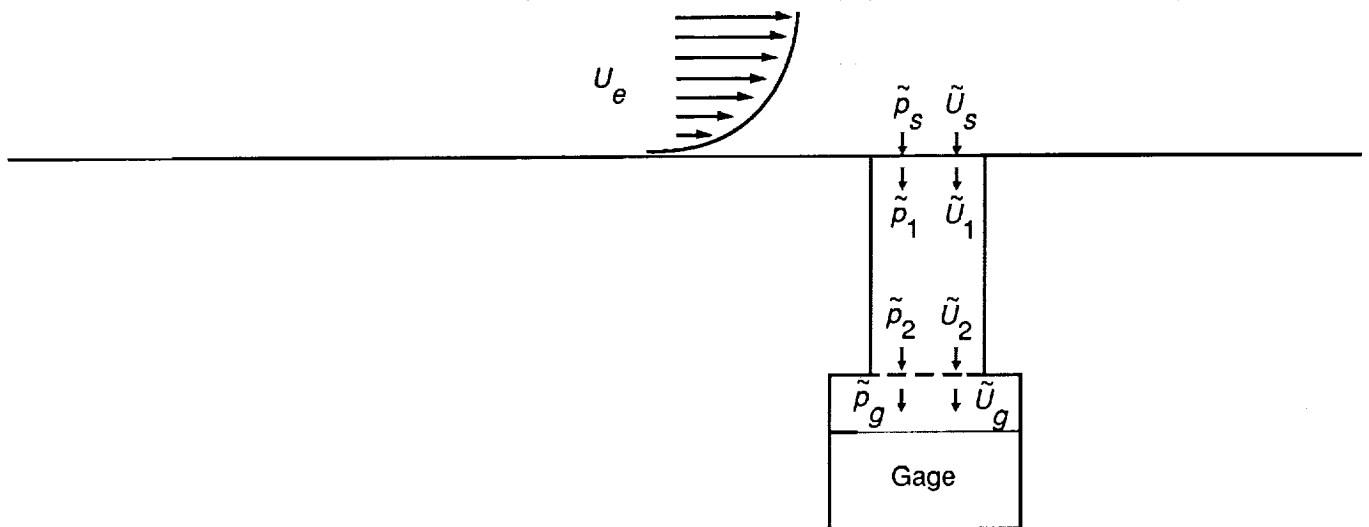


Figure B2. Recessed gage configuration.

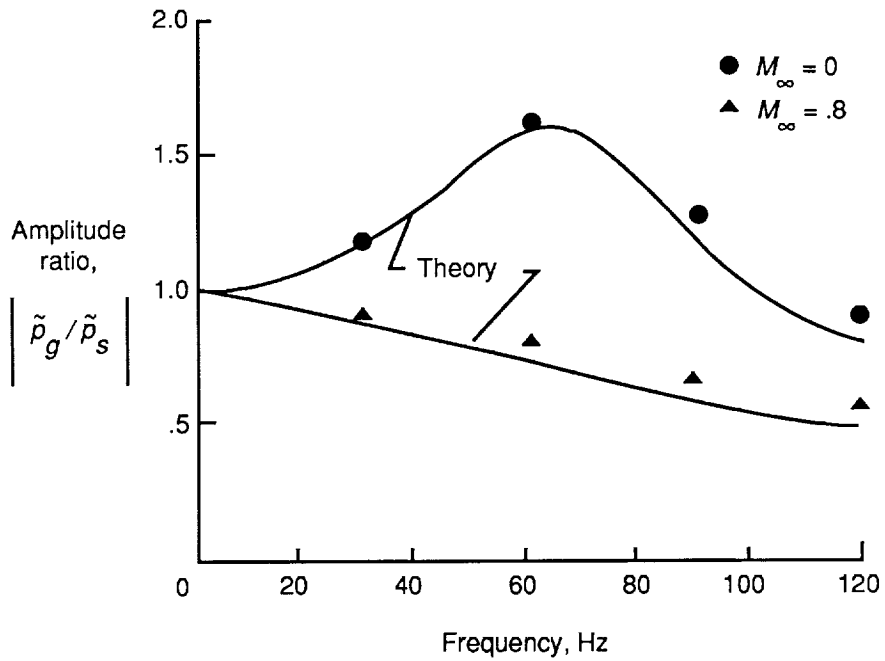


Figure B3. Frequency response change of recessed gage from grazing flow (ref. 7).

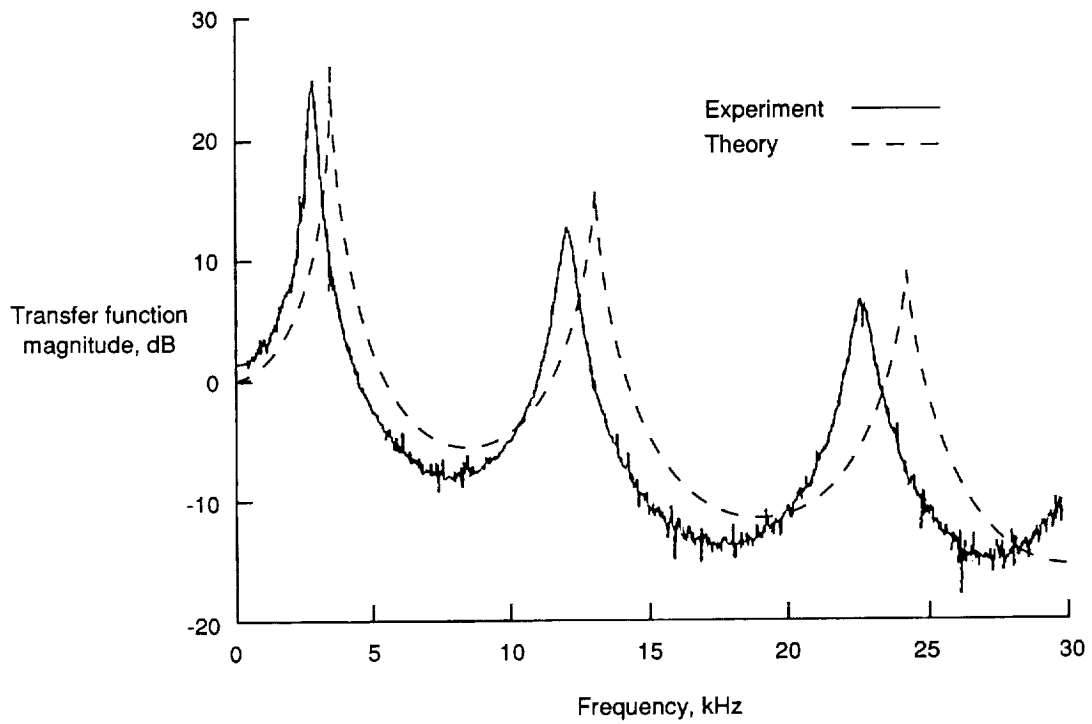


Figure B4. Measured versus predicted transfer function magnitudes and resonant frequencies.

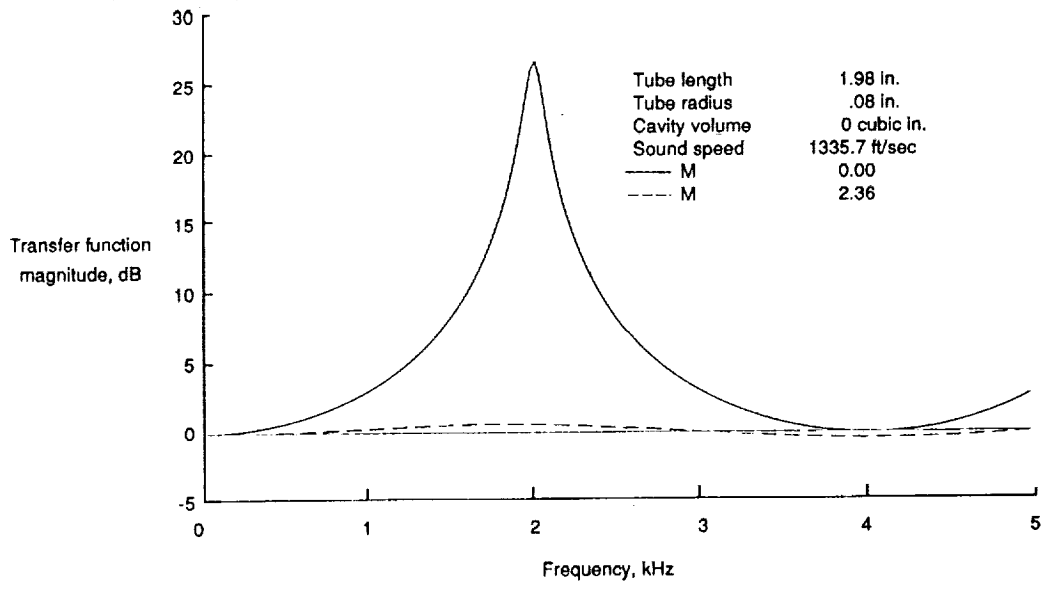


Figure B5. Computed transfer function magnitudes versus frequencies for $M = 0.00$ and $M = 2.36$.

Appendix C

Recessed Gage Self-Noise Effects

In this appendix, the self-noise or aeroacoustic disturbance generated by the interaction of the boundary layer with the gas in the recess port is addressed. Such interactions, if present, distort and contaminate the aeroacoustic loads in the absence of the recess port. The frequencies at which such effects may occur are estimated from results for subsonic flows over relatively shallow cavities. Reference 16 gives a survey of the work in this area.

According to reference 16, flow-cavity interactions are classified into three categories: fluid dynamic, fluid resonant, and fluid elastic. Of these, the fluid-resonant interaction should be the dominant interaction mode for the recessed gage configurations in this investigation. (Recess diameter and length in this discussion are referred to as cavity length and depth, respectively, in the context of refs. 16 and 17. Also, the cavities of these references were generally rectangular.) Formulas quoted from reference 17 have been changed for consistency with the notation of this discussion, l is the recess (or tube) length, and d is the recess (or tube) diameter. For the recessed gages along the isolator section of the GHSE, the d/l is about 0.08.

Figure C1 shows a collection of data replicated from reference 17 for the first three crosswise modes (i.e., modes associated with the diameter d) for cavity d/l ratios ranging from 16 to 0.25. The data are plotted as Strouhal number fd/U_e versus Mach number M for three different mode numbers n . Although most of the data are for subsonic flows, a small amount extends to a Mach number of 1.1 for modes 1 and 2. The data are fairly well described by an empirical equation attributed to Rossiter and given in reference 17 as

$$\frac{fd}{U_e} = \frac{n - \alpha}{(1/K_v) + M} \quad (\text{C1})$$

The empirical constants K_v and α are taken to be 0.57 and 0.25, respectively, for the first three modes. Note that the parameter d/l does not explicitly appear in this equation. Reference 17 indicates that α decreases as d/l decreases. The value K_v is the ratio of vortex convection velocity across the recess port to the free-stream velocity. If this equation is used to calculate a Strouhal number for the flow conditions over a typical recessed gage of interest in the isolator section (i.e., $M \approx 1.6$ and $d/l \approx 0.08$), then for a first-mode excitation, the result is 0.22. This value appears to agree reasonably well with the extrapolation of the bottom curve in figure C1 to a Mach number of 1.6. This value for the Strouhal number gives a crosswise modal frequency of about 43 kHz, which will be higher if a lower value of α is used. This frequency is well out of our range of interest and is not a problem in this investigation.

Flow excitation of depthwise modes in shallow cavities underneath subsonic flows is also discussed in reference 17; however, extrapolation to the configuration of interest in this investigation is far less reliable than is the case for the crosswise modes discussed above. In the context of the present investigation, these depthwise modes can be identified with the longitudinal acoustic or organ pipe modes that control the resonant response of the gage-cavity system to incident acoustic pressure disturbances discussed in appendix B. In addition to purely acoustic pressures, a possibility clearly exists for the unsteady part of the flow to excite these modes and to result in additional distortion of the desired fluctuating pressure measurements. However, as suggested in appendix B, localized mean flow interaction with the ported tube dampens the resonant response to negligible levels. Therefore, flow-port interaction noise is essentially uniformly distributed across the entire frequency spectrum; consequently, it just raises the effective noise floor of the measurement system. This flow-port interaction or self-noise is assumed present at about equal levels at all gage locations and is treated as the key contributor to the total noise floor of the measurement system.

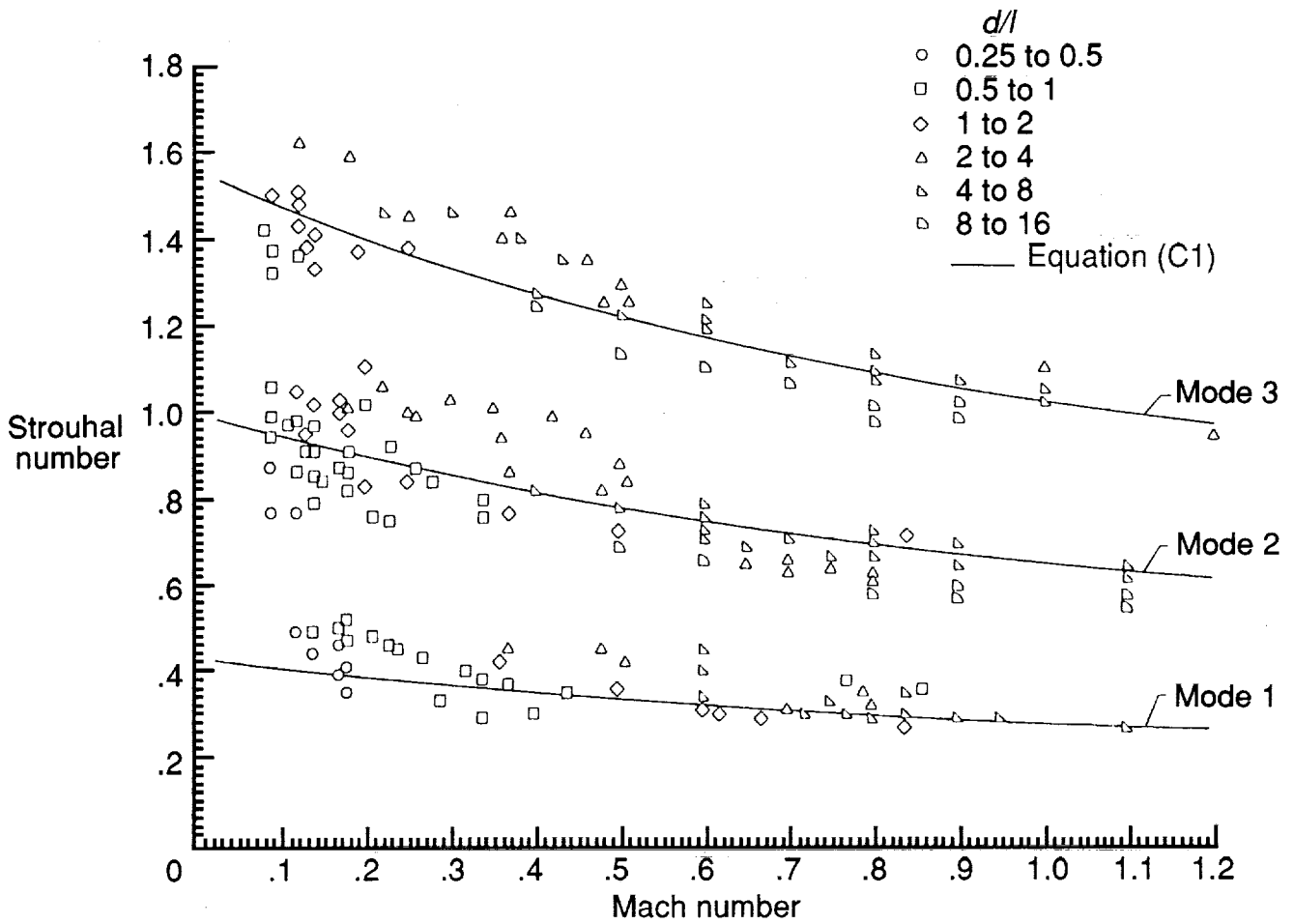


Figure C1. Experimental results from several investigations of cavity oscillation frequencies versus prediction of equation (C1) (ref. 17).

References

1. Holden, Michael S.: A Review of Aerothermal Problems Associated With Hypersonic Flight. AIAA-86-0267, Jan. 1986.
2. Andrews, Earl H., Jr.; Torrence, Marvin G.; Anderson, Griffin Y.; Northam, G. Burton; and Mackley, Ernest A.: *Langley Mach 4 Scramjet Test Facility*. NASA TM-86277, 1985.
3. Bement, D. A.; Stevens, J. R.; Thompson, M. W.; Andrews, E. H.; and Eggers, J. M.: Measured Performance of the Generic High-Speed Engine. *Seventh National Aero-Space Plane Technology Symposium, Volume V—Propulsion*, NASP CP-7044, Part 1, 1989, pp. 313-342.
4. Jones, Michael G.: *An Operations Manual for the Digital Data System*. NASA CR-181688, 1988.
5. Parrott, Tony L.; Jones, Michael G.; and Albertson, Cindy W.: *Fluctuating Pressures Measured Beneath a High-Temperature, Turbulent Boundary Layer on a Flat Plate at a Mach Number of 5*. NASA TP-2947, 1989.
6. Hardin, Jay C.: *Introduction to Time Series Analysis*. NASA RP-1145, 1986.
7. Tjeldeman, H.; and Bergh, H.: *The Influence of the Main Flow on the Transfer Function of Tube-Transducer Systems Used for Unsteady Pressure Measurements*. NLR MP 72023 U, National Aerospace Lab. (NLR) (Netherlands), Sept. 1972.
8. Heller, Hanno H.; and Widnall, Sheila E.: Dynamics of an Acoustic Probe for Measuring Pressure Fluctuations on a Hypersonic Re-Entry Vehicle. *J. Acoust. Soc. America*, vol. 44, no. 4, Oct. 1968, pp. 885-896.
9. Blake, William K.: *Aero-Hydroacoustics for Ships, Volume II*. Rep. No. DTNSRDC-84/010, U.S. Navy, June 1984.
10. Shapiro, Ascher H.: *The Dynamics and Thermodynamics of Compressible Fluid Flow, Volume I*. Ronald Press Co., c.1953.
11. Laganelli, A. L.; Martellucci, A.; and Shaw, L. L.: Wall Pressure Fluctuations in Attached Boundary-Layer Flow. *AIAA J.*, vol. 21, no. 4, Apr. 1983, pp. 495-502.
12. Speaker, W. V.; and Ailman, C. M.: *Spectra and Space-Time Correlations of the Fluctuating Pressures at a Wall Beneath a Supersonic Turbulent Boundary Layer Perturbed by Steps and Shock Waves*. NASA CR-486, 1966.
13. Raman, K. R.: *Surface Pressure Fluctuations in Hypersonic Turbulent Boundary Layers*. NASA CR-2386, 1974.
14. Salikuddin, M.; Burrin, R. H.; and Brown, W. H.: Design and Characterization of a High Temperature and High Frequency Infinite-Line Pressure Probe. AIAA-89-1116, Apr. 1989.
15. Richards, W. Bruce: *Propagation of Sound Waves in Tubes of Noncircular Cross Section*. NASA TP-2601, 1986.
16. Komerath, N. M.; Ahuja, K. K.; and Chambers, F. W.: Prediction and Measurement of Flows Over Cavities—A Survey. AIAA-87-0166, Jan. 1987.
17. Block, Patricia J. W.: *Noise Response of Cavities of Varying Dimensions at Subsonic Speeds*. NASA TN D-8351, 1976.

Table I. Data for Recessed Gage Transfer Function Calculation

(a) Run 6, batch 7 (R6B7)

Gage	Model	Gage		Analysis segment		
	Port/ESP	Location, in.	Recession, in.	Region	ESP, cycles	Interval, sec
1	TN/NOZ18 ^a	-2.2	0.78	I	6-8	3.7-5.5
1	TN/NOZ18 ^a	-2.2	.78	II	15-18	10.0-12.3
4	306/51	35.0	1.97	I	6-8	3.7-5.5
4	306/51	35.0	1.97	II	15-18	10.0-12.3
Gage	p_t , psia	T_t , °R	p_e , psia	T_e , °R	ρ_e , slugs/ft ³	ρ_{cav} , slugs/ft ³
1	94.14	1532.4	1.35	455.7	248.6×10^{-6}	188.8×10^{-6}
1	92.38	1580.2	1.29	466.3	232.1	180.4
4	94.14	1532.4	7.07	731.3	810.9	988.3
4	92.38	1580.2	7.49	770.8	815.4	1047.6
Gage	c_e , ft/sec	U_e , ft/sec	q_e , psia	p_{rms} , psia	p_{rms}/p_e , percent	p_{rms}/q_e , percent
1	1046.3	3596.3	11.2	0.0152	1.13	0.14
1	1058.5	3657.8	10.9	.0165	1.28	.15
4	1325.4	3102.1	27.1	.1311	1.86	.48
4	1360.8	3118.0	27.5	.2150	2.87	.78
Gage	M_e	N_{Re} , ft ⁻¹	(OASPL) _{PSD} , dB	OASPL, dB	OASPL - (OASPL) _{PSD} , dB	
1	3.4	2.65×10^6	134.4	135.2	0.8	
1	3.5	2.47	135.1	139.0	3.9	
4	2.3	5.22	153.1	153.2	.1	
4	2.3	5.08	157.4	157.8	.4	

^aNOZ18 refers to port 18 in tunnel wall.

Table I. Continued

(b) Run 15, batch 6 (R15B6)

Gage	Model	Gage		Analysis segment		
	Port/ESP	Location, in.	Recession, in.	Region	ESP, cycles	Interval, sec
4	306/51	35.0	1.97	I	5-8	3.1-5.2
4	306/51	35.0	1.97	II	14-20	9.4-13.4
4	306/51	35.0	1.97	III	24-36	16.3-24.4
5	308/81	47.7	1.85	I	5-8	3.1-5.2
5	308/81	47.7	1.85	II	14-20	9.4-13.4
5	308/81	47.7	1.85	III	24-36	16.3-24.4
6	309/101	53.4	1.75	II	14-20	9.4-13.4
6	309/101	53.4	1.75	III	24-36	16.3-24.4
Gage	p_t , psia	T_t , °R	p_e , psia	T_e , °R	ρ_e , slugs/ft ³	ρ_{cav} , slugs/ft ³
4	91.81	1468.9	6.66	694.0	805.0×10^{-6}	931.1×10^{-6}
4	91.92	1502.4	6.76	712.7	795.9	945.5
4	91.31	1540.5	20.95	1011.6	1737.9	2930.1
5	91.81	1468.9	7.52	718.6	878.1	1051.7
5	91.92	1502.4	18.28	947.0	1619.7	2556.4
5	91.31	1540.5	21.82	1023.4	1788.9	3051.3
6	91.92	1502.4	16.89	925.9	1531.0	2362.6
6	91.31	1540.5	18.33	973.7	1579.6	2563.4
Gage	c_e , ft/sec	U_e , ft/sec	q_e , psia	p_{rms} , psia	p_{rms}/p_e , percent	p_{rms}/q_e , percent
4	1291.3	3050.8	26.0	0.1357	2.04	0.52
4	1308.5	3079.8	26.2	.1650	2.44	.63
4	1558.9	2520.6	38.3	2.1752	10.38	5.67
5	1313.9	3002.0	27.5	.2007	2.67	.73
5	1508.3	2582.8	37.5	.5278	2.89	1.41
5	1568.0	2492.4	38.6	.6879	3.15	1.78
6	1491.5	2631.4	36.8	2.8674	16.97	7.79
6	1529.4	2609.4	37.3	2.3850	13.01	6.39
Gage	M_e	N_{Re} , ft ⁻¹	(OASPL) _{PSD} , dB	OASPL, dB	OASPL - (OASPL) _{PSD} , dB	
4	2.4	5.29×10^6	153.4	153.5	0.1	
4	2.3	5.18	155.1	153.1	-2.0	
4	1.6	7.27	177.5	177.6	.1	
5	2.3	5.54	156.8	157.6	.8	
5	1.7	7.26	165.2	168.4	3.2	
5	1.6	7.34	167.5	169.8	2.3	
6	1.8	7.09	179.9	180.3	.4	
6	1.7	7.02	178.3	178.4	.1	

Table I. Continued

(c) Run 50, batch 10 (R50B10)

Gage	Model	Gage		Analysis segment		
	Port/ESP	Location, in.	Recession, in.	Region	ESP, cycles	Interval, sec
2	301/7	8.5	(a)	I	4-6	3.1-5.0
2	301/7	8.5	(a)	II	17-19	14.2-16.0
2	301/7	8.5	(a)	III	22-24	18.3-20.2
3	304/26	24.2	1.97	I	4-6	3.1-5.0
3	304/26	24.2	1.97	II	17-19	14.2-16.0
3	304/26	24.2	1.97	III	22-24	18.3-20.2
4	306/51	35.0	1.97	I	4-6	3.1-5.0
4	306/51	35.0	1.97	II	17-19	14.2-16.0
4	306/51	35.0	1.97	III	22-24	18.3-20.2
5	308/81	47.7	1.85	I	4-6	3.1-5.0
5	308/81	47.7	1.85	II	17-19	14.2-16.0
5	308/81	47.7	1.85	III	22-24	18.3-20.2
6	309/101	53.4	1.75	III	22-24	18.3-20.2
Gage	p_t , psia	T_t , °R	p_e , psia	T_e , °R	ρ_e , slugs/ft ³	ρ_{cav} , slugs/ft ³
2	94.51	1475.7	3.62	581.0	522.8×10^{-6}	506.3×10^{-6}
2	90.65	1575.0	3.53	623.1	475.4	493.7
2	91.17	1581.7	3.55	625.7	476.1	496.5
3	94.51	1475.7	6.74	694.0	815.0	942.7
3	90.65	1575.0	6.43	739.5	729.6	899.3
3	91.17	1581.7	6.46	742.5	730.5	904.0
4	94.51	1475.7	7.07	703.6	843.6	989.3
4	90.65	1575.0	7.44	770.9	809.5	1040.1
4	91.17	1581.7	14.41	933.7	1295.1	2015.4
5	94.51	1475.7	14.67	866.6	1420.5	2051.7
5	90.65	1575.0	14.61	934.9	1311.3	2043.4
5	91.17	1581.7	14.60	937.2	1307.3	2042.0
6	91.17	1581.7	21.80	1050.9	1740.6	3048.5

^aInfinite line.

Table I. Concluded

(c) Concluded

Gage	c_e , ft/sec	U_e , ft/sec	q_e , psia	p_{rms} , psia	p_{rms}/p_e , percent	p_{rms}/q_e , percent
2	1181.5	3278.2	19.5	0.0115	0.32	0.06
2	1223.5	3381.5	18.9	.0105	.30	.06
2	1226.0	3388.7	19.0	.0109	.31	.06
3	1291.2	3064.4	26.6	.0665	.99	.25
3	1332.9	3167.9	25.4	.0781	1.21	.31
3	1335.6	3174.9	25.6	.1341	2.07	.52
4	1300.1	3045.4	27.2	.1708	2.41	.63
4	1360.9	3107.9	27.1	.3369	4.53	1.24
4	1497.7	2789.9	35.0	.9279	6.44	2.65
5	1442.9	2704.8	36.1	.2007	1.37	.56
5	1498.7	2772.8	35.0	.1388	.95	.40
5	1500.5	2782.4	35.1	1.0902	7.47	3.10
6	1588.9	2525.1	38.5	.6273	2.88	1.63
Gage	M_e	N_{Re} , ft ⁻¹	(OASPL) _{PSD} , dB	OASPL, dB	OASPL - (OASPL) _{PSD} , dB	
2	2.8	4.21×10^6	132.0	133.0	1.0	
2	2.8	3.75	131.2	134.1	1.9	
2	2.8	3.75	131.5	134.2	2.7	
3	2.4	5.38	147.2	151.9	4.7	
3	2.4	4.76	148.6	153.1	4.5	
3	2.4	4.76	153.3	156.4	3.1	
4	2.3	5.48	155.4	157.4	2.0	
4	2.3	5.03	161.3	163.3	2.0	
4	1.9	6.33	170.1	177.4	7.3	
5	1.9	7.08	156.8	158.2	1.4	
5	1.8	6.36	153.6	160.2	6.6	
5	1.8	6.35	171.5	181.0	9.5	
6	1.6	7.11	166.7	178.7	12.0	

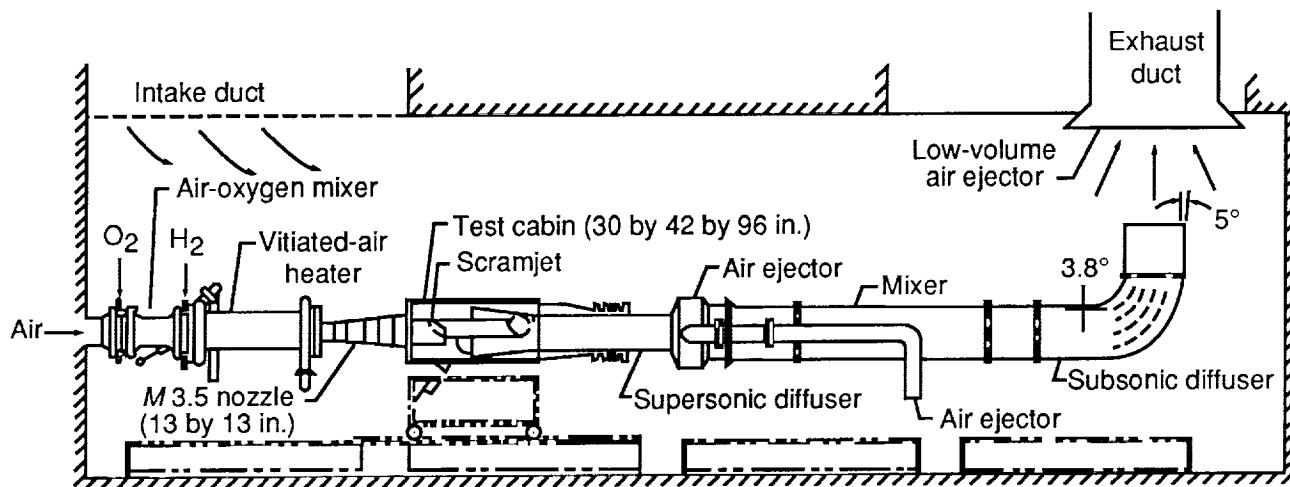


Figure 1. Combustion-Heated Scramjet Test Facility at the Langley Research Center.

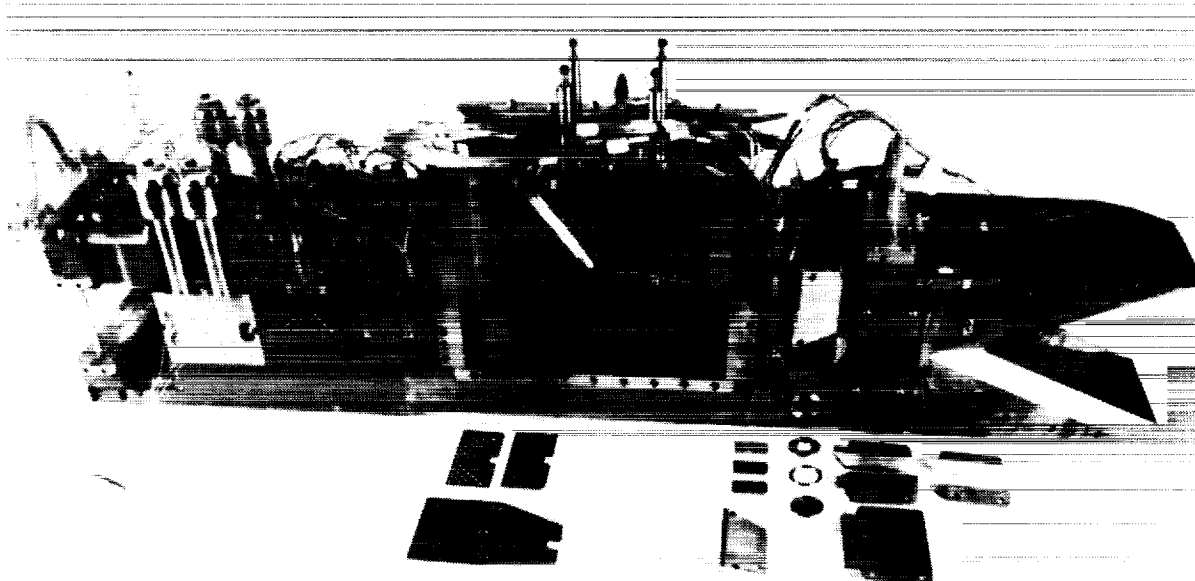
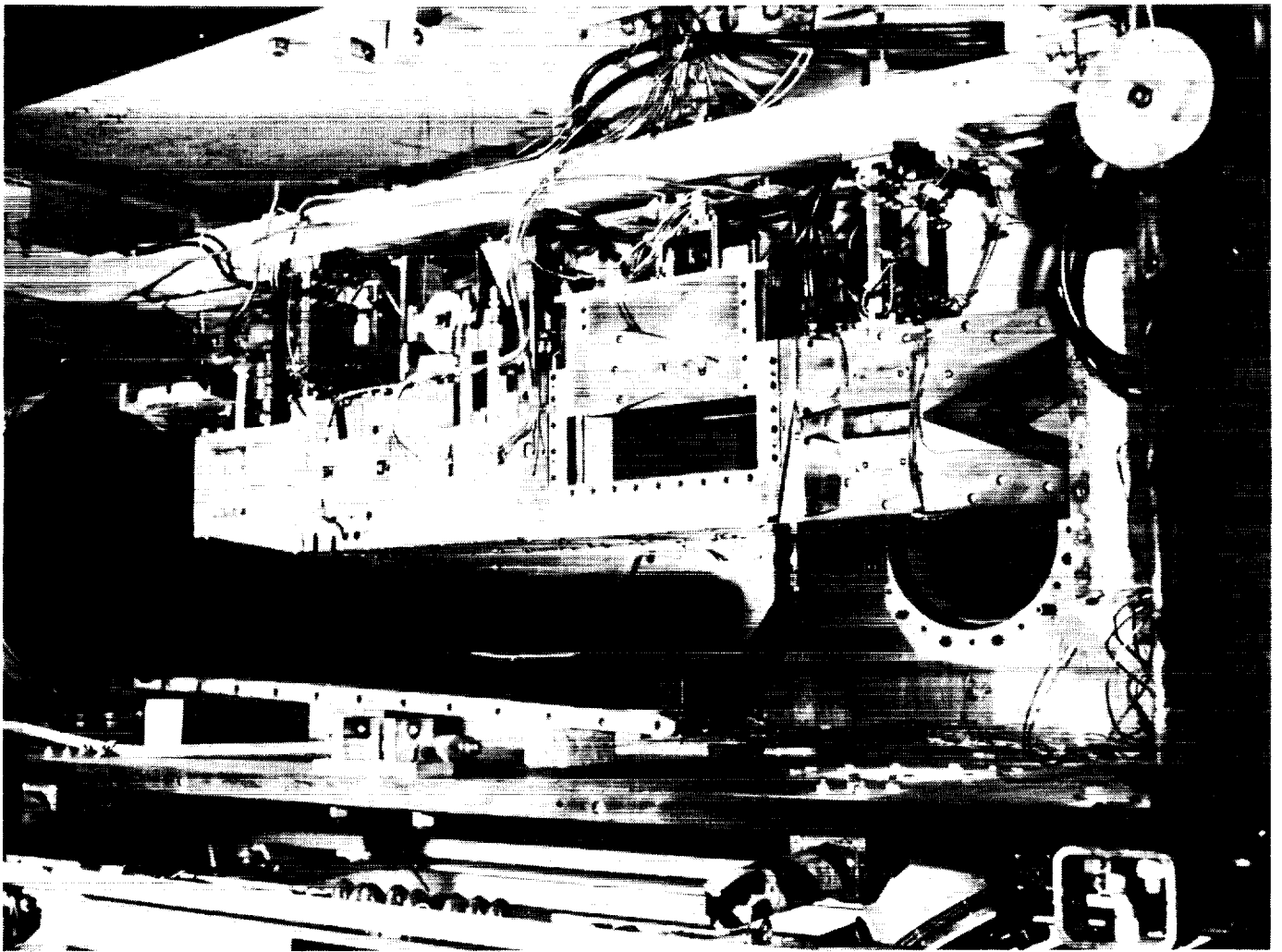


Figure 2. GHSE model.

L-88-9905

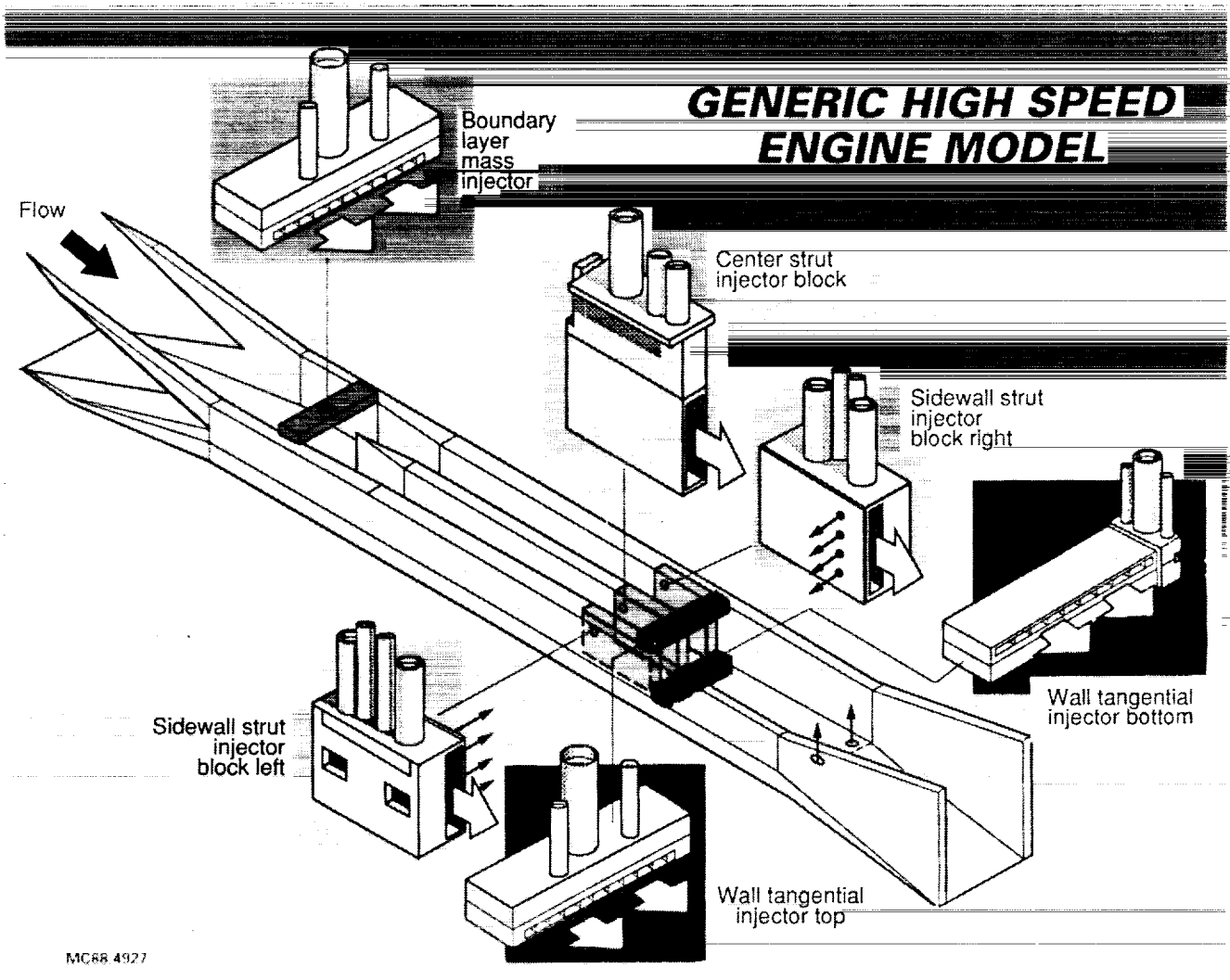
ORIGINAL PAGE
BLACK AND WHITE PHOTOGRAPH

ORIGINAL PAGE
BLACK AND WHITE PHOTOGRAPH



L-88-10,681

Figure 3. GHSE model installed in Combustion-Heated Scramjet Test Facility.



MC68 4927

L-89-3606

Figure 4. Conceptual view of GHSE model.

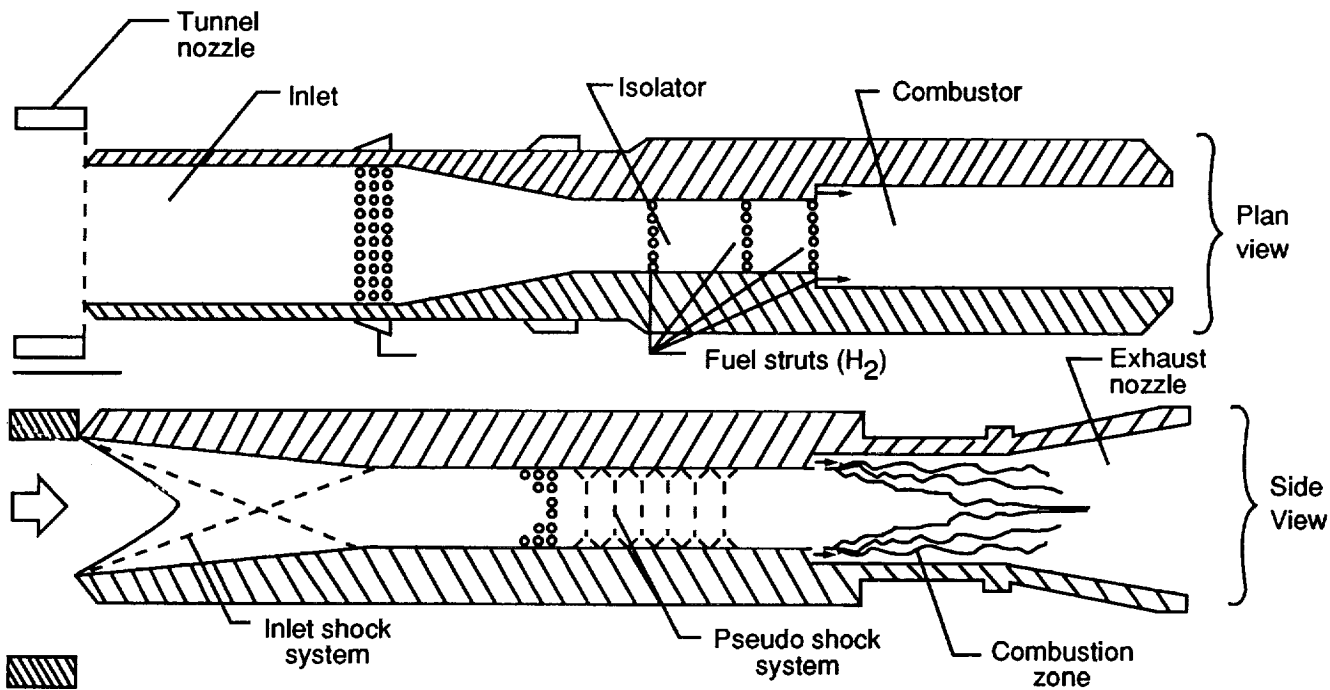


Figure 5. Plan view and side view of GHSE model. (Figure not to scale.)

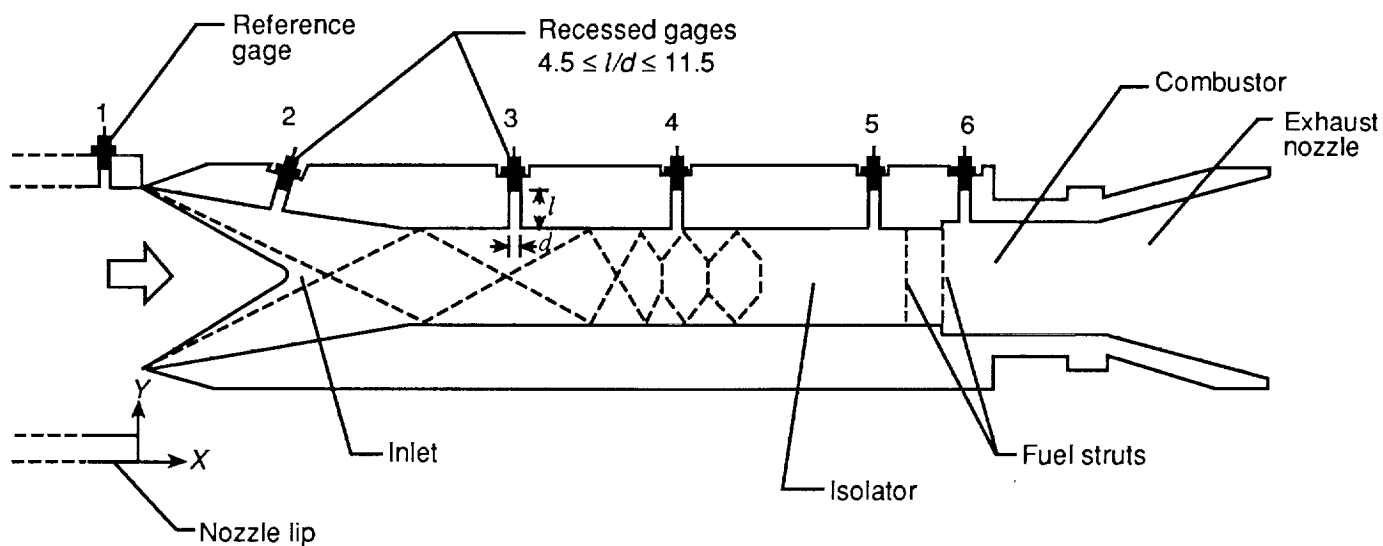


Figure 6. Side view of engine model and gage installation layout. (Figure not to scale.)

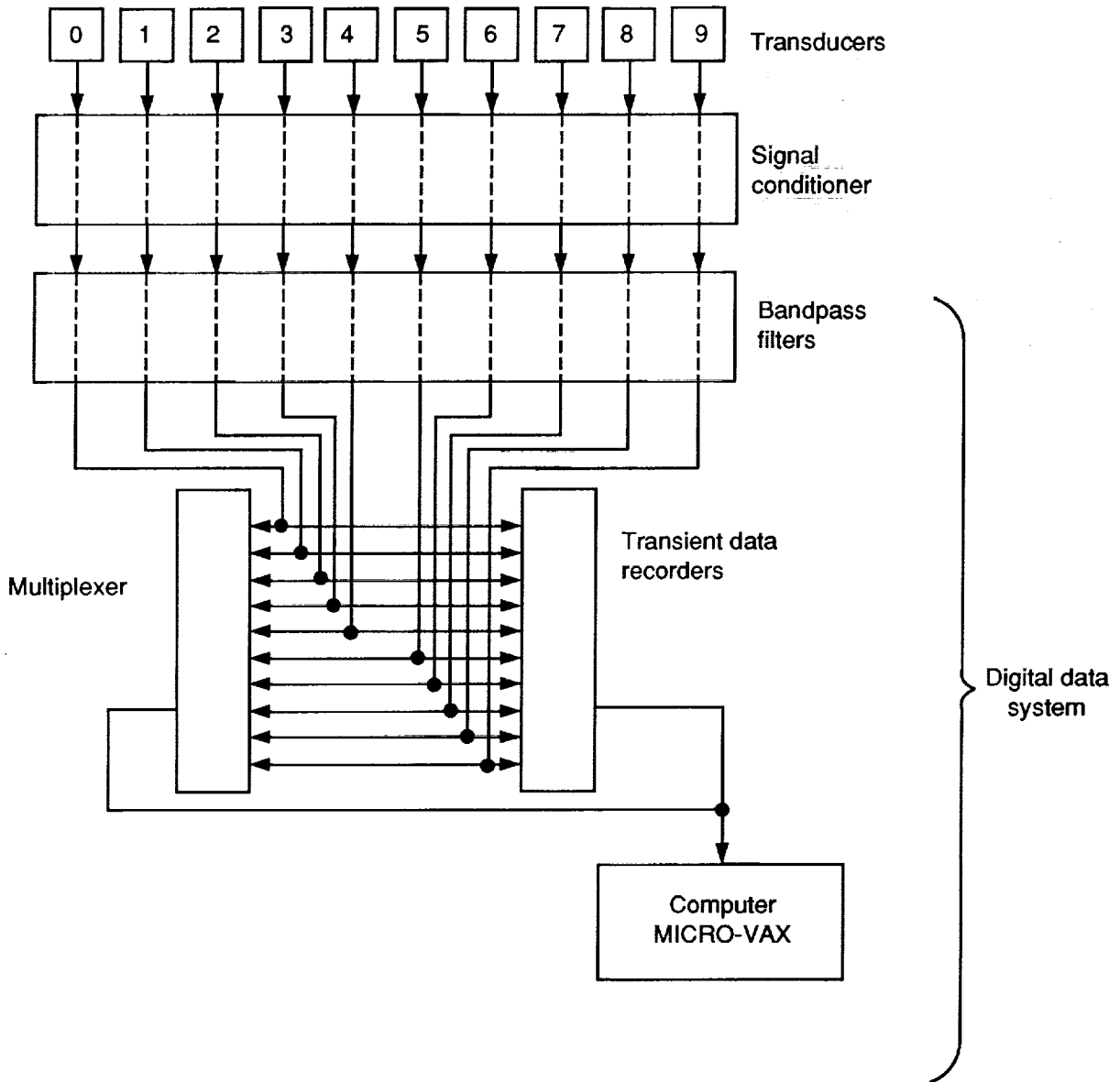


Figure 7. Digital Data Acquisition System.

Series	Time, sec	Cycle	ϕ
1	10.2	15	0.415
2	10.9	16	.407
3	12.2	18	.407
4	13.0	19	.492 ^a
5	14.3	21	.581

^a Acquired during transition to unstart.

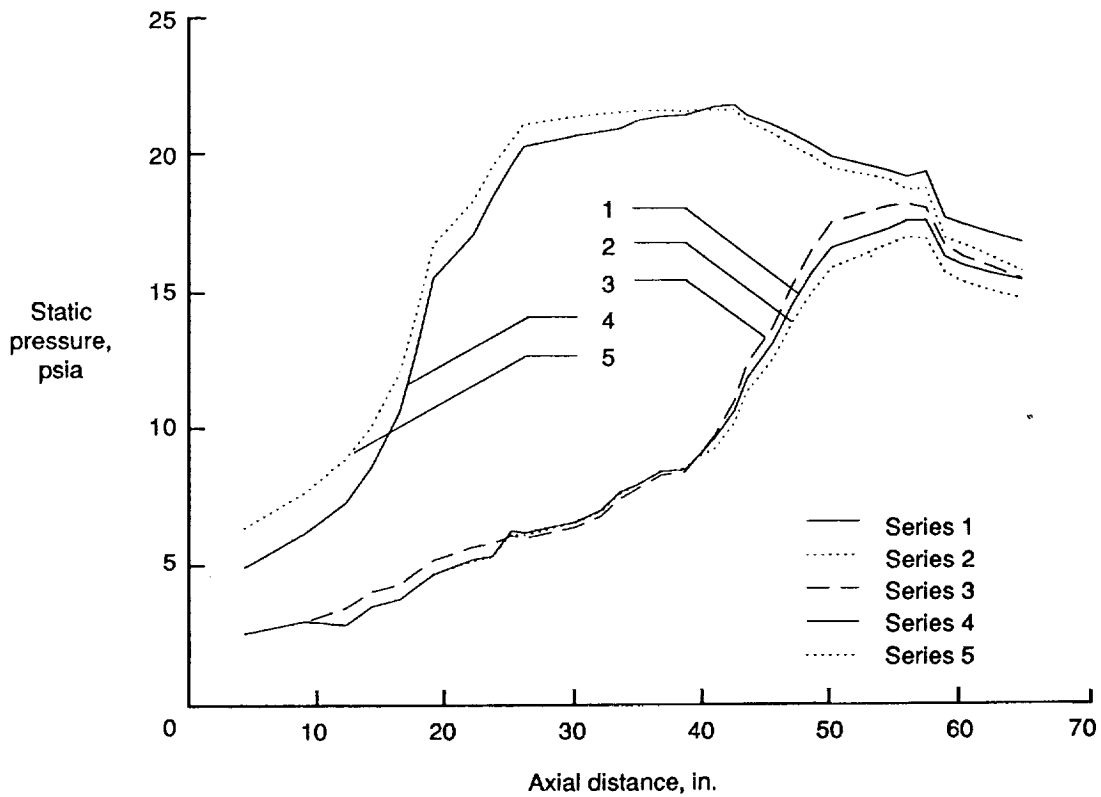


Figure 8. Axial static pressure distribution versus time for test R6B7.

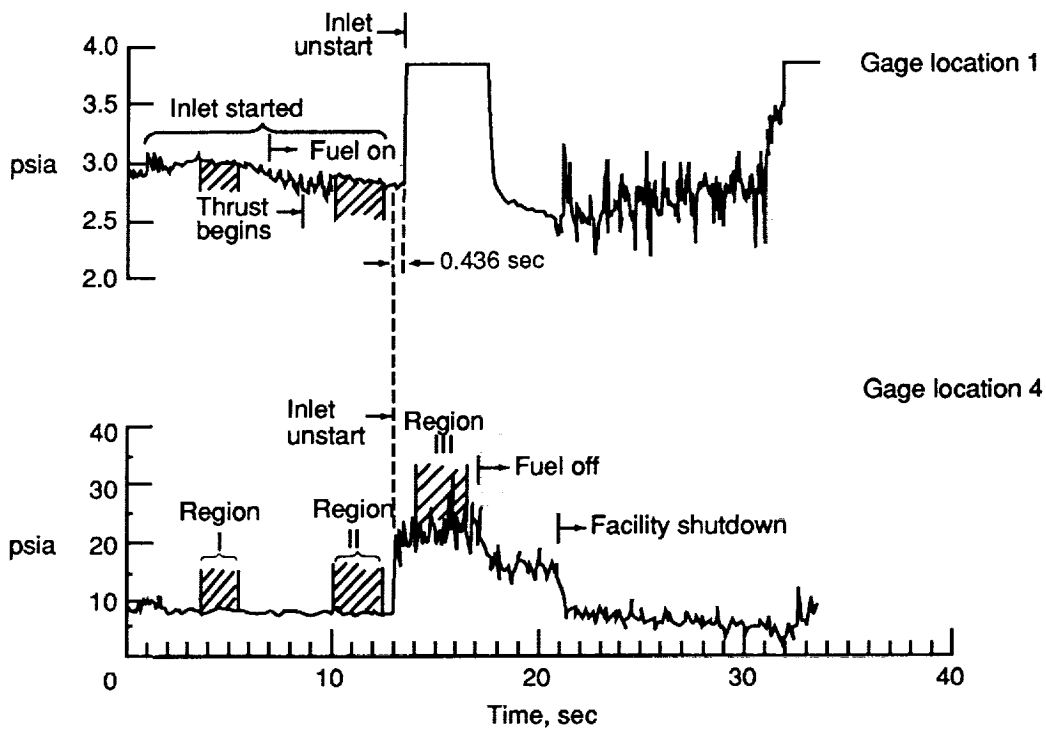


Figure 9. Pressure time histories during unstart for test R6B7.

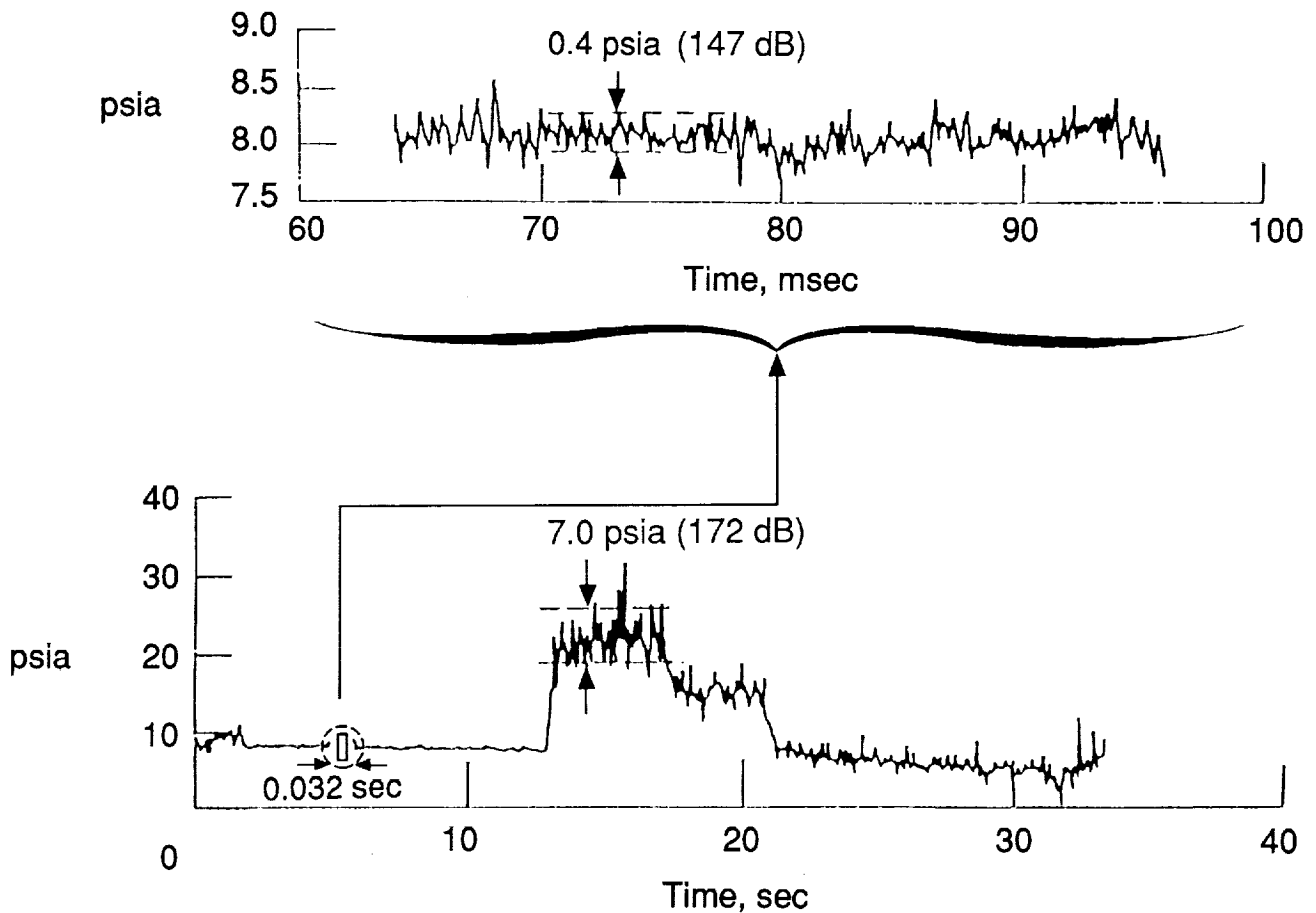
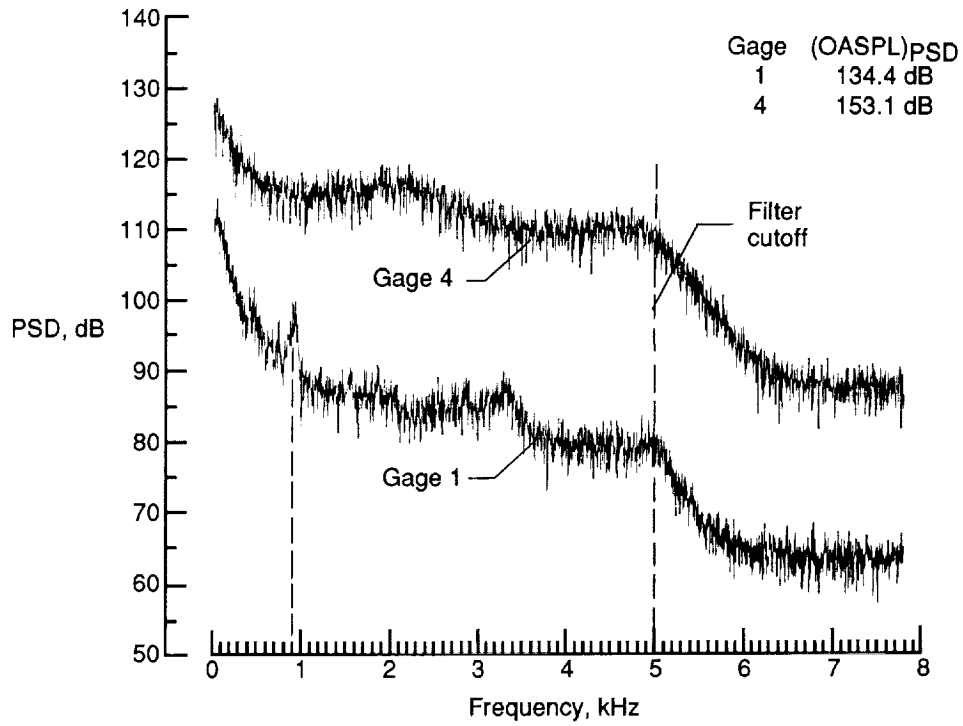
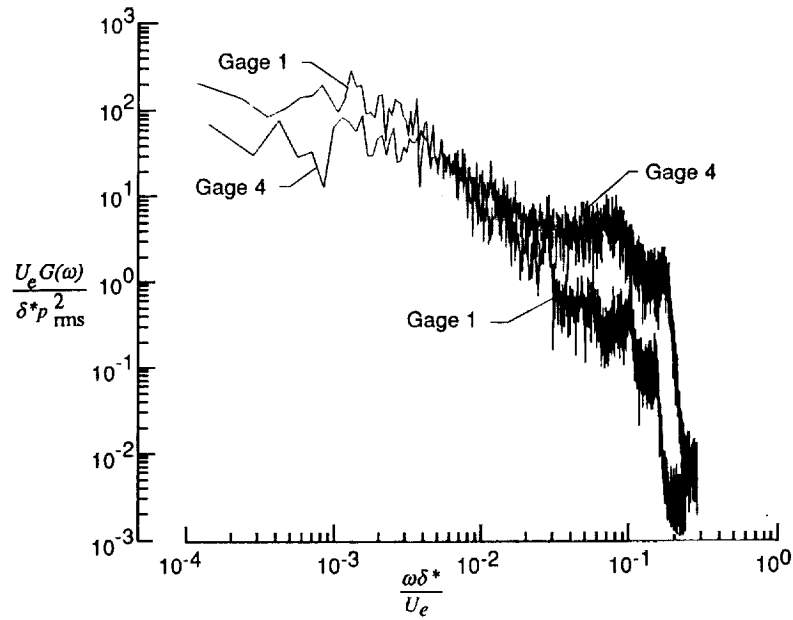


Figure 10. Pressure fluctuations at gage location 4 before inlet unstart for test R6B7.

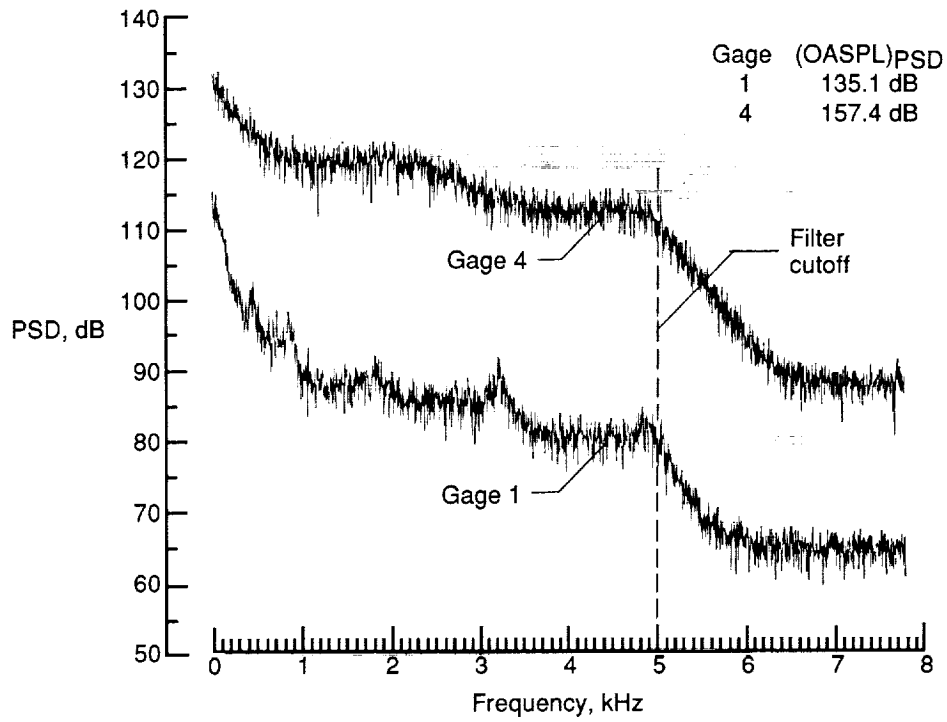


(a) Pressure spectra.

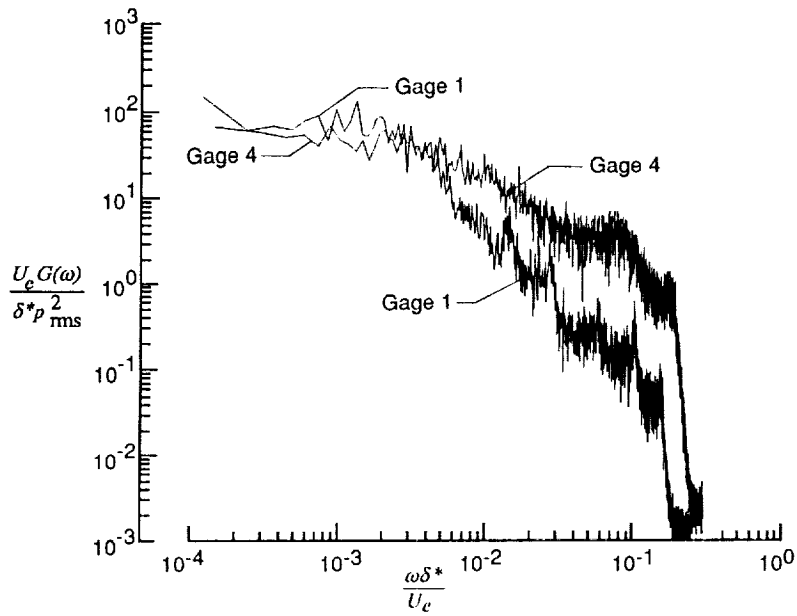


(b) Nondimensional spectra.

Figure 11. No-combustion case for test R6B7, Region I; 3.7 to 5.5 sec.

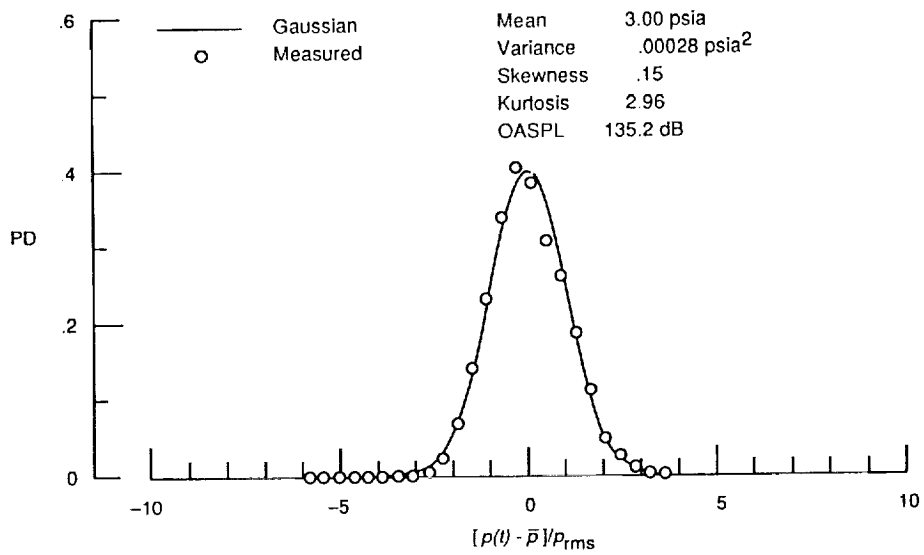


(a) Pressure spectra.

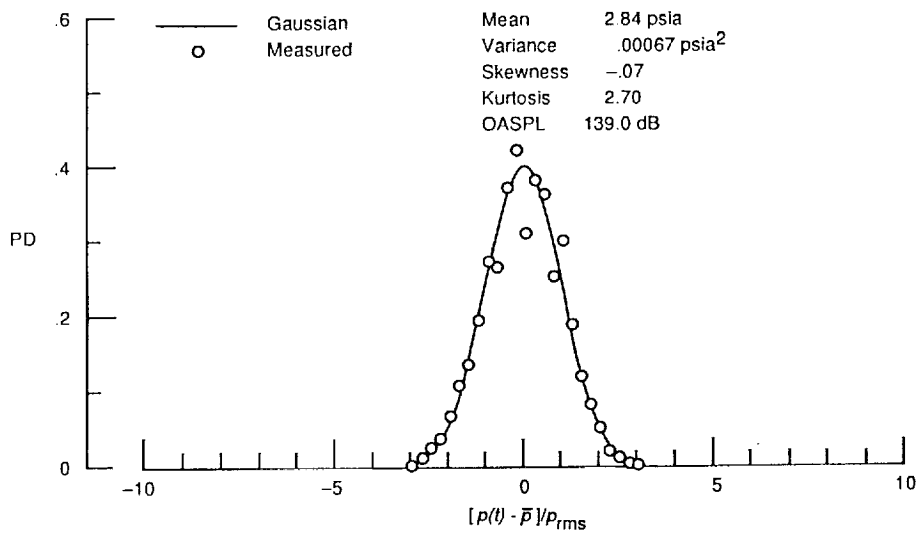


(b) Nondimensional spectra.

Figure 12. Combustion case for test R6B7, Region II; 10.0 to 12.3 sec.

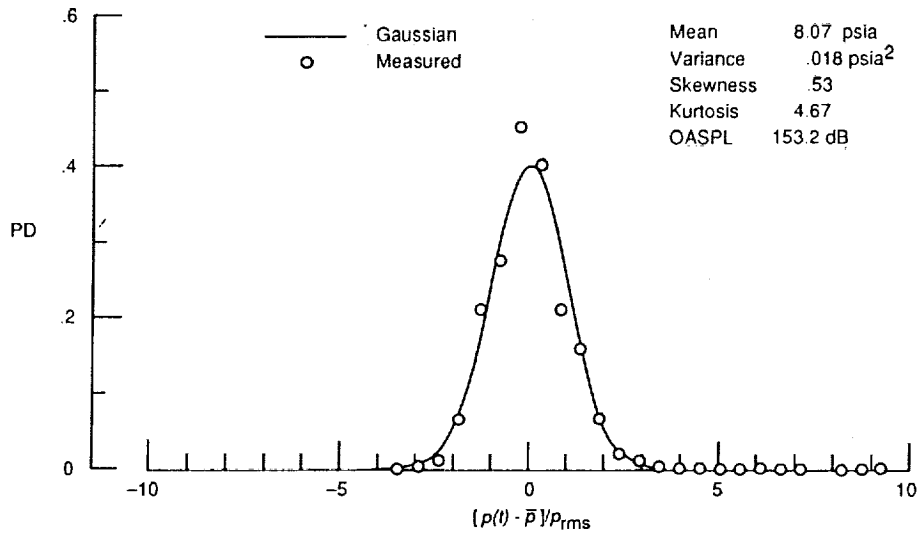


(a) Region I with no combustion.

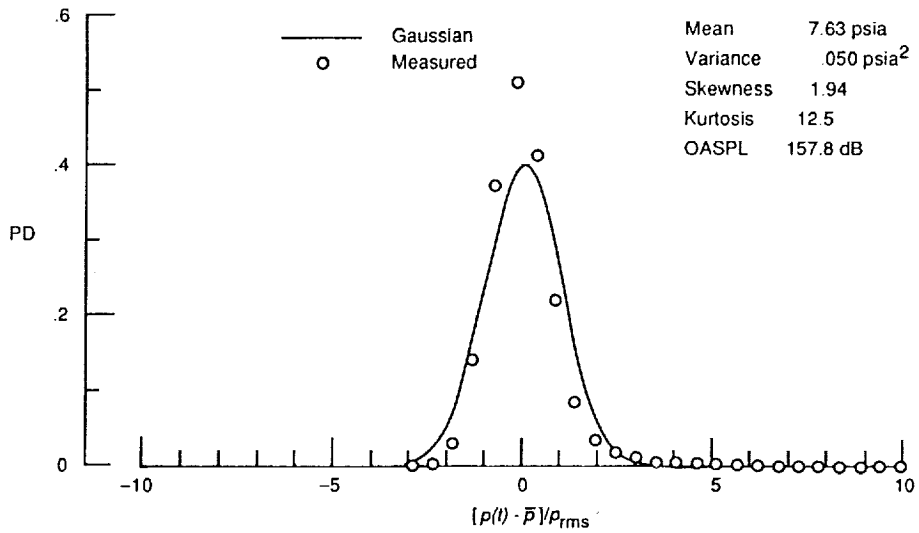


(b) Region II with combustion.

Figure 13. Probability density distribution of pressure time histories at gage location 1 for test R6B7.



(a) Region I with no combustion.



(b) Region II with combustion.

Figure 14. Probability density distribution of pressure time histories at gage location 4 for test R6B7.

Series	Time, sec	Cycle	ϕ
1	13.6	20	0.414
2	14.3	21	.422
3	15.0	22	.486 ^a
4	15.6	23	.523

^a Acquired during transition to unstart.

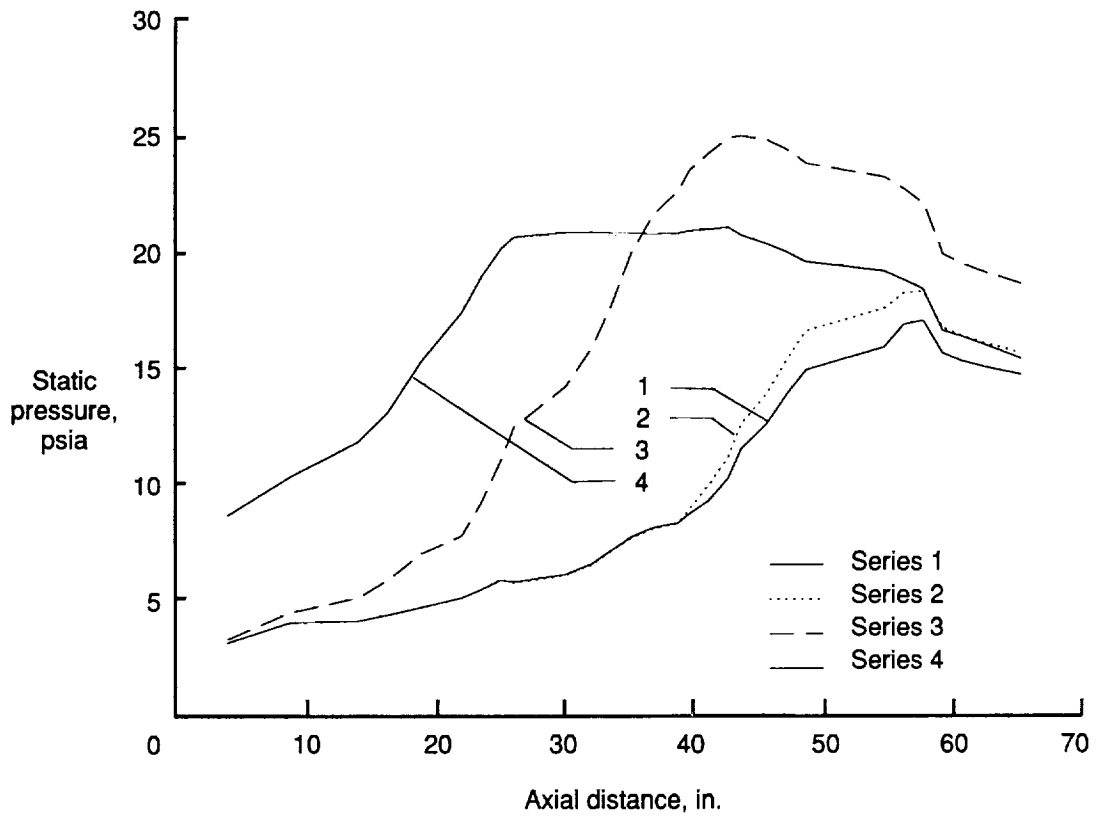


Figure 15. Axial static pressure distribution versus time for test R15B6.

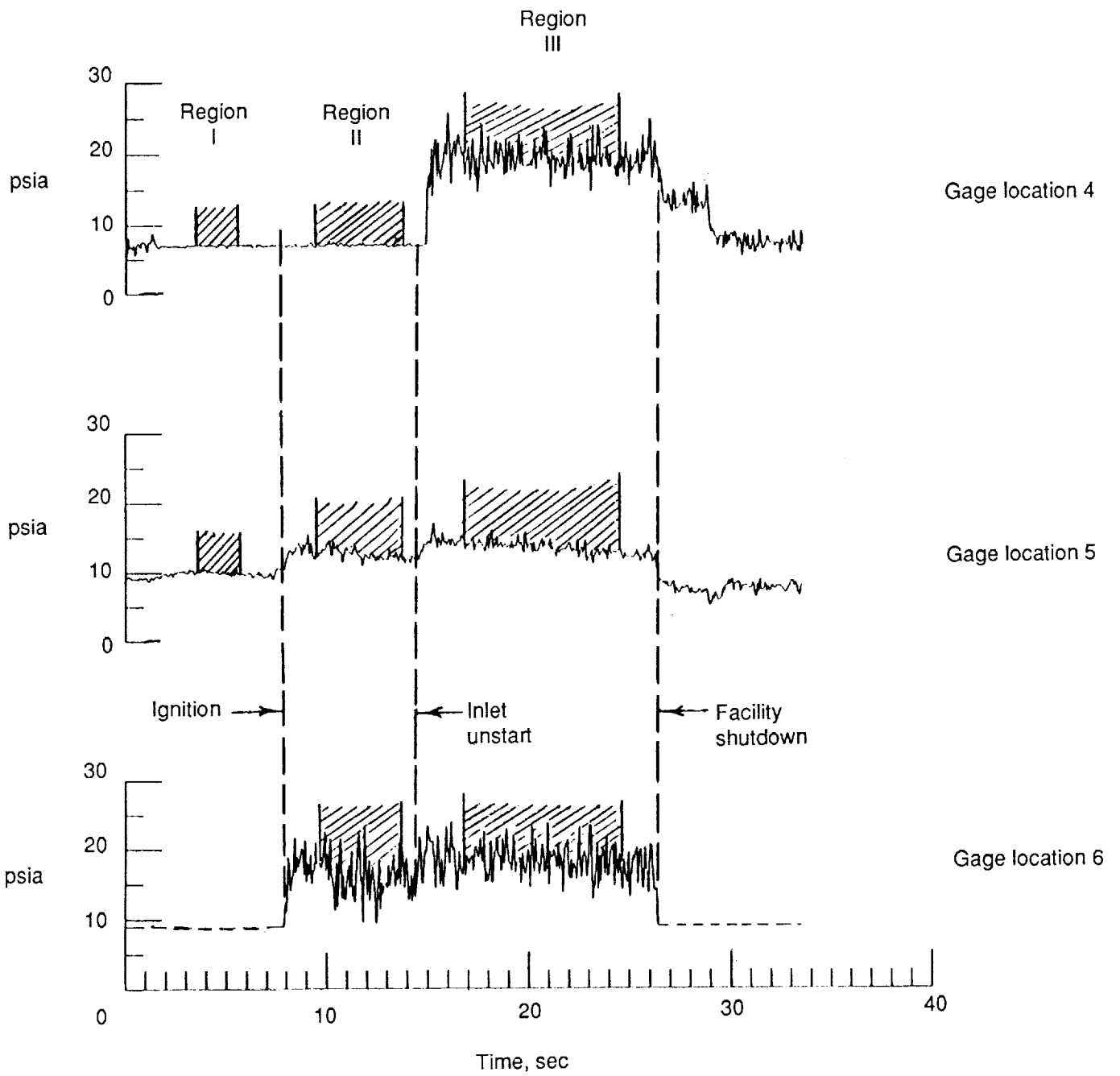
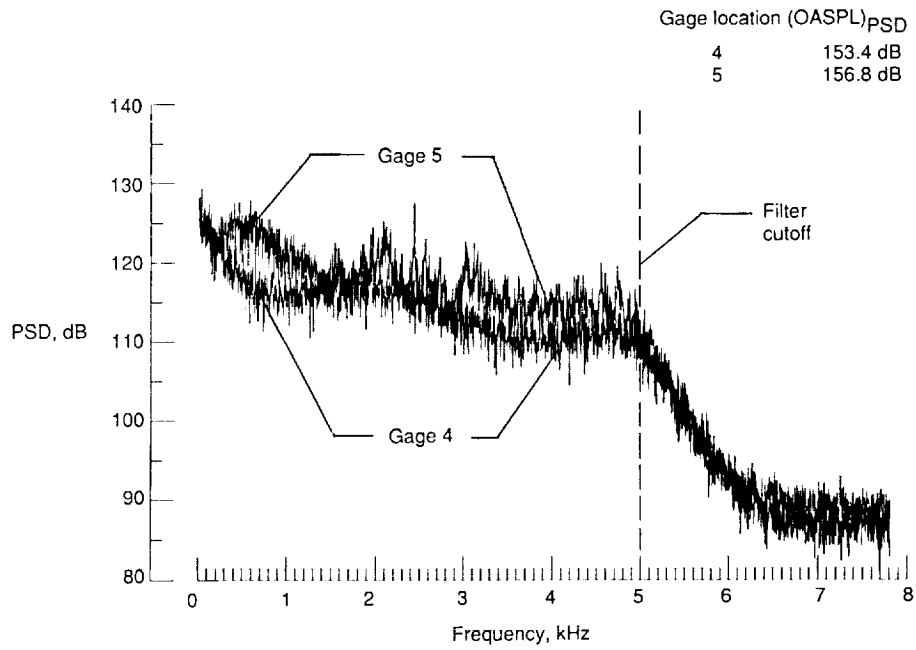
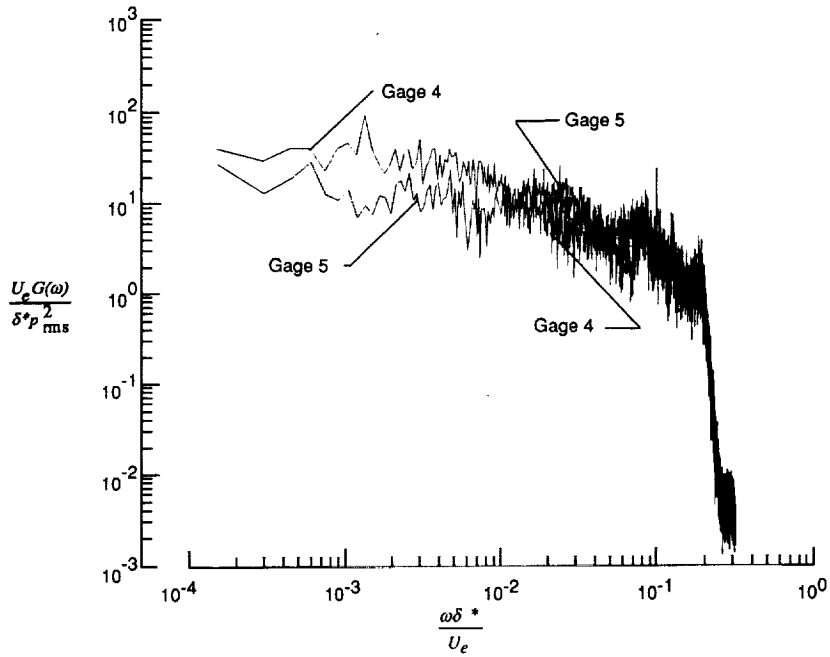


Figure 16. Pressure time histories during an unstart for test R15B6.

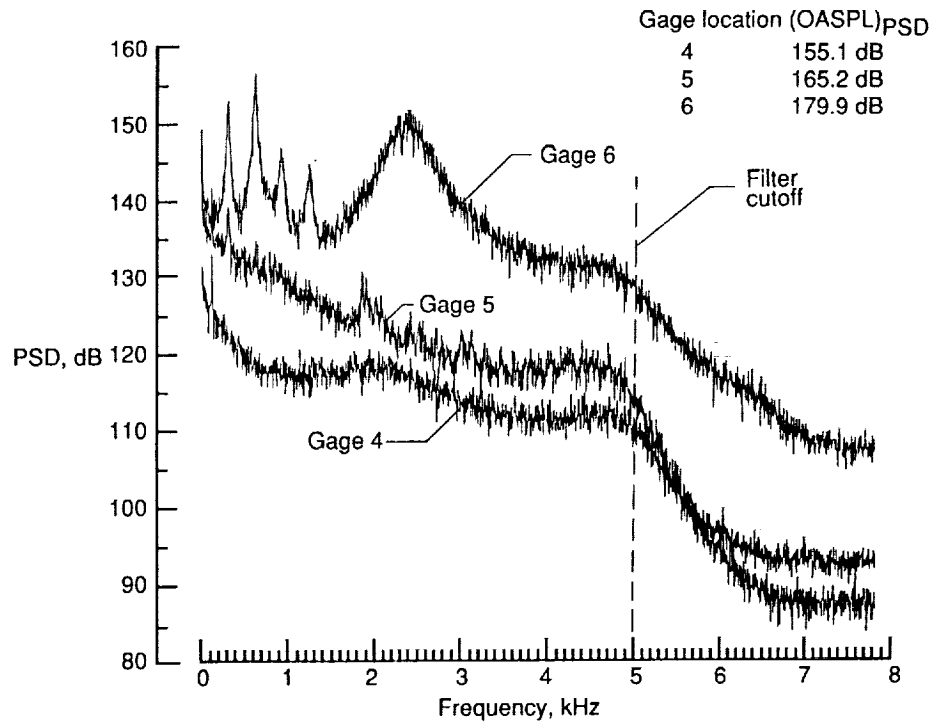


(a) Pressure spectra.

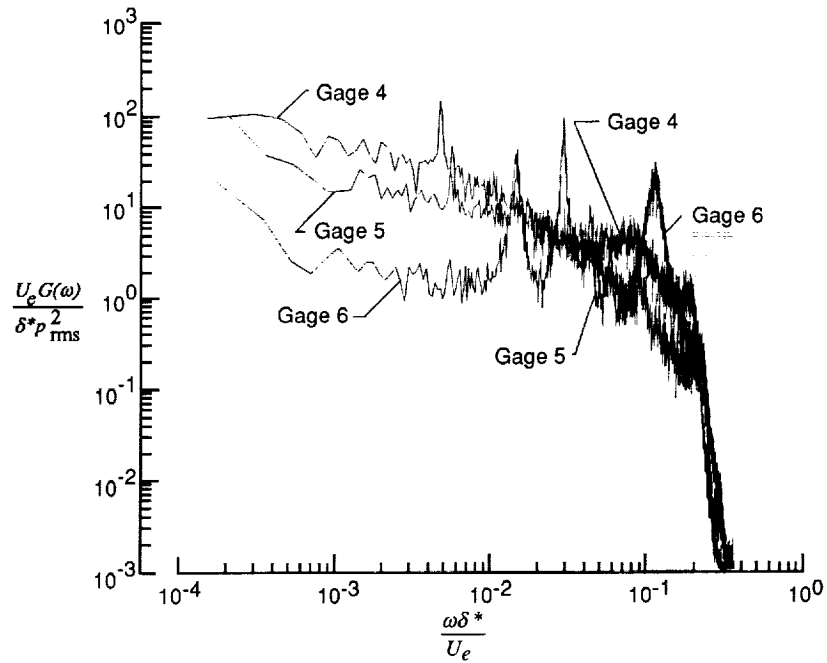


(b) Nondimensional spectra.

Figure 17. No-combustion case for test R15B6, Region I; 3.1 to 5.2 sec.

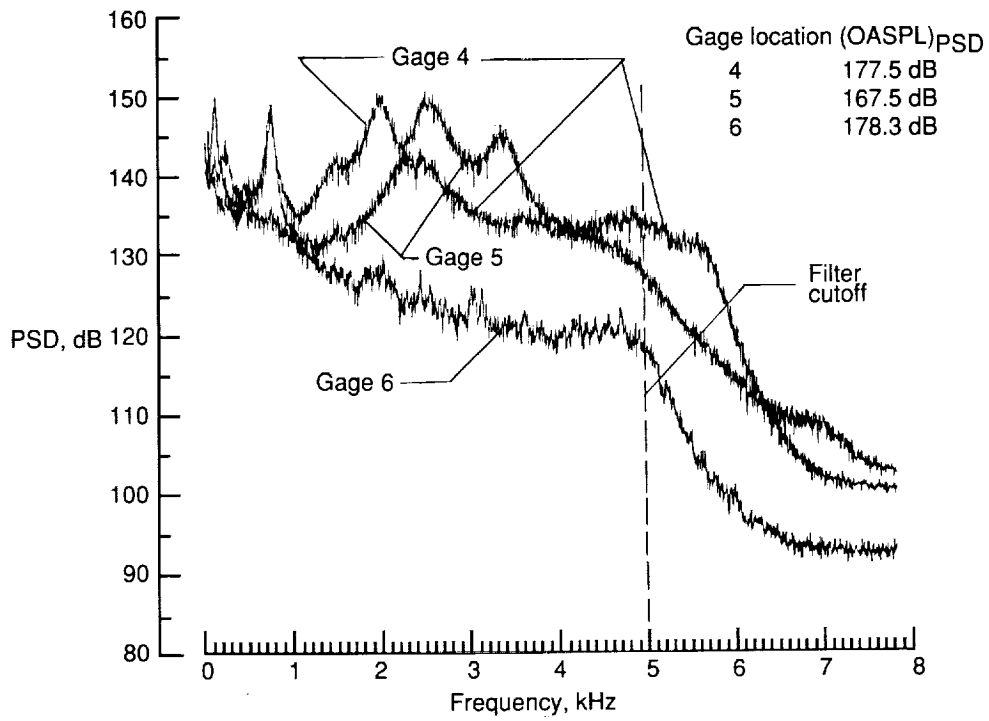


(a) Pressure spectra.

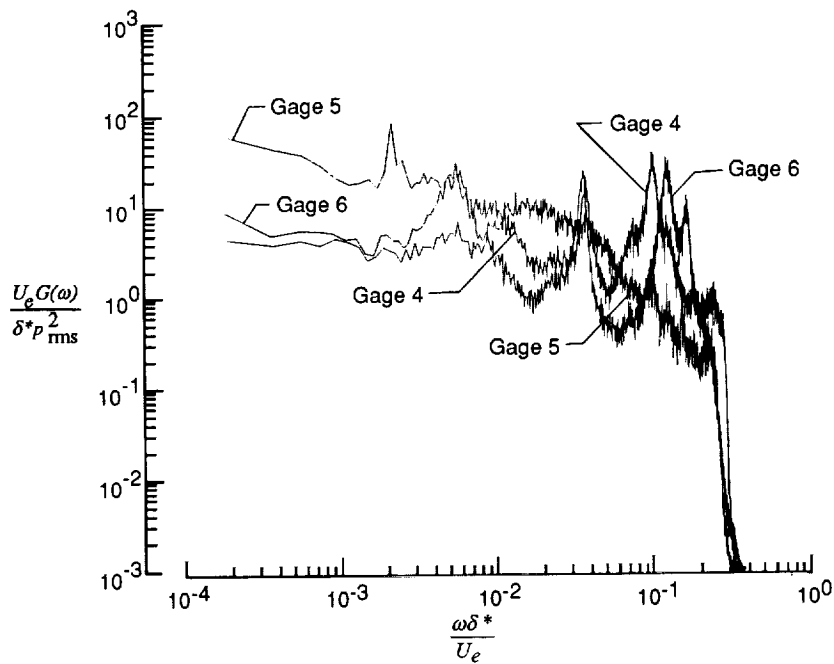


(b) Nondimensional spectra.

Figure 18. Combustion case for test R15B6, Region II; 9.4 to 13.4 sec.

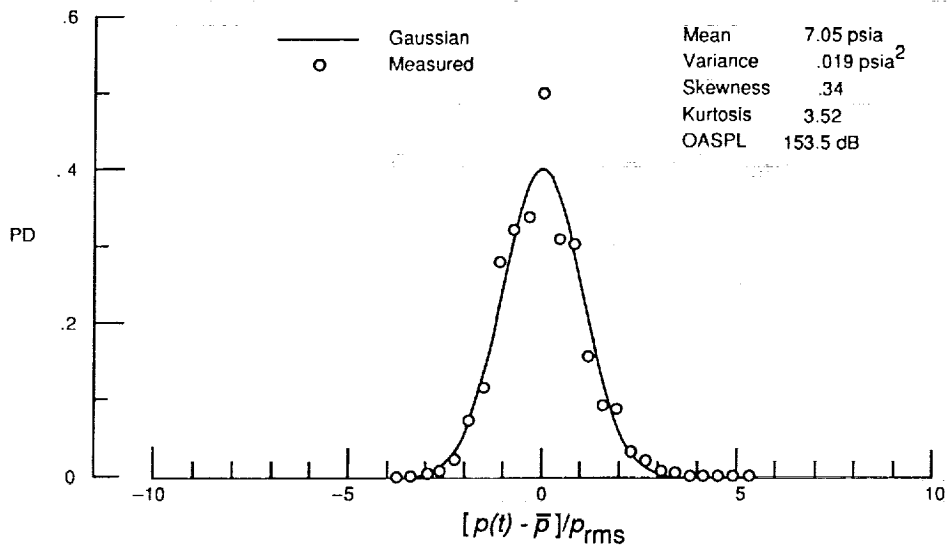


(a) Pressure spectra.

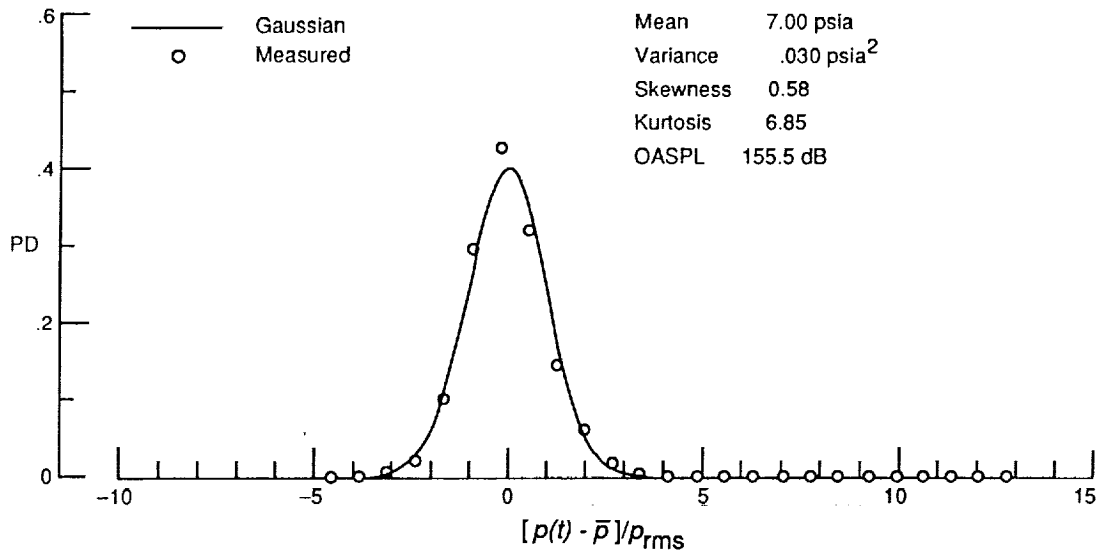


(b) Nondimensional spectra.

Figure 19. Inlet unstarted case for test R15B6, Region III; 16.3 to 24.4 sec.

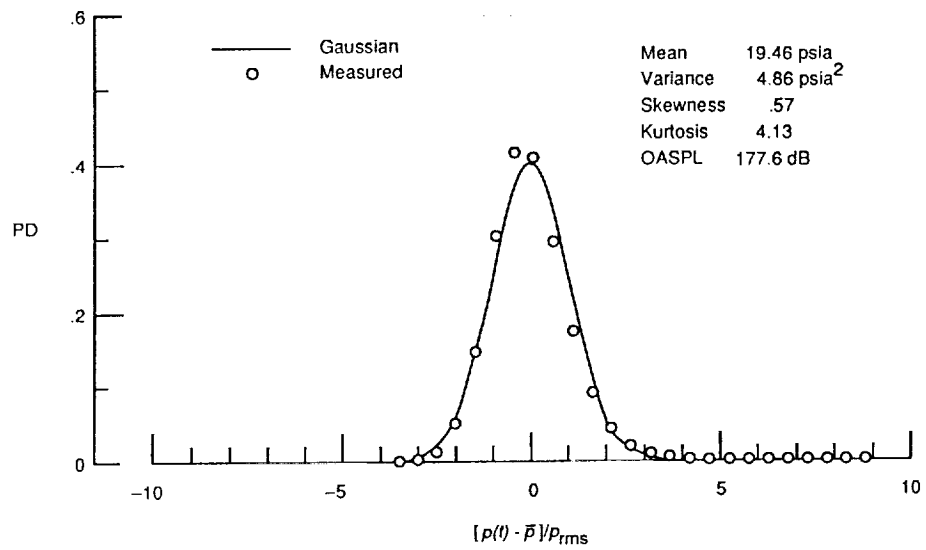


(a) Region I with no combustion.



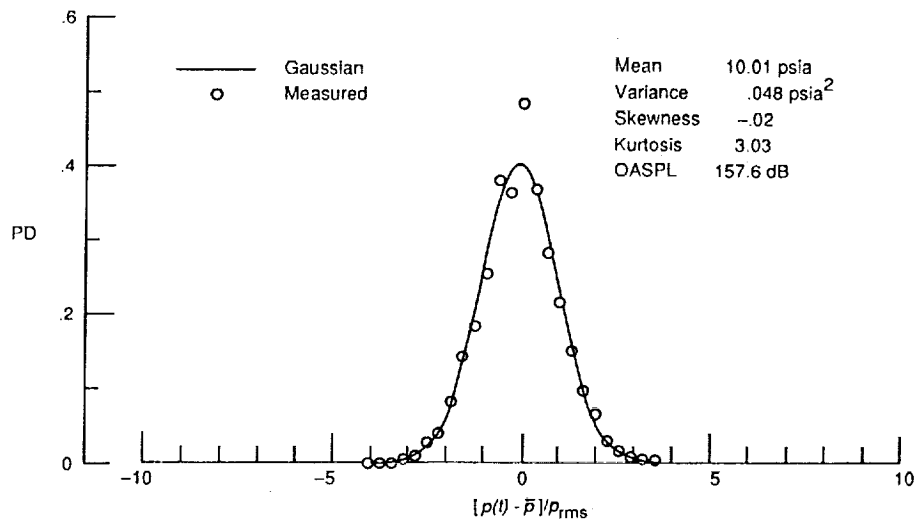
(b) Region II with combustion.

Figure 20. Probability density distribution of pressure time histories at gage location 4 for test R15B6.

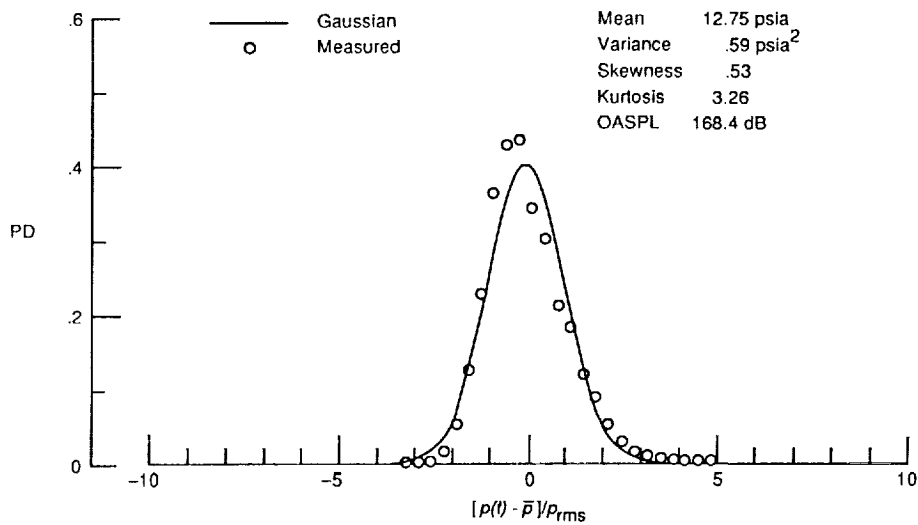


(c) Region III with inlet unstarted.

Figure 20. Concluded.

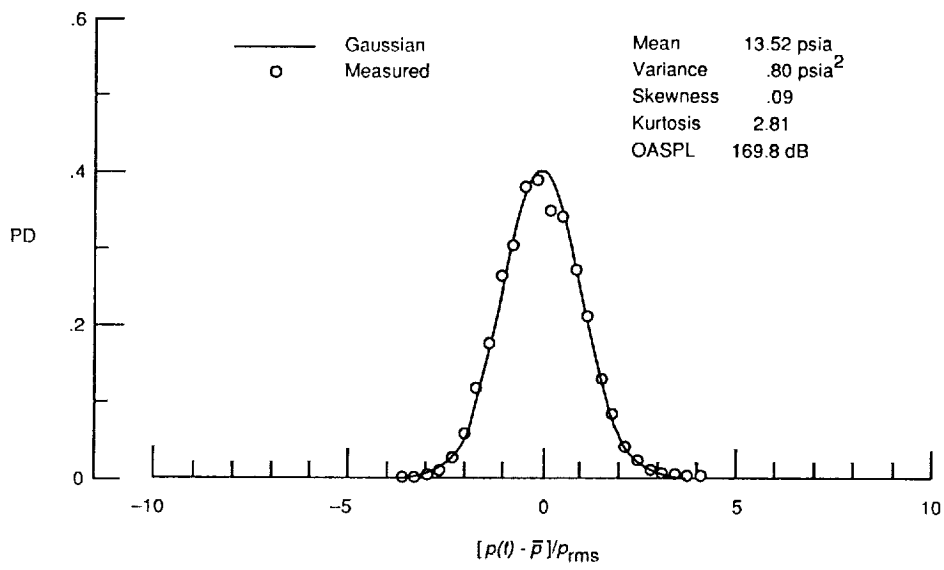


(a) Region I with no combustion.



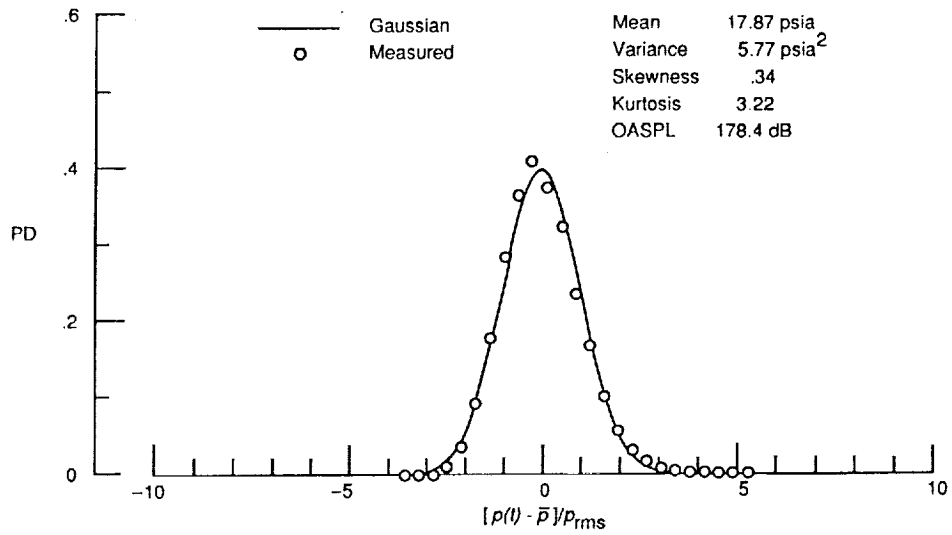
(b) Region II with combustion.

Figure 21. Probability density distribution of pressure time histories at gage location 5 for test R15B6.

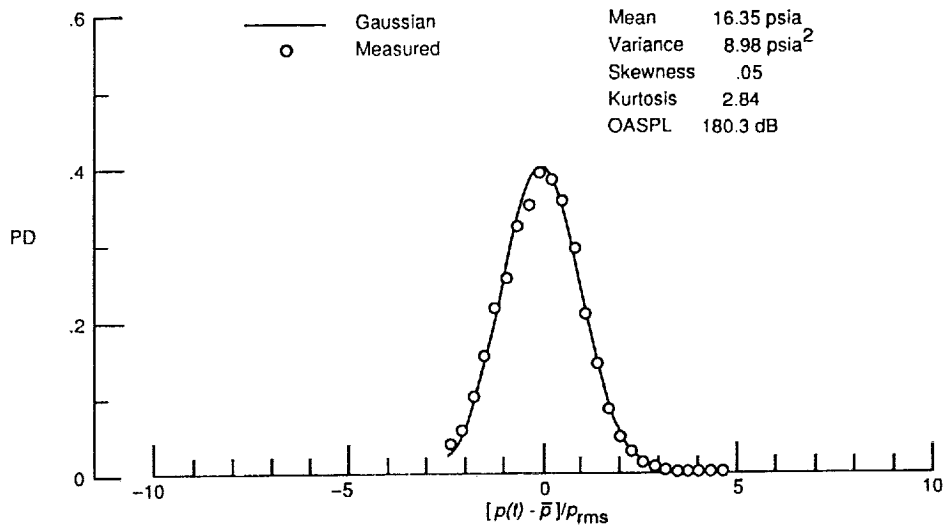


(c) Region III with inlet unstarted.

Figure 21. Concluded.



(a) Region II with combustion.



(b) Region III with inlet unstated.

Figure 22. Probability density distribution of pressure time histories at gage location 6 for test R15B6.

Series	Time, sec	Cycle	ϕ
1	16.0	19	0.354
2	16.8	20	.361
3	17.6	21	.533

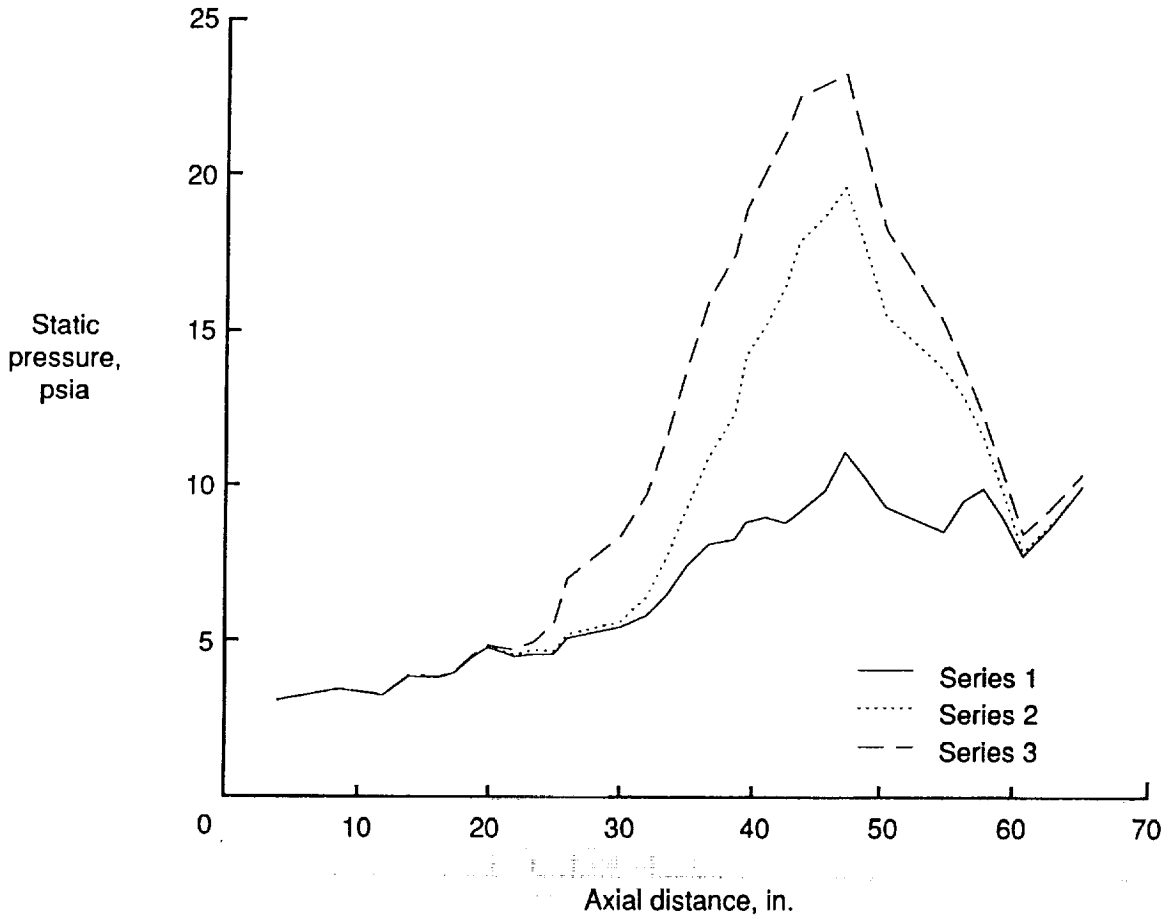
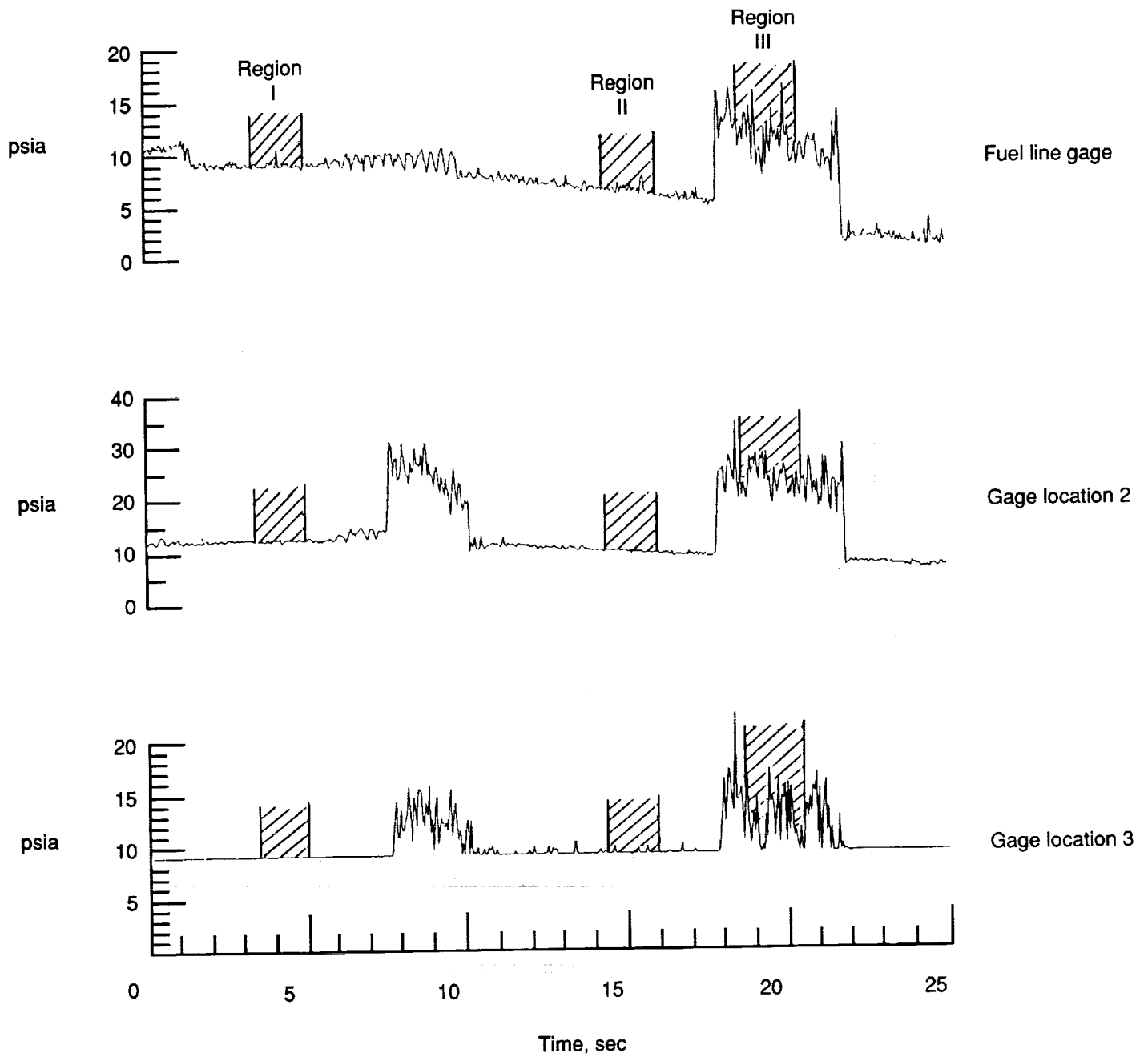
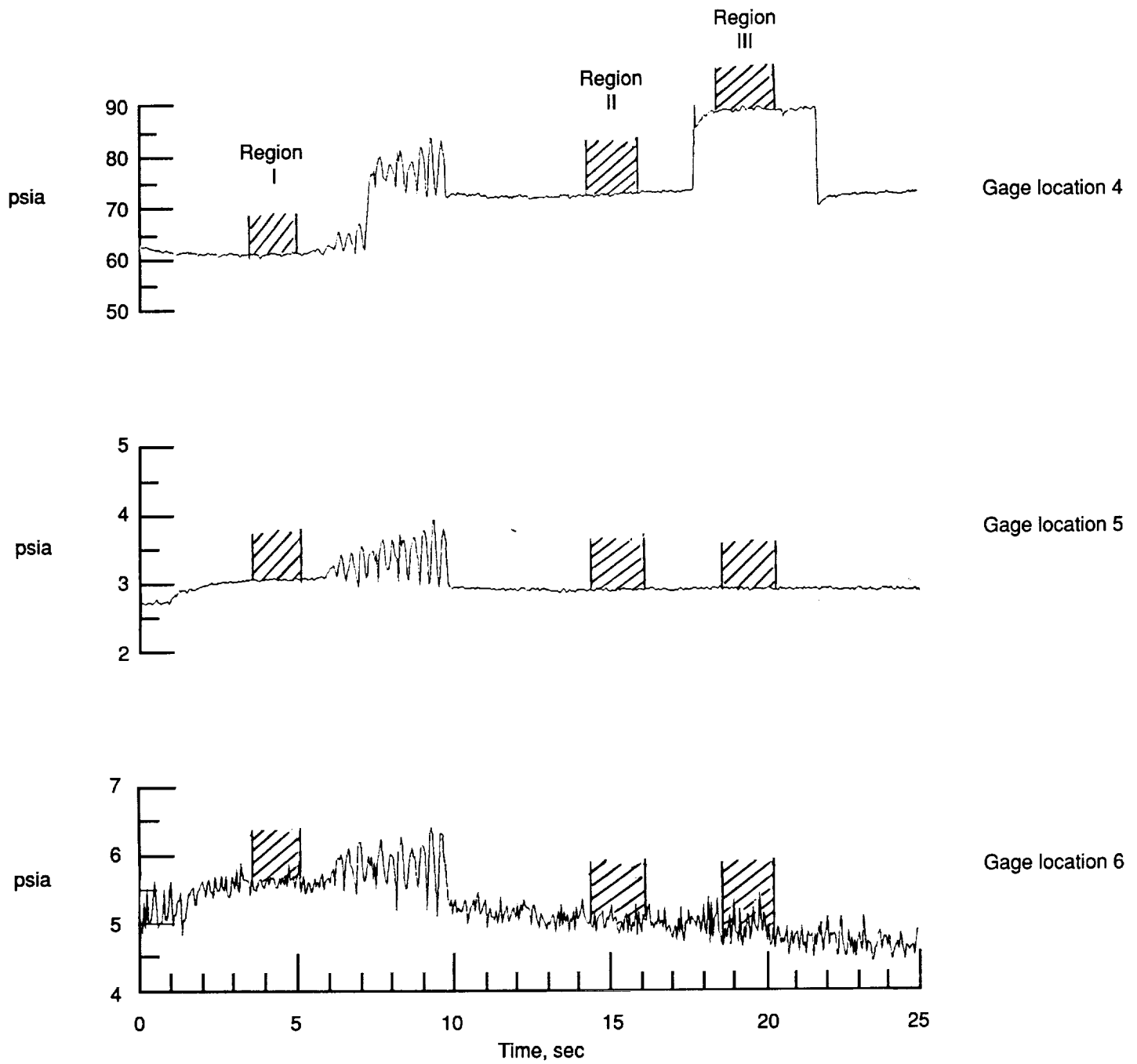


Figure 23. Axial static pressure distribution versus time for test R50B10.



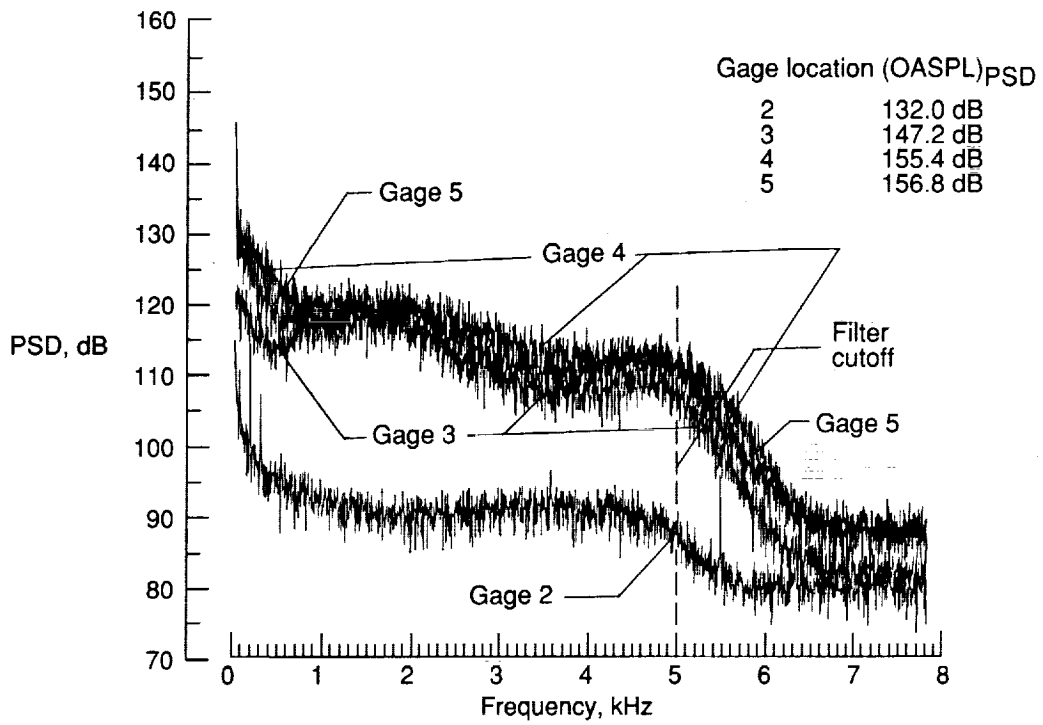
(a) Fuel line gage plus gage locations 2 and 3.

Figure 24. Pressure time histories during varied heat release for test R50B10.

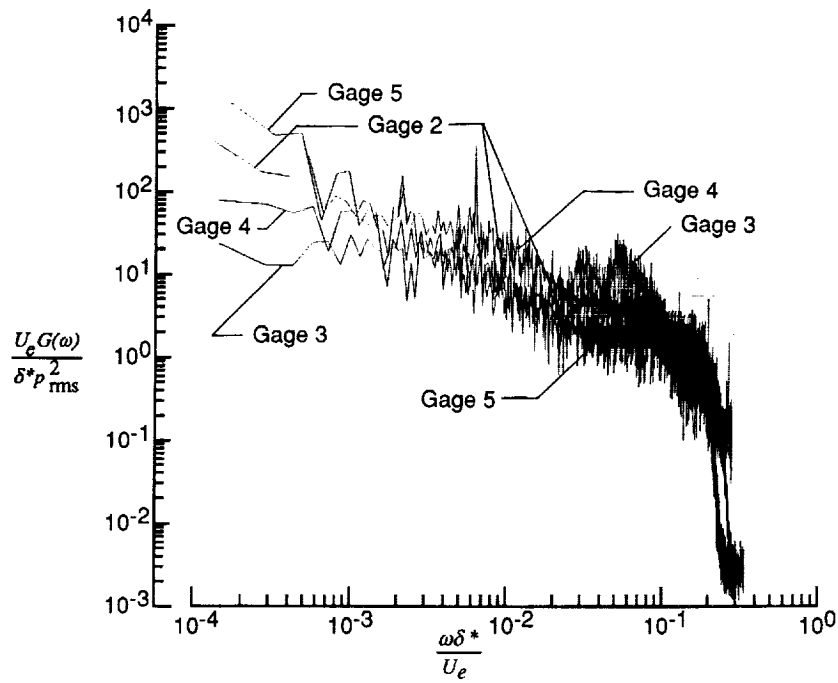


(b) Gage locations 4, 5, and 6.

Figure 24. Concluded.

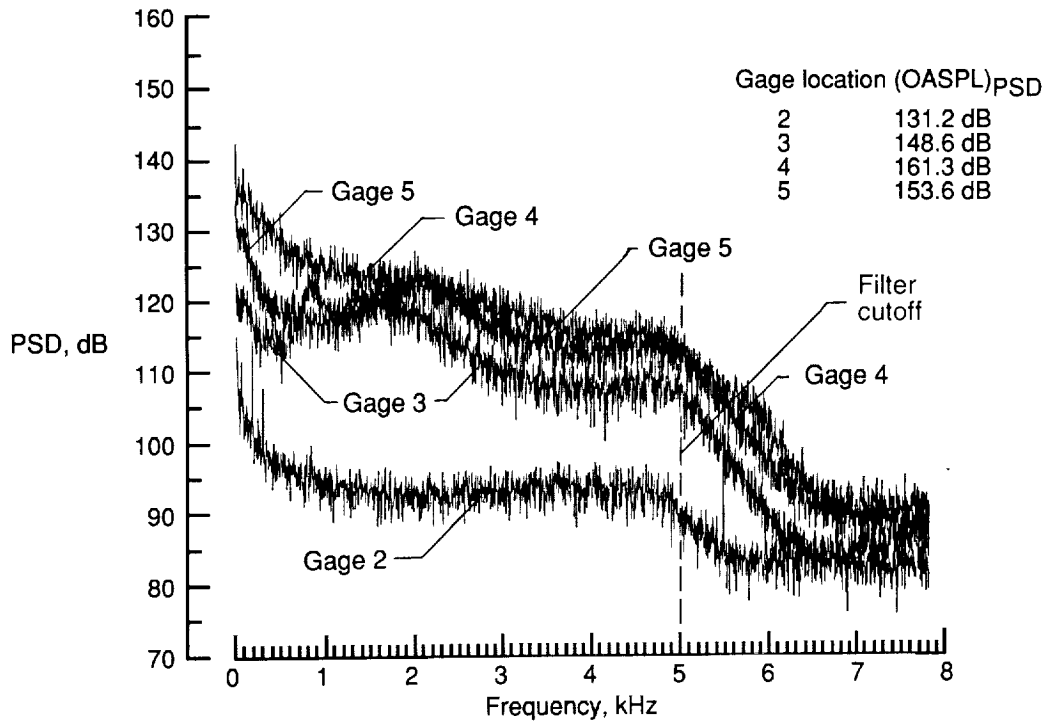


(a) Pressure spectra.

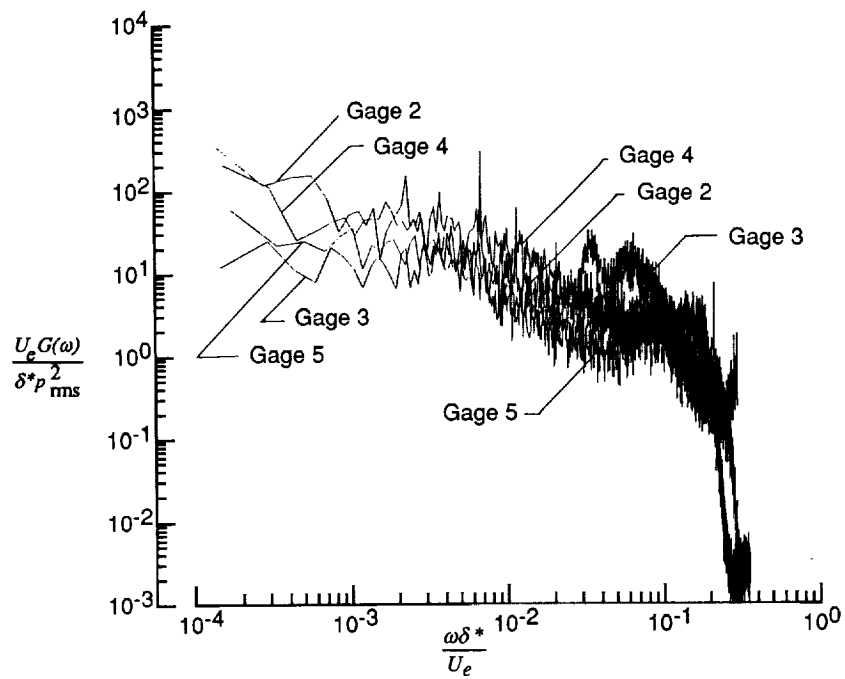


(b) Nondimensional spectra.

Figure 25. Test R50B10 with no heat release, Region I; 3.1 to 5.0 sec.

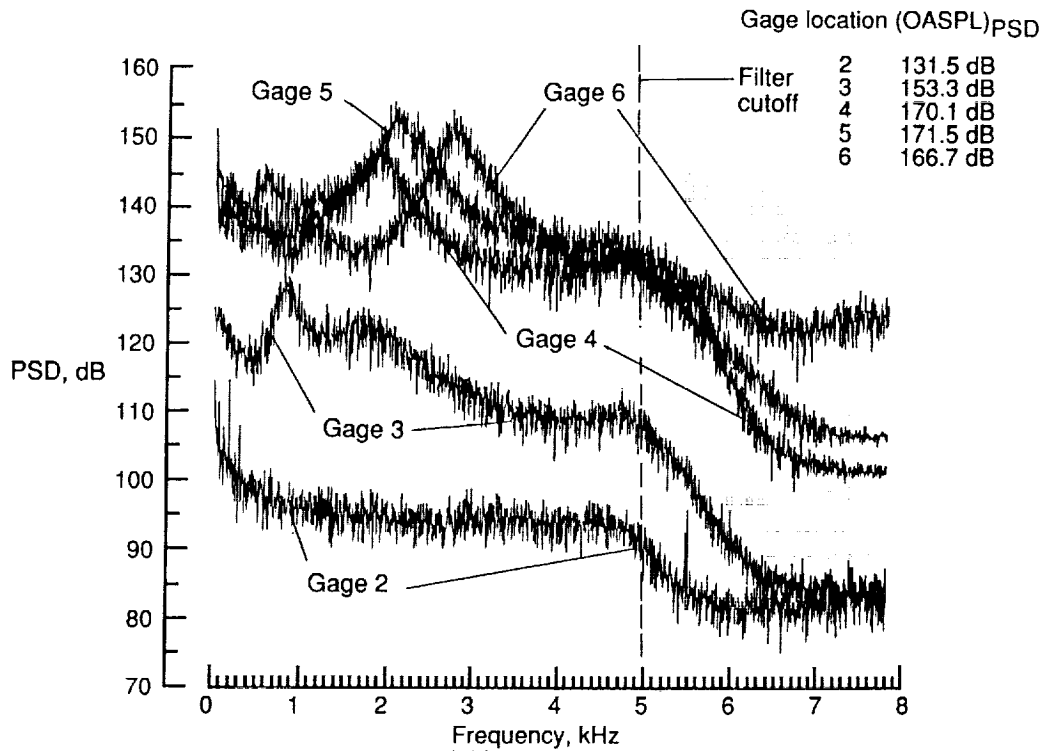


(a) Pressure spectra.

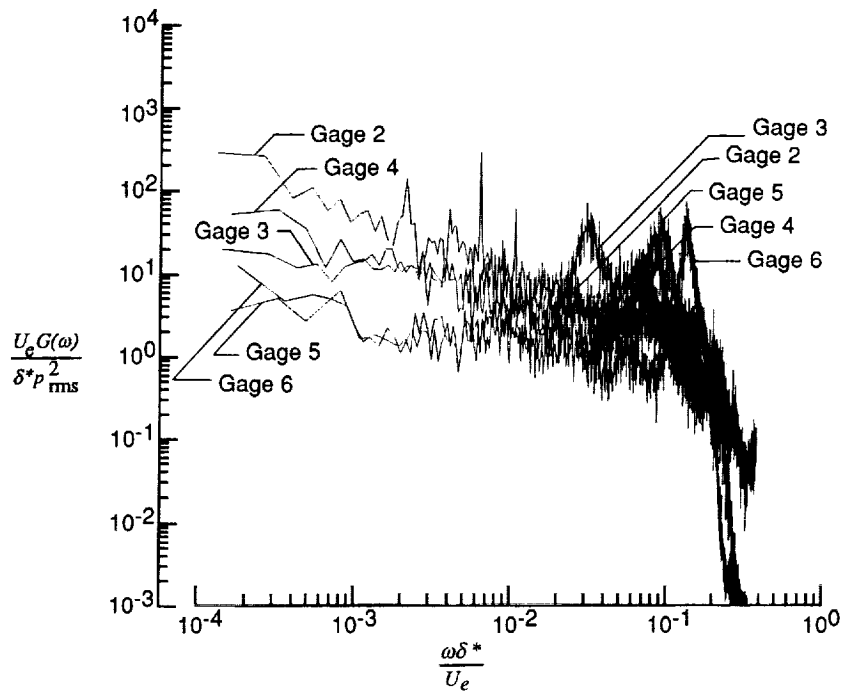


(b) Nondimensional spectra.

Figure 26. Test R50B10 with low heat release, Region II; 14.2 to 16.0 sec.

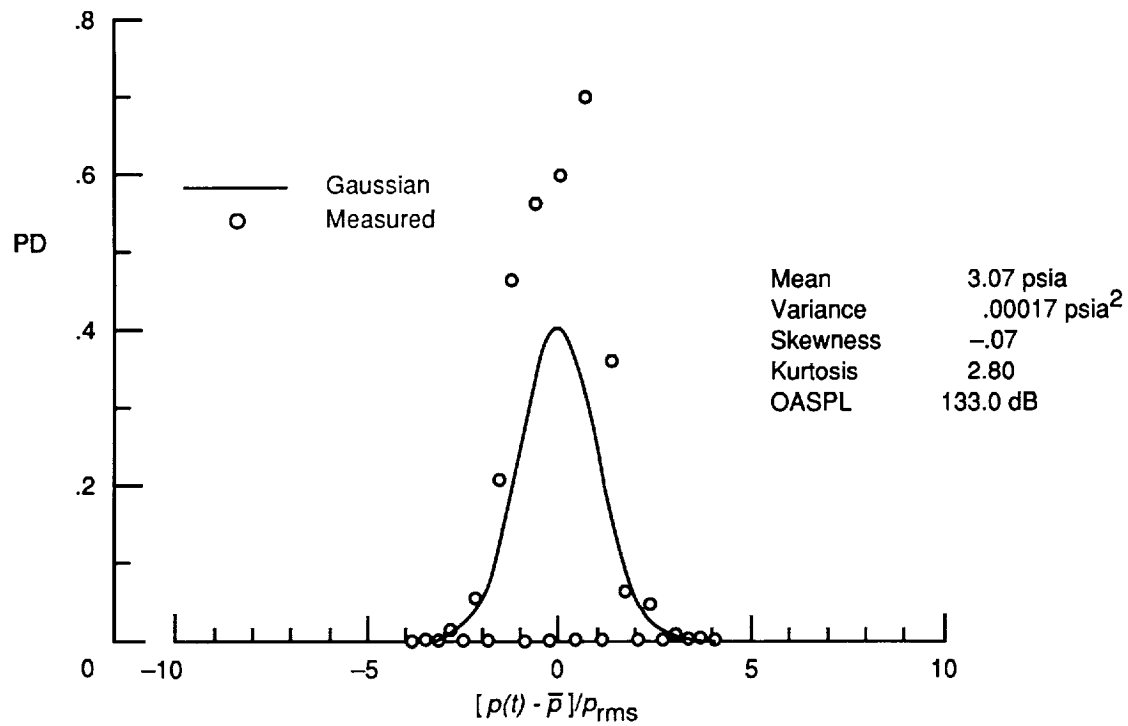


(a) Pressure spectra.

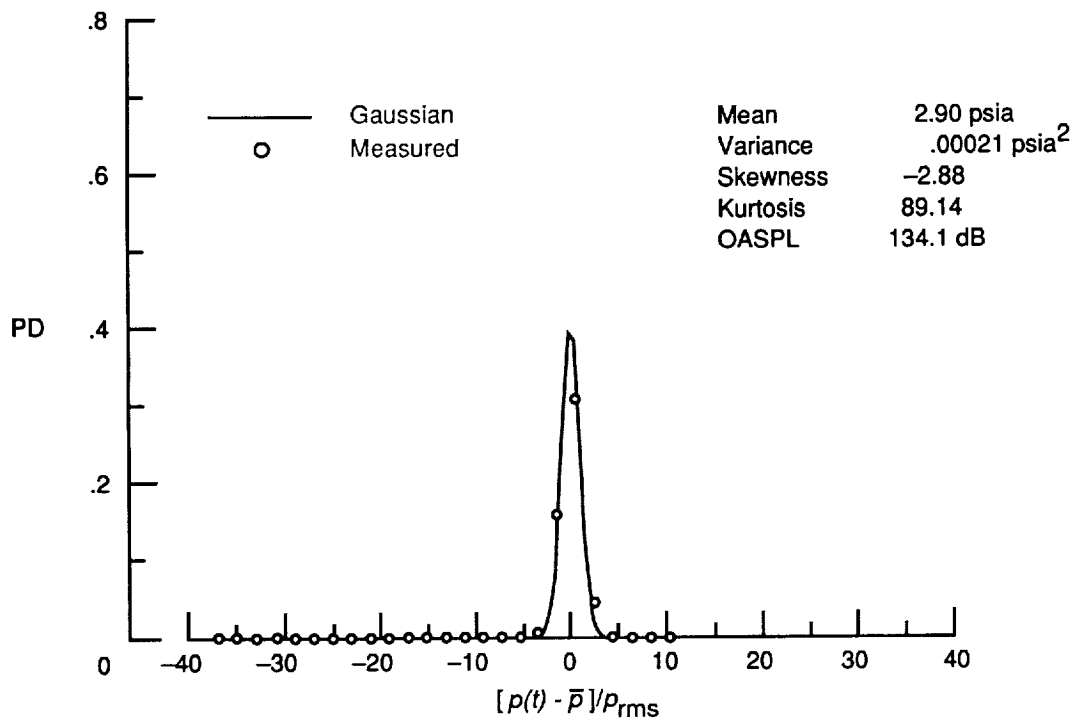


(b) Nondimensional spectra.

Figure 27. Test R50B10 with high heat release, Region III; 18.3 to 20.2 sec.

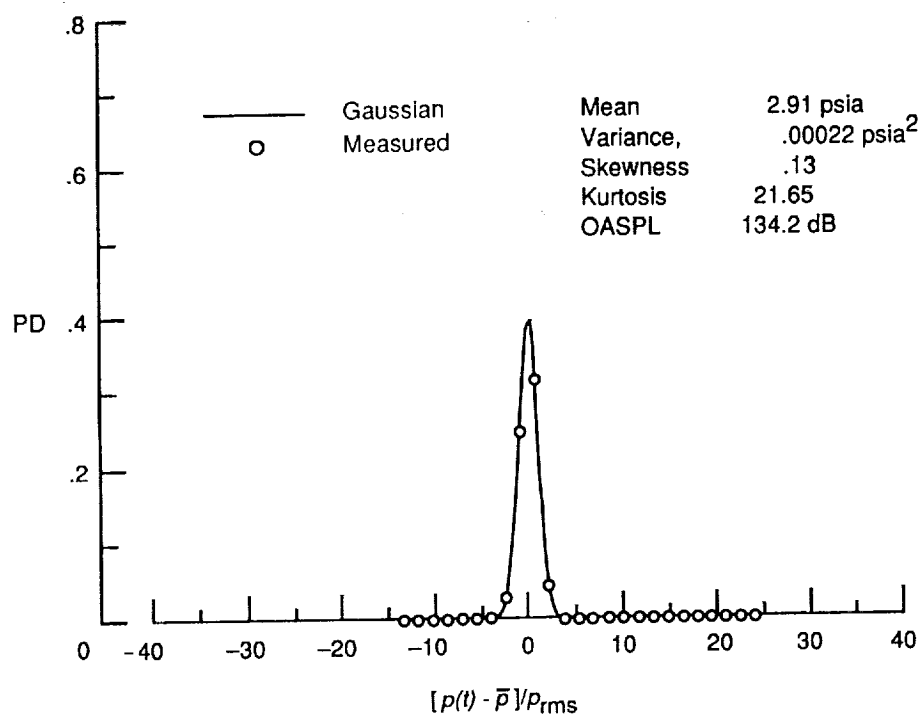


(a) Region I with no heat release.



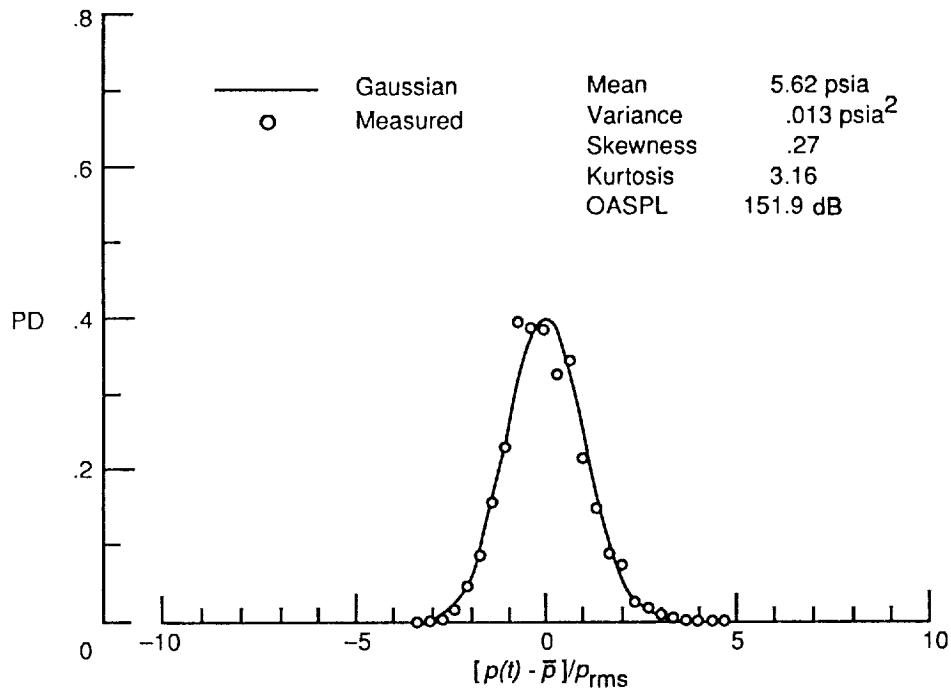
(b) Region II with low heat release.

Figure 28. Probability density distribution of pressure time histories at gage location 2 for test R50B10.

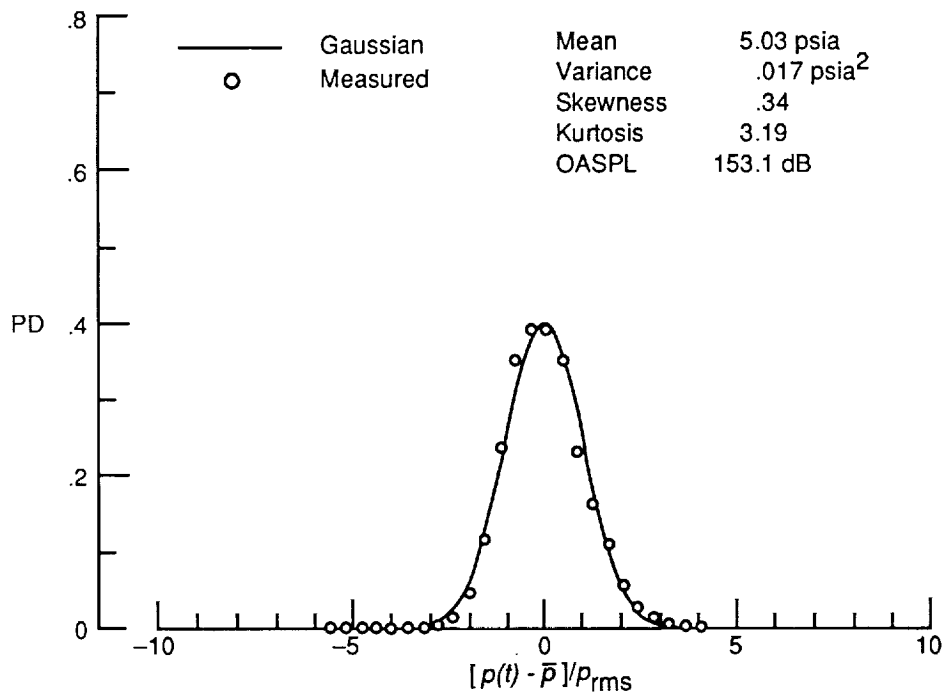


(c) Region III with high heat release.

Figure 28. Concluded.

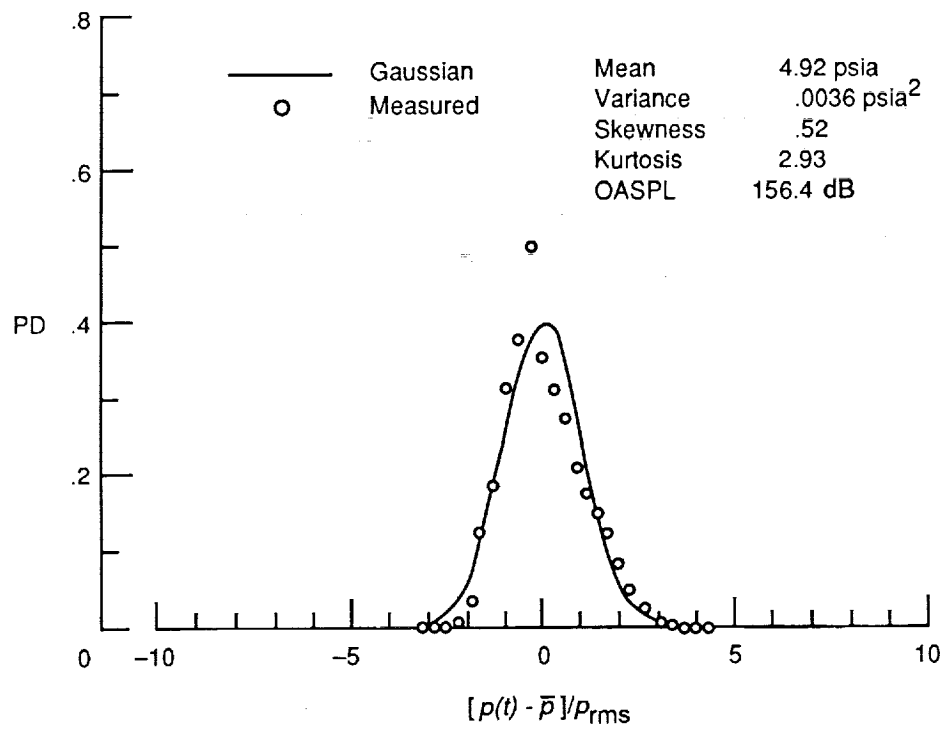


(a) Region I with no heat release.



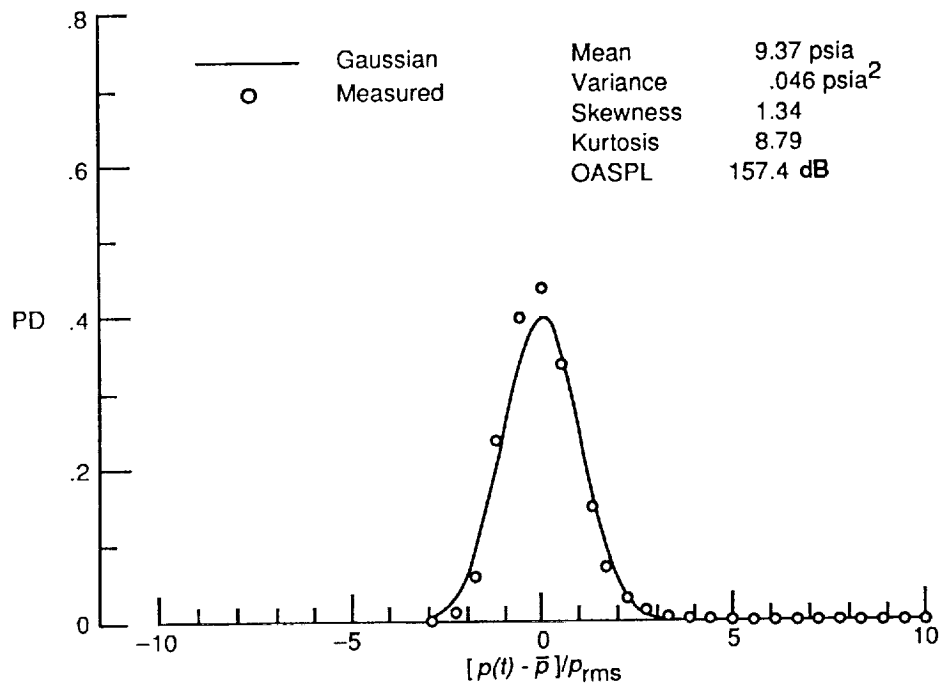
(b) Region II with low heat release.

Figure 29. Probability density distribution of pressure time histories at gage location 3 for test R50B10.

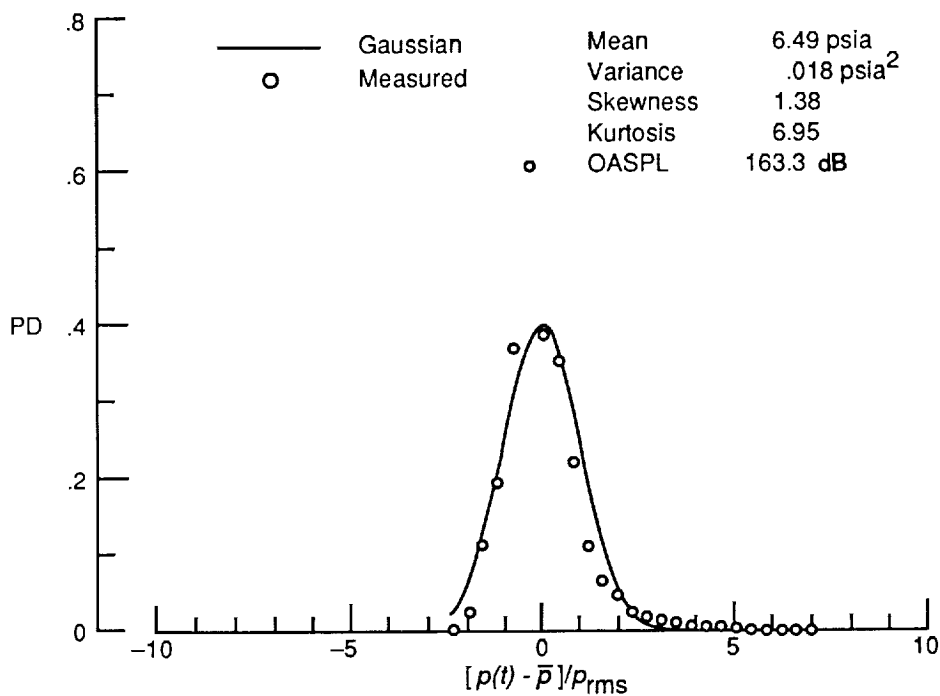


(c) Region III with high heat release.

Figure 29. Concluded.

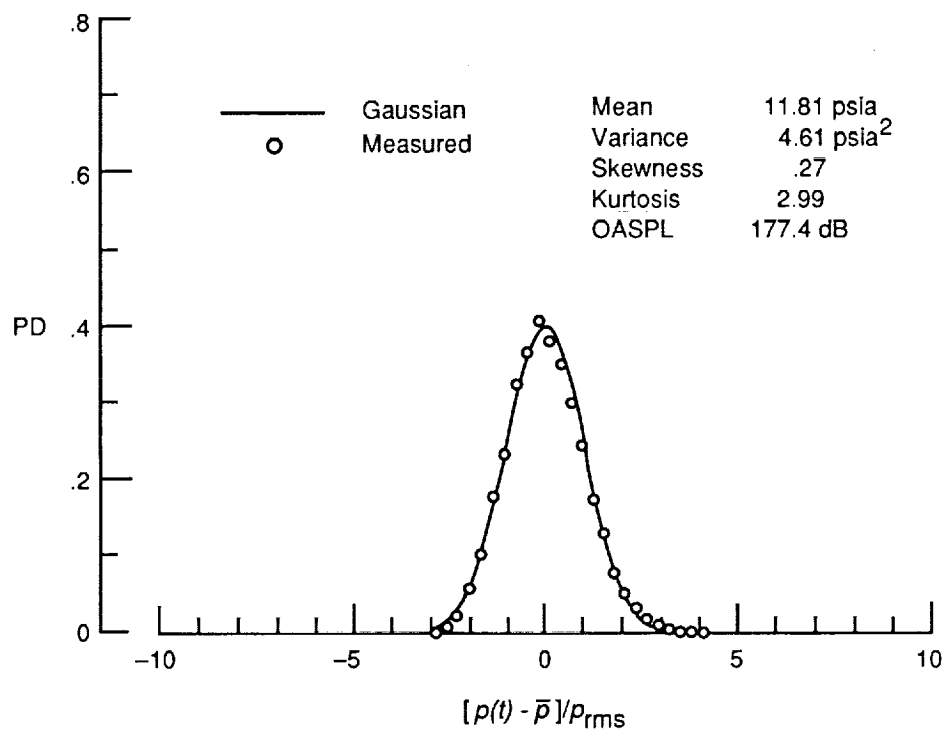


(a) Region I with no heat release.



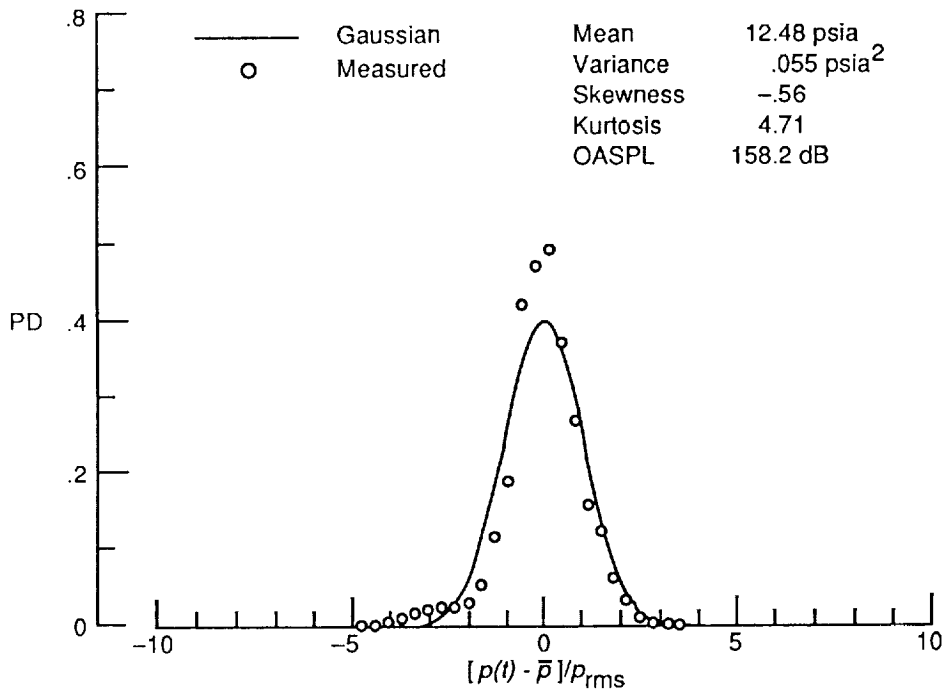
(b) Region II with low heat release.

Figure 30. Probability density distribution of pressure time histories at gage location 4 for test R50B10.

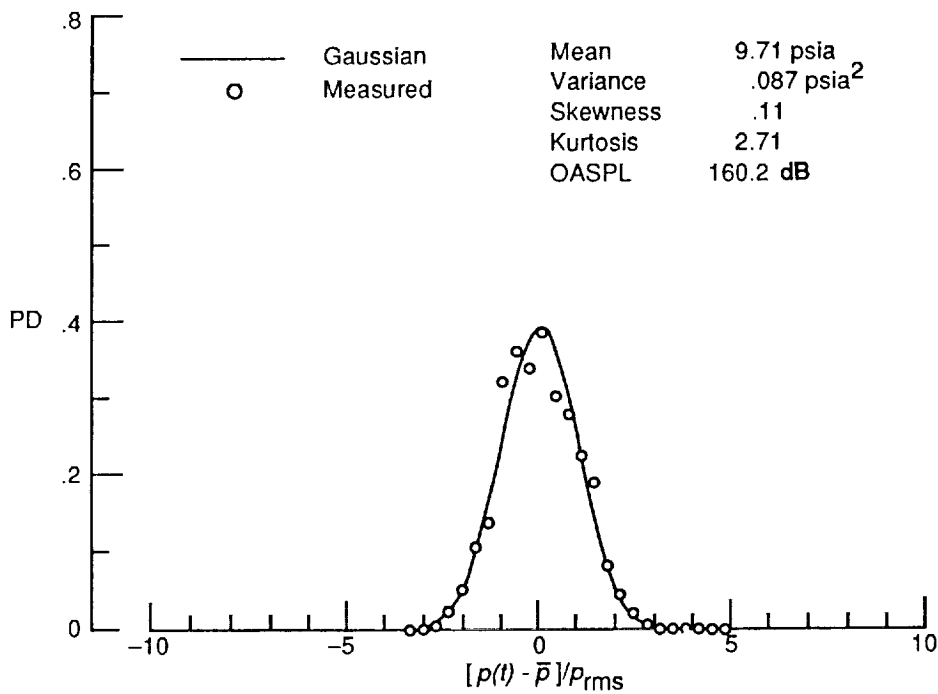


(c) Region III with high heat release.

Figure 30. Concluded.

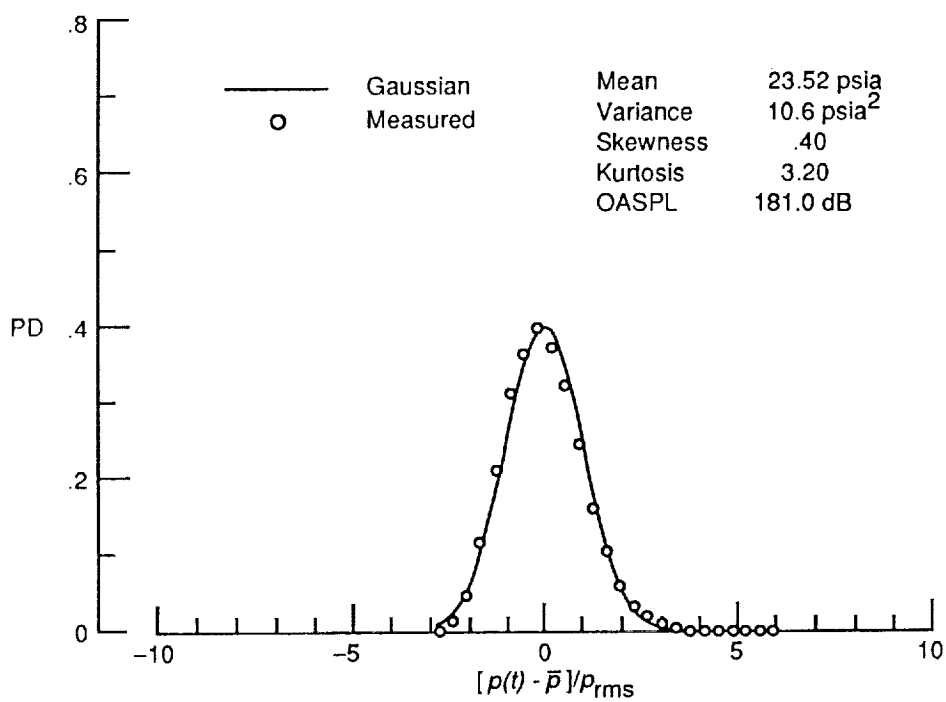


(a) Region I with no heat release.



(b) Region II with low heat release.

Figure 31. Probability density distribution of pressure time histories at gage location 5 for test R50B10.



(c) Region III with high heat release.

Figure 31. Concluded.

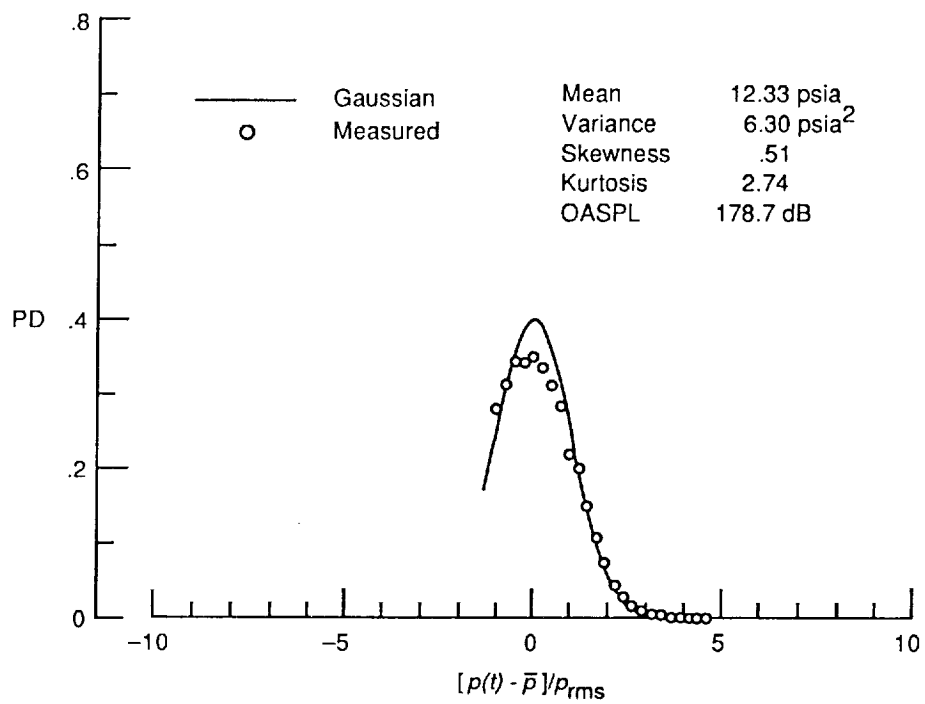


Figure 32. Probability density distribution of pressure time histories at gage location 6 for test R50B10, Region III; High heat release.

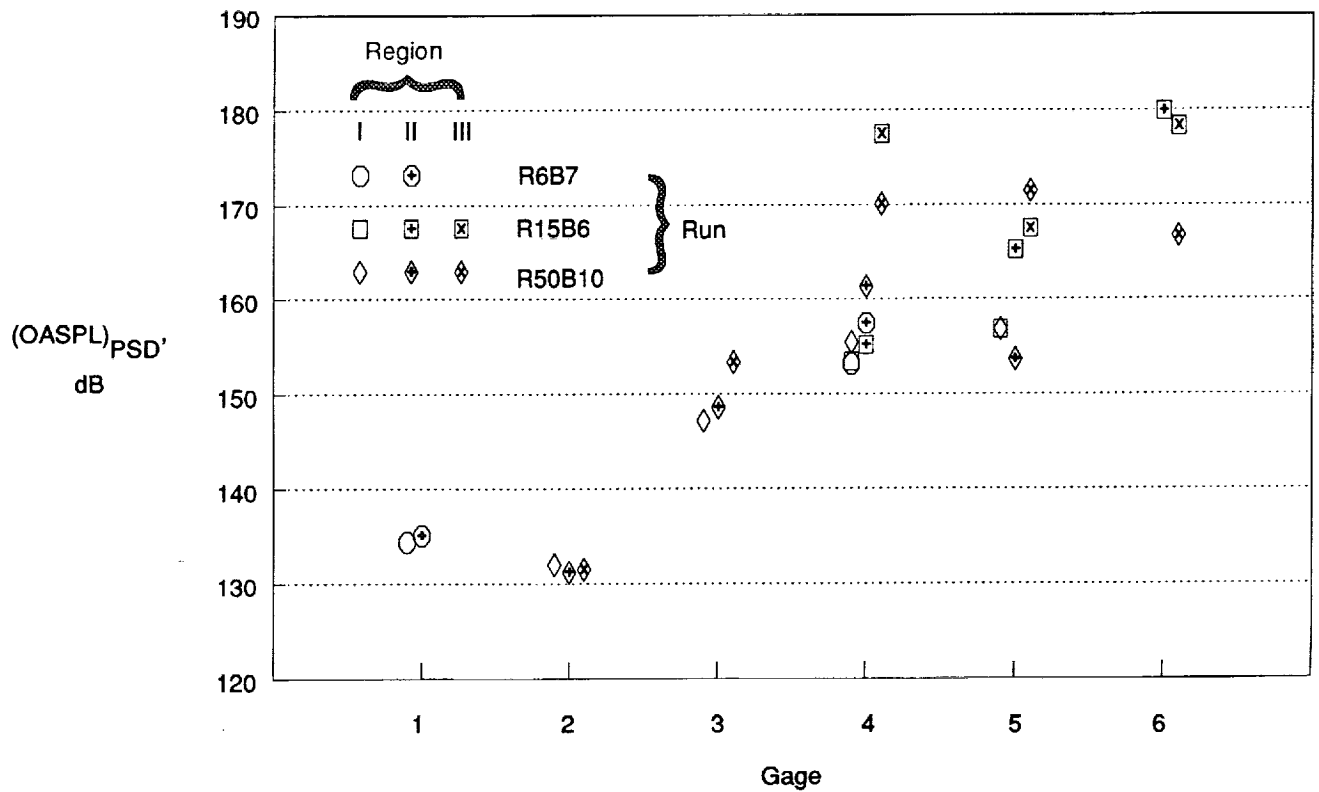


Figure 33. Summary of values of $(OASPL)_{PSD}$ for all tests and time regions.

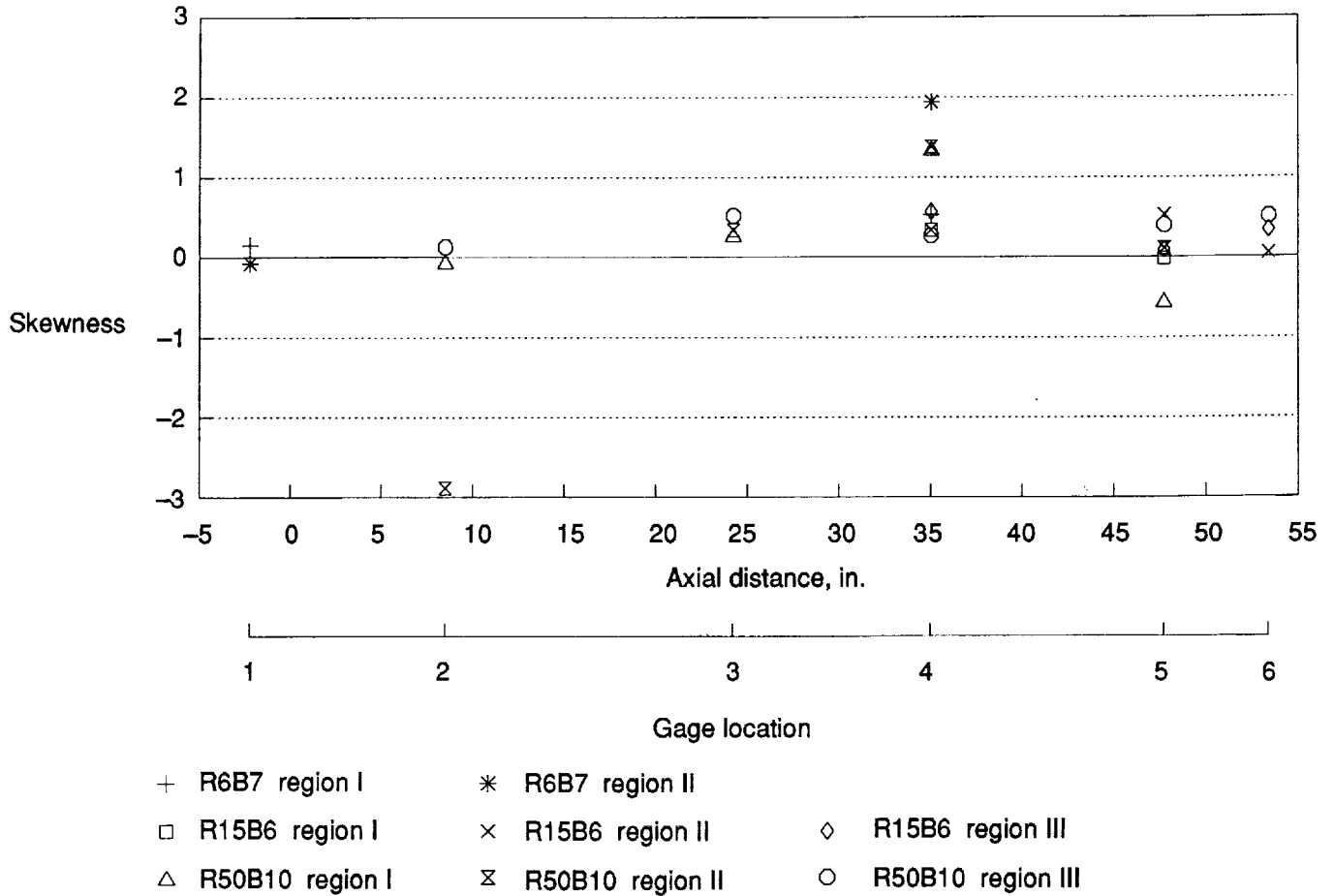


Figure 34. Skewness versus axial distance for all tests.

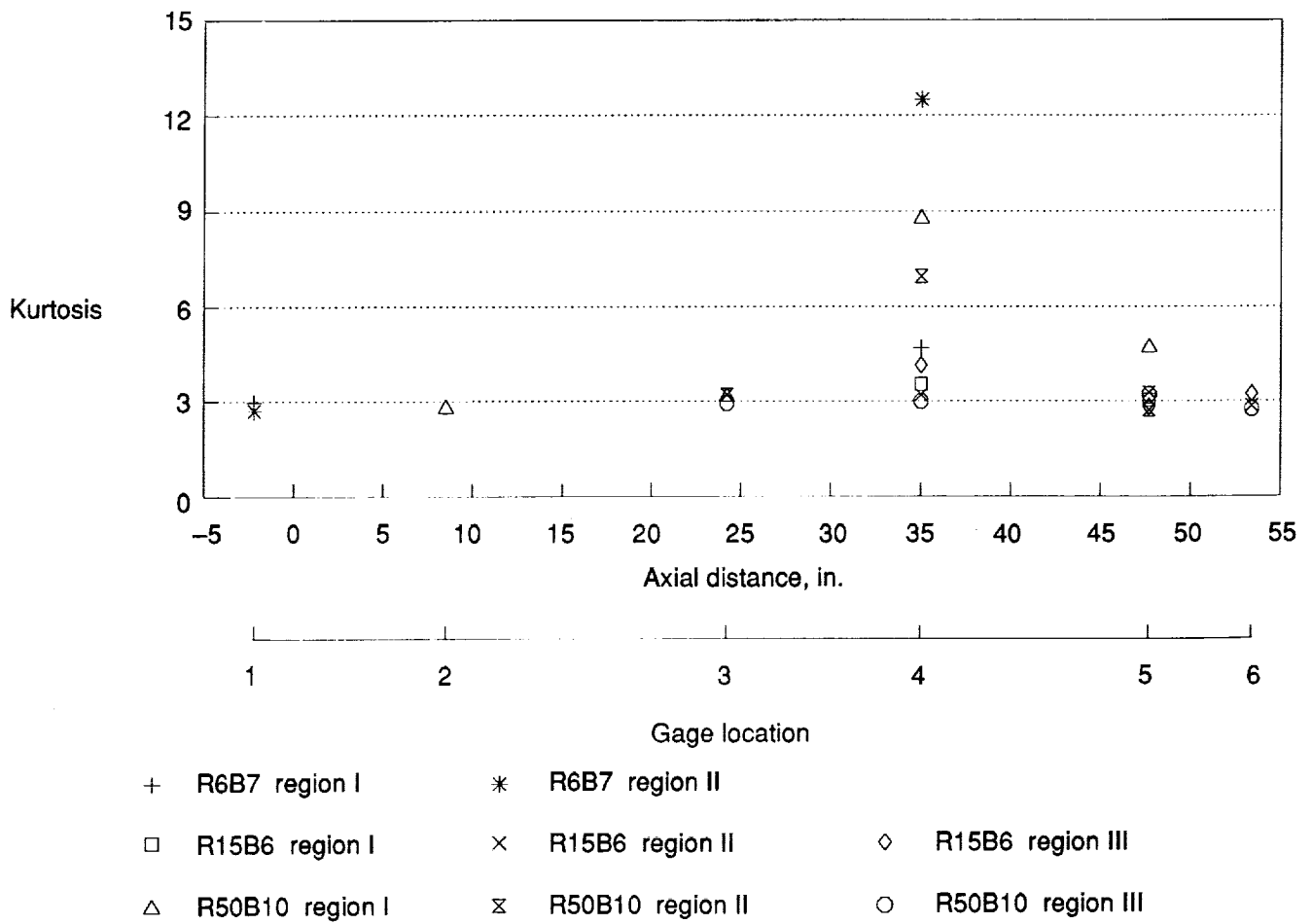
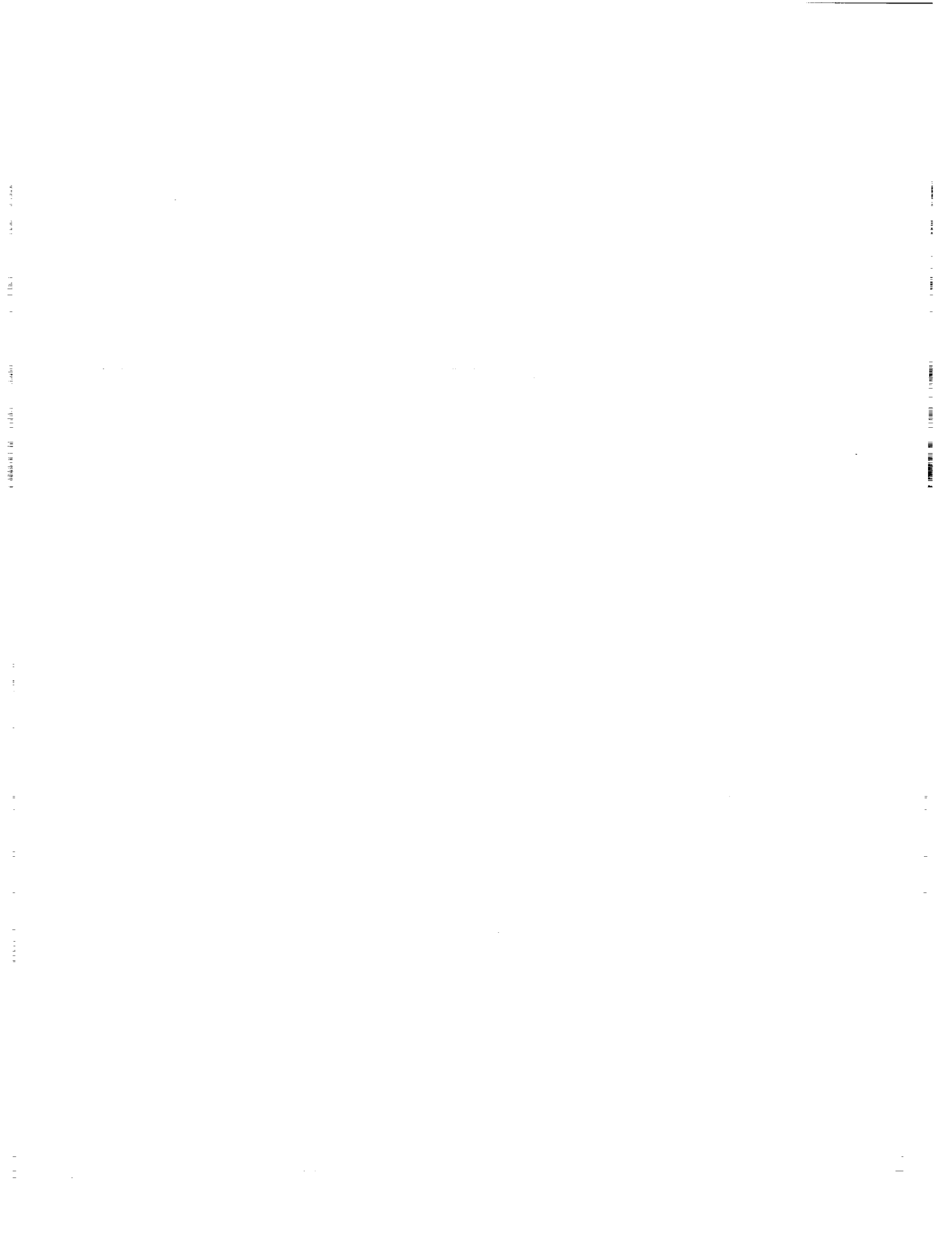


Figure 35. Kurtosis versus axial distance for all tests.

1000

1000





REPORT DOCUMENTATION PAGE			Form Approved OMB No. 0704-0188	
Public reporting burden for this collection of information is estimated to average 1 hour per response, including the time for reviewing instructions, searching existing data sources, gathering and maintaining the data needed, and completing and reviewing the collection of information. Send comments regarding this burden estimate or any other aspect of this collection of information, including suggestions for reducing this burden, to Washington Headquarters Services, Directorate for Information Operations and Reports, 1215 Jefferson Davis Highway, Suite 1204, Arlington, VA 22202-4302, and to the Office of Management and Budget, Paperwork Reduction Project (0704-0188), Washington, DC 20503.				
1. AGENCY USE ONLY (Leave blank)	2. REPORT DATE December 1992	3. REPORT TYPE AND DATES COVERED Technical Paper		
4. TITLE AND SUBTITLE Unsteady Pressure Loads in a Generic High-Speed Engine Model			5. FUNDING NUMBERS WU 763-01-41-27	
6. AUTHOR(S) Tony L. Parrott, Michael G. Jones, and Ernie M. Thurlow				
7. PERFORMING ORGANIZATION NAME(S) AND ADDRESS(ES) NASA Langley Research Center Hampton, VA 23681-0001			8. PERFORMING ORGANIZATION REPORT NUMBER L-16912	
9. SPONSORING/MONITORING AGENCY NAME(S) AND ADDRESS(ES) National Aeronautics and Space Administration Washington, DC 20546-0001			10. SPONSORING/MONITORING AGENCY REPORT NUMBER NASA TP-3189	
11. SUPPLEMENTARY NOTES Parrott: Langley Research Center, Hampton, VA; Jones and Thurlow: Lockheed Engineering & Sciences Co., Hampton, VA.				
12a. DISTRIBUTION/AVAILABILITY STATEMENT Unclassified Unlimited Subject Category 71			12b. DISTRIBUTION CODE	
13. ABSTRACT (Maximum 200 words) Unsteady pressure loads were measured along the top interior wall of a generic high-speed engine (GHSE) model undergoing performance tests in the Combustion-Heated Scramjet Test Facility at the Langley Research Center. Flow to the model inlet was simulated at 72000 ft and a flight Mach number of 4. The inlet Mach number was 3.5 with a total temperature and pressure of 1640°R and 92 psia. The unsteady pressure loads were measured with 5 piezoresistive gages, recessed into the wall 4 to 12 gage diameters to reduce incident heat flux to the diaphragms, and distributed from the inlet to the combustor. Contributors to the unsteady pressure loads included boundary layer turbulence, combustion noise, and transients generated by unstart loads. Typical turbulent boundary layer rms pressures in the inlet ranged from 133 dB in the inlet to 181 dB in the combustor over the frequency range from 0 to 5 kHz. Downstream of the inlet exit, combustion noise was shown to dominate boundary layer turbulence noise at increased heat release rates. Noise levels in the isolator section increased by 15 dB when the fuel-air ratio was increased from 0.37 to 0.57 of the stoichiometric ratio. Transient pressure disturbances associated with engine unstarts were measured in the inlet and have an upstream propagation speed of about 7 ft/sec and pressure jumps of at least 3 psia.				
14. SUBJECT TERMS Scramjet; Unsteady loads; Combustion noise; Unstarts			15. NUMBER OF PAGES 75	
			16. PRICE CODE A04	
17. SECURITY CLASSIFICATION OF REPORT Unclassified	18. SECURITY CLASSIFICATION OF THIS PAGE Unclassified	19. SECURITY CLASSIFICATION OF ABSTRACT	20. LIMITATION OF ABSTRACT	